Investigation of large-scale structures in turbulent boundary layers

M.Sc. Felix Eich

Vollständiger Abdruck der an der
Fakultät für Luft- und Raumfahrttechnik
der Universität der Bundeswehr München
zur Erlangung des akademischen Grades eines

Doktor-Ingenieurs (Dr.-Ing.)

genehmigtenen Dissertation.

Gutachter:
1. Prof. Dr. rer. nat. habil Christian J. Kähler
2. apl. Prof. Dr.-Ing. Ulrich Rist

Diese Dissertation wurde am 23.07.2020 bei der Universität der Bundeswehr München eingereicht und durch die Fakultät für Luft- und Raumfahrttechnik am 15.04.2021 angenommen. Die mündliche Prüfung fand am 11.06.2021 statt.

Abstract

The investigation of large-scale coherent structures in turbulent boundary layers has been subject to intensive research in the past decades. However, the instantaneous spatial organisation of these coherent structures and their statistical impact on the flow is still not completely understood. One difficulty in the experimental investigation are the mutual characteristics of large-scale structures, which can extend multiple boundary-layer thicknesses in length. Another difficulty arises from the large Reynolds number required to obtain large-scale structures of sufficient energy for a reliable identification and analysis.

The objective of this dissertation is to analyse the effect of Reynolds number, wall distance and streamwise momentum on the turbulent large-scale structures with the aim to better understand the impact of the large-scale structures on the turbulent boundar-layer flow itself. Therefore, velocity fields are measured in multiple wall-parallel planes and in a cross-stream plane normal to the mean flow direction. The results are analysed by means of multi-point statistical methods in order to determine the average sizes, shape and spacing of the large-scale turbulent structures. So far, most studies focus on canonical zero-pressure gradient flows. In contrast, most technical flows are subject to pressure gradients. Therefore, the impact of an adverse pressure gradient on large-scale turbulent structures is examined within this study, to investigate the persistence of the large-scale structures and the structure impact on a beginning flow separation.

The results show a dependence of the large-scale structure spatial scales on the wall distance and multiple scaling regimes are identified. Furthermore, it was shown by conditioning the statistical analysis on low and high-momentum flow events, that distinct changes in the shape and size of coherent flow structures are present. A conceptual model was then derived based on the statistics that explains the observed scaling of the large-scale structures. The analysis of the flow under the impact of an adverse pressure gradient shows a persistence of large-scale coherent structures from the preceding zero pressure gradient section through the adverse pressure gradient region until the flow separation takes place. Furthermore, the interaction between the coherent turbulent structures and the flow separation is characterised. Using conditional comparison of mean flow parameters, it is shown that high-momentum structures are able to shift the point of separation downstream while the opposite is true for low-momentum large-scale structures. This interaction has a significant impact on the dynamics of the separation line. It is also demonstrated that the separated region does not have a major influence on the mean boundary layer thickness but the mean flow velocity and spatial scales of coherent structures are visibly influenced.

Focusing on the flow field around the structures, a characteristic vortex structure is identified and quantified. Combining the observations from the scaling analysis and the vortical pattern, a self-sustaining process is described which explains the generation and decay of large-scale structures in the turbulent boundary layer. In a literature review, this process is differentiated to existing models highlighting similarities and controversies in the interpretation of observations.

Kurzfassung

Die Erforschung großskaliger, kohärenter Strukturen in turbulenten Grenzschichten erfuhr zunehmendes Interesse in den letzten Jahren. Die momentane räumliche Organisation der kohärenten Strukturen und ihrer statistischen Auswirkungen auf die Strömung ist jedoch noch nicht vollständig erforscht und erklärt. Eine Schwierigkeit bei der experimentellen Untersuchung sind die Strukturen selbst, da sie sich über mehrere Grenzschichtdicken in Strömungsrichtung ausdehnen können. Weiterhin ist eine hohe Reynoldszahl erforderlich, um großskalige Strukturen mit hinreichender Energie für eine zuverlässige Identifizierung und Analyse zu erhalten.

Ziel dieser Dissertation ist es, den Einfluss von Reynoldszahl, Wandabstand und Impuls auf die turbulenten Strukturen zu analysieren mit dem Ziel, die Bedeutung der großskaligen Strukturen auf die turbulente Grenzschicht selbst und die darin stattfindenen Prozesse besser zu verstehen. Dazu werden Geschwindigkeitsfelder in mehreren wandparallelen Ebenen und in einer Ebene senkrecht zur mittleren Strömungsrichtung mittels PIV gemessen. Die Ergebnisse werden mit Hilfe statistischer Mehrpunkt-Methoden analysiert um mittlere Strukturgrößen, Form und Abstände zu bestimmen. Bisher wurden die meisten Studien in kanonische Grenzschichten ohne Druckgradienten durchgeführt. Ein Großteil der technisch relevanten Strömungen sind jedoch im Gegensatz dazu unter dem Einfluss von Druckgradienten. Daher wird im Rahmen dieser Arbeit der Einfluss eines positiven Druckgradienten auf großskalige, turbulente Strukturen untersucht um die Beständigkeit der großskaligen Strukturen und den Einfluss der Strukturen auf eine beginnende Strömungsablösung zu ermitteln.

Die Ergebnisse zeigen eine Abhängigkeit der räumlichen Strukturskalen vom Wandabstand und es konnten mehrere Skalierungsbereiche identifiziert werden. Weiterhin wurde gezeigt, dass durch die Konditionierung der statistischen Analyse auf Strömungsereignisse mit geringem und hohem Impuls in Strömungsrichtung deutliche Veränderungen in Form und Größe von kohärenten Strömungsstrukturen vorliegen. Auf der Basis der Statistik wird ein konzeptionelles Modell abgeleitet, das die beobachtete Skalierung der großskaligen Strukturen erklärt. Die Analyse der Strömung unter dem Einfluss eines positiven Druckgradienten zeigt, dass die Strukturen beim Durchlaufen verschiedener Druckgradienten erhalten bleiben. Weiterhin kann die Wechselwirkung zwischen den kohärenten turbulenten Strukturen und der Strömungsablösung charakterisiert werden. Mit Hilfe des konditionieren Vergleichs der mittleren Strömungsparameter wird gezeigt, dass großskalige Strukturen mit hohem Impuls in der Lage sind den Ablösepunkt lokal stromabwärts zu verschieben, während das Gegenteil für großskalige Strukturen mit niedrigem Impuls zutrifft. Diese Wechselwirkung hat einen signifikanten Einfluss auf die Dynamik der Ablöseline. Die Ergebnise zeigen zudem, dass der abgelöste Bereich keinen wesentlichen Einfluss auf die mittlere Grenzschichtdicke hat, aber die mittlere Strömungsgeschwindigkeit und die räumlichen Skalen kohärenter Strukturen beeinflusst werden.

Durch die Analyse des Strömungsfeldes in der Umgebnung der Strukturen kann eine charakteristische Wirbelstruktur identifiziert und quantifiziert werden. Basierend auf der Kombination der Beobachtungen aus der Skalierungsanalyse und der Wirbelstuktur wird ein sich selbst erhaltender Prozess beschrieben, der die Entstehung und den Zerfall von großräumigen Strukturen in der turbulenten Grenzschicht erklärt.

Acknowledgement

First of all, I would like to thank Prof. Kähler for the opportunity to do a PhD and for the many discussions and inputs on turbulence research. My further thanks go to Prof. Rist for the second review, as well as the many suggestions for improvement and helpful comments and to Prof. Klein as chairman of the examination committee..

As can be seen in the following, the research involved many large-scale experiments, which are impossible to set-up alone. I'd like to thank my colleagues at the institute, especially Nico Reuther, Matthew Bross, Benedikt Mutsch, Martin Heinold and Sebastian Herbst, for helping setting up laser light-sheets, lifting mounting equipment and cameras during long hours in the wind tunnel, but also for many productive and interesting discussions on the research. In line with the daily work, my special thanks go to Rainer Hain and Sven Scharnowski who ensure the smooth work at the institute and always provided helpful suggestions and ideas as experienced senior researchers.

In the process of writing this dissertation, special thanks go to Matthew Bross and Tim Lüdemann, who both found the time and patience to read the entire manuscript and check for spelling errors, and offered helpful suggestions.

Last but not least, I would like to thank my friends and family who always support me in my work and what I do, as well as the university badminton group who helped me to keep my head clear of the turbulence turmoil at least twice a week.

Contents

Abstract **i**

Kurzfassung **iii**

Acknowledgement **v**

Contents **vii**

List of Figures **ix**

List of Tables **xiii**

List of Symbols **xv**

1 Introduction **1**

2 Fundamentals of turbulent boundary-layer flows **5**
- 2.1 Mathematical description of turbulence and coherent structures 5
  - 2.1.1 Scaling of turbulent boundary layers - mean velocity 8
  - 2.1.2 Scaling of turbulent boundary layers - turbulent fluctuations 10
  - 2.1.3 Correlation functions 11
- 2.2 Literature review on coherent structures in boundary-layer flows 12
  - 2.2.1 Definition, scaling and dynamics of large-scale structures 12
  - 2.2.2 Origin of large-scale structures and conceptual models 16
  - 2.2.3 Structure of adverse pressure gradient turbulent boundary-layer flow . . 18

3 Experimental facility and measurement setups **23**
- 3.1 Atmospheric Wind Tunnel Munich 24
- 3.2 Boundary-layer models 25
  - 3.2.1 Model 1 - RETTINA 26
  - 3.2.2 Model 2 - VicToria 27
- 3.3 Measurement Setups. 29
- 3.4 Scale and resolution estimations. 31
- 3.5 Preliminary Investigations 33
  - 3.5.1 Qualification of the local seeding system 33
  - 3.5.2 Convergence Analysis. 34

4 Statistical analysis of large-scale structures **41**
- 4.1 Scaling of large-scale structures under ZPG 41
- 4.2 Influence of the intermittency on large-scale structures 49
- 4.3 Conditional analysis of large-scale structures 53
- 4.4 Summary of the statistical analysis 58

5 Towards an improved spatial representation of a boundary layer from the attached-eddy model **61**
- 5.1 Synthetic AEM flow fields 62
- 5.2 Results and Discussion 63
  - 5.2.1 Comparisons of the original AEM configuration with experimental data. 63

5.2.2 The influence of meandering structures in the attached-eddy model . . . 64
5.2.3 Cross-plane results 66
5.2.4 Analysis of the spanwise velocity component 68

6 On the origin of large-scale structures 71
6.1 Introduction of a conceptual self-sustaining process 71
6.2 Characterisation of the vortices in the turbulent boundary layer. 73
6.2.1 Vortex size and distribution 74
6.2.2 Vortex paths 79
6.3 Comparison with existing theories and models 80

7 On the impact of an adverse pressure gradient on large-scale structures 83
7.1 Attached adverse pressure gradient turbulent boundary-layer flow. 83
7.2 Analysis of a turbulent boundary-layer flow up to flow separation. 86
7.2.1 Characterisation of the unsteady flow separation 86
7.2.2 Conditional analysis of the boundary layer parameters 87
7.2.3 Analysis of the structural pattern 88
7.2.4 Interaction between large-scale structures and flow separation. 92
7.2.5 Spectral analysis 93

8 Volumetric data - an outlook to future possibilities 95
8.1 Measurement set-up 95
8.2 Results of the volumetric measurement. 97

9 Summary 101

Bibliography 103

Appendix 112
A.1 Turbulent energy equation - APG. 113
A.2 Wall-parallel flow fields masked 114
A.3 Structures spacing calculation - binarisation algorithm test. 115
A.4 Error estimation of the vortex parameter calculation 117
A.5 Vortex path based on the potential theory. 119
A.6 Detection of the separation location 121

List of Figures

1.1 Visualisation of a turbulent boundary layer flow 2

2.1 Signal of a turbulent flow variable ϕ. 6
2.2 Energy cascade 7
2.3 Schematic turbulent boundary layer streamwise velocity profile 8
2.4 Schematic turbulent fluctuation $\overline{u'^2}/u_\tau^2$ profiles for different Re_τ 10
2.5 Sketch of an exemplary spatial two-point correlation function. 12
2.6 Scales of structures 15
2.7 Conceptual scenario of nested packets of hairpins or cane-type vortices 16
2.8 Vortices around structures 18
2.9 Turbulent intensity profiles at $Re_\tau = 1900$ 20
2.10 Pressure gradient impact on structures 21

3.1 Friction Reynolds number ranges 23
3.2 Sketch of the Atmospheric Wind Tunnel Munich 25
3.3 Sketch of the boundary-layer model 1 26
3.4 Pressure gradient distribution model 1 27
3.5 Sketch of the boundary-layer model 2 28
3.6 Pressure gradient distribution model 2 29
3.7 Sketch of the local seeding system 34
3.8 Qualification of the local seeding system, $\overline{u}$ and u' profiles 35
3.9 Intermittency factor for different Re 36
3.10 Convergence analysis 37
3.11 Convergence of two-point correlations 38
3.12 Comparison of shifted multiple point two-point correlation functions 39
3.13 Convergence of two-point correlations - point shifting 39

4.1 Instantaneous flow fields at $Re_\tau = 9300$ in three wall-parallel planes 42
4.2 Comparison of different structure scales under ZPG 44
4.3 Sketch of turbulent large-scale structures 45
4.4 Structure spacing in wall-parallel planes 46
4.5 PDF of large-scale structure spacing 46
4.6 Spatial scales from $R_{v'v'}$ and $R_{w'w'}$ 48
4.7 Instantaneous flow field under ZPG in the yz-plane. 48
4.8 Instantaneous normalised velocity field u/u_∞ in a cross-stream plane 50
4.9 Masked two-point correlation functions 50
4.10 Intermittency effect on structure scales 52
4.11 Sketch of the intermittency effect on turbulent structures 53
4.12 Quadrant analysis at $y^*/\delta_{99} = 0.07$ 54
4.13 Conditioned two-point correlation functions at $Re_\tau = 9300$ 55
4.14 Conditioned TPC at $Re_\tau = 12000$ in a cross-stream plane 56
4.15 Spatial scales from conditioned two-point correlations 57
4.16 Scaling of large-scale structures with turbulent kinetic energy 58

5.1 Comparison of streamwise velocity fluctuations u'^{+} on a wall-parallel plane between the AEM and experiment . . . 61
5.2 Schematic of a typical representative Λ eddy . . . 63
5.3 Two-point correlation coefficient $R_{u'u'}$ on a wall-parallel plane from the AEM and experiment . . . 63
5.4 Schematic illustrating the meandering angle θ and probability distribution of θ. 64
5.5 Probability distribution of the streamwise u'^{+} and spanwise w'^{+} fluctuations 65
5.6 Comparison of instantaneous streamwise velocity fluctuations fields u'^{+} from the AEM and experiments. . . . 65
5.7 Two-point correlation coefficient $R_{u'u'}$ from the AEM and experiments . . . 66
5.8 Comparison of the calculated scales based the AEM and experimental data . 67
5.9 Instantaneous colour contours of streamwise velocity u/u_∞ on a cross-stream y^*z^*-plane . . . 67
5.10 Two-point correlation coefficient $R_{u'u'}$ for a correlation point at $y^*/\delta = 0.24$ in a y^*z^*-plane. . . . 68
5.11 A comparison of instantaneous spanwise velocity fluctuations v^{+} based on the AEM and experiments . . . 69
5.12 Two-point correlation coefficient $R_{w'w'}$ for the spanwise velocity fluctuations computed on wall-parallel planes . . . 69
5.13 Conditioned two-point correlation coefficient $R_{w'w'}$ . . . 70

6.1 Instantaneous velocity field in the y^*z^*-plane at $Re_\tau = 12000$ . . . 72
6.2 Self-sustaining process of large-scale structure generation . . . 73
6.3 Conditionally averaged velocity fluctuations at $Re_\tau = 12000$ . . . 74
6.4 Characterisation of the vortex circulation Γ and the wall distance of the vortex centre . . . 75
6.5 Average number of detected vortices at $Re_\tau = 12000$ . . . 76
6.6 Characterisation of vortex core diameter and, circulation and centre location 77
6.7 Instantaneous flow field in a xz-plane with vortex centre locations . . . 77
6.8 Probability distribution of the normalised fluctuations in a wall-parallel plane 78
6.9 Joint probability distribution of the vortex core diameter d/δ_{99} and the circulation Γ in wall-parallel planes . . . 78
6.10 Detected vortex centres (●) from time-resolved data at $Re_\tau = 8400$. . . . 80

7.1 Velocity fluctuations $u'/\overline{u}$ in wall parallel planes under ZPG and APG . . . 84
7.2 Comparison of structure width W_2, height H_2 and length L_2 under APG and ZPG . . . 85
7.3 Cumulative distribution function of the instantaneous separation starting position . . . 87
7.4 Conditional analysis of the boundary layer parameters . . . 88
7.5 Normalised velocity field u/u_∞ and fluctuation field u'/u_∞ APG impact at $Re_\tau, \mathrm{ZPG} = 12000$ . . . 89
7.6 Two-point correlation function $R_{u'u'}$ at the beginning flow separation . . . 90
7.7 Evolution of the structure length and structure angle under APG conditions . 91
7.8 Spanwise spacing Λ_2 of large-scale structures under APG impact with beginning flow separation . . . 92
7.9 Conditioned streamwise mean velocity $\langle u_i \rangle$ . . . 93
7.10 Impact of large-scale structure on the position of the flow separation . . . 93
7.11 Spanwise pre-multiplied energy spectra . . . 94

8.1 Camera set-up of the volumetric measurement 96
8.2 Instantaneous snapshot of the tracked HFSB at $Re_\tau = 4200$ 98
8.3 Exemplary instantaneous wall-parallel cut sub-volumes from the HSFB measurements 99
8.4 3D correlation functions 100

A.1 Masked flow fields at $Re_\tau = 9300$ 114
A.2 Diagnosis factor χ 115
A.3 Structure spacings from binarised flow fields 116
A.4 Sketch of a generic vortex 117
A.5 Relative error ϵ_{rel} of the circulation and area estimation. 118
A.6 Sketch of potential vortices in the turbulent boundary layer 119
A.7 Sketch of the flow separation. 121
A.8 CDF of the instantaneous separation locations 122

List of Tables

3.1 Flow parameters of the experiments on model 1 27
3.2 Flow parameters of the experiments on model 2 29
3.3 Experimental equipment and positioning of the experiments 30
3.4 Experimental and PIV evaluation parameters 31
3.5 Estimated spatial scales within the turbulent boundary layer 32

4.1 Mean, standard deviation and most probable distance of the Λ_2 distribution . 46

8.1 Experimental parameters of the volumetric measurements 97

List of Symbols

Symbol	**Unit**	**Name**
Latin Symbols		
a	m/s^2	acceleration
A	m^2	area
A_0	m^2	vortex core area
b	m	distance
c	–	fitting constant
C	–	integration constant
d	m	diameter
d_0	m	vortex core diameter
d_L	m	light sheet thickness
B	–	logarithmic law constant
f	Hz	frequency
f_s	Hz	samplilng frequency
h	m	distance
H_1	m	absolute structure height
H_2	m	structure height in a cut plane
H	–	shape factor
i	–	running index
I	–	intensity
j	–	running index
k	–	conditioning factor
k	1/m	wave number
k_d	1/m	dissipation range boundary wave number
k_f	1/m	energy carrying boundary wave number
k_p	m^2/s^2	turbulence production
K	m^2/s^2	turbulent kinetic energy
L	m	length scale
L_1	m	absolute structure length
L_2	m	structure length in a cut plane
n	–	running index
M	–	masking function
M	–	magnification
N	–	number of PIV images
$N_{u<0}$	–	number of reverse flow vectors
$\mathcal{O}$	–	order of magnitude
p	Pa	pressure
$\mathcal{P}$	–	probability
r	m	radius
r_0	m	vortex core radius

R	–	two-point correlation function
Re	–	Reynolds number
Re_{L}	–	Reynolds number based on the length L
Re_{τ}	–	friction velocity Reynolds number
Re_{θ}	–	momentum deficit Reynolds number
t	s	time
t_{CPU}	s	computational time
T	°C	temperature
Th	–	threshold
Tu	%	intensity of turbulence
u	m/s	streamwise velocity component
u_{i}	m/s	induced velocity
u_{P}	m/s	streamwise velocity component in the correlation point P
u_{s}	m/s	velocity lag due to Stokes drag
u_{τ}	m/s	friction velocity
u_{∞}	m/s	free stream velocity
u_0	m/s	velocity at start of the wind tunnel test section
v	m/s	wall-normal velocity component
w	m/s	spanwise velocity component
W_1	m	absolute structure width
W_2	m	structure width in a cut plane
x, y, z	m	wind tunnel cartesian coordinate system
x^*, y^*, z^*	m	relative model cartesian coordinate system

Greek Symbols

α	∘	angle
β	–	Rotta-Clauser pressure gradient parameter
χ	–	diagnosis factor
δ	m	boundary layer thickness
δ_{99}	m	boundary layer thickness with $u(\delta_{99}) = 0.99\,u_{\infty}$
δ^*	m	mass deficit thickness
Δ	–	difference
ϵ	$\mathrm{m^2/s^3}$	turbulent dissipation
ϵ_{rel}	–	relative error
η_{k}	m	Kolmogorov length
γ	–	intermittency factor
Γ	$\mathrm{m^2/s}$	circulation
λ	m	wavelength
λ_d	1/m	dissipation range boundary wavelength
λ_f	1/m	energy carrying boundary wavelength
Λ	m	structure spacing/ periodicity

Λ_2	m	structure spacing/ periodicity in a cut plane
κ	–	Karman constant
μ	$\mathrm{Pa} \cdot \mathrm{s}$	dynamic viscosity
μ	–	expected value
ν	m^2/s	kinematic viscosity
ω	1/s	vorticity
ϕ	–	flow variable
φ	$\circ$	structure angle relative to the wall
ψ	–	scale resolution ratio
ρ	kg/m^3	density
σ_u	m/s	standard deviation of the fluctuation distribution
σ	Pixel	uncertainty of the pixel displacement
σ	–	measurement uncertainty
τ	Pa	shear stress
τ_w	Pa	wall shear stress
τ_δ	s	boundary layer turn over time
θ	m	momentum deficit thickness

Abbreviations

APG	adverse pressure gradient
AEM	attached-eddy model
AWM	Atmospheric Wind Tunnel Munich
DEHS	Di-Ethyl-Hexyl-Sebacat
DFG	Deutsche Forschungsgemeinschaft
DLR	Deutsches Zentrum für Luft und Raumfahrt
DNS	direct numerical simulation
FOV	field of view
FPG	favourable pressure gradient
HFSB	helium filled soap bubbles
IW	interrogation window
LED	light emitting diodes
PDF	probability density function
PIV	particle image velocimetry
POD	proper orthogonal decomposition
ppp	particles per pixel
PTV	particle tracking velocimetry
RETTINA	Reliable Turbulence and Transition Modelling for Industrial Aerodynamics
RMS	root mean square
SLTEST	Surface Layer Test
STB	Shake The Box
SPIV	stereoscopic particle image velocimetry
SSVM	self-sustaining flanking vortex model

TBL	turbulent boundary layer
TNTI	turbulent/ non-turbulent interface
VicToria	Virtual Aircraft Technology Integration Platform
VLSM	very large scale motion
ZPG	zero pressure gradient

Indices [denoted for a given variable ϕ]

ϕ_{F}	fluid
ϕ_{Max}	maximum value
ϕ_{Min}	minimum value
ϕ_{P}	value at the correlation point
ϕ_{TP}	value at the correlation point
ϕ_{W}	value at the wall
ϕ_{∞}	free stream value
ϕ^{+}	wall units
$\overline{\phi}$	ensemble averaged component
$\langle\phi\rangle$	conditional averaged component
ϕ'	fluctuating component

1

Introduction

The substantial reduction of carbon dioxide emission is crucial for the limitation of global warming in near future. Therefore, the International Civil Aviation Organisation has set new targets for the environmental sustainability of commercial aviation. Carbon dioxide emissions are to be reduced by 50 % until 2050, based on 2005 emissions (International Civil Aviation Organization, 2019). In order to achieve this goal, it is necessary to improve the engines, optimise flight planning and to fluid mechanically optimise the aircraft to reduce drag. The drag of an aircraft in cruising flight is composed of approximately 50 % − 60 % friction drag, approximately 20 % lift dependant drag, additional interference drag and propulsion caused drag (Oertel et al., 2013). Since the friction drag represents the largest proportion and it is difficult to reduce the other drag sources, the focus of the fluid mechanical optimisation is the flow over the aircraft surface. Many different approaches are generally possible, e.g. active or passive flow control, which lead to delayed boundary layer transition, improved boundary layer profile shapes or delayed flow separation (Schlichting and Gersten, 2006; Lachmann, 2014). All techniques have in common that a deep fundamental understanding of the flow physics is an indispensable necessity.

For all flows over surfaces, an area is created where the flow is slowed down by skin friction at the wall. This region is known as the boundary layer. A boundary layer can be in a laminar or turbulent state. Almost all technically relevant boundary layer flows, including the flow around a commercial aircraft, are turbulent. While laminar boundary layers can be described mathematically and the governing equations solved analytically, turbulent flows have to be analysed by experiments or numerical flow simulations. The complexity of turbulence is directly visible in the visualisation of a turbulent boundary layer flow over a flat plate in figure 1.1. The turbulent boundary layer flow consists of vortices of multiple scales, orientation and strength, is time dependant and chaotic due to non-linear interactions. The action of the vortices and velocity fluctuations lead to increased diffusivity, dissipation and viscous drag in a turbulent flow in comparison to laminar flow.

A major challenge in turbulence research is the need for large Reynolds numbers to capture real or comparable flow conditions. This makes the experimental investigation and simulations difficult. The computational time t_{CPU} for a direct numerical simulation (DNS) scales with the Reynolds number $t_{\mathrm{CPU}} \propto Re_{\mathrm{L}}^3$ (Fröhlich and von Terzi, 2008). Considering present computational capabilities, thousands of years of computational time are needed to simulate a boundary layer flow at realistic conditions to have sufficient statistical independent data for turbulence analysis. Hence, modelling is necessary which needs profound data bases and physical understanding of the turbulence and turbulent boundary layer flow itself. These data bases are usually generated experimentally. This is also the focus of this thesis,

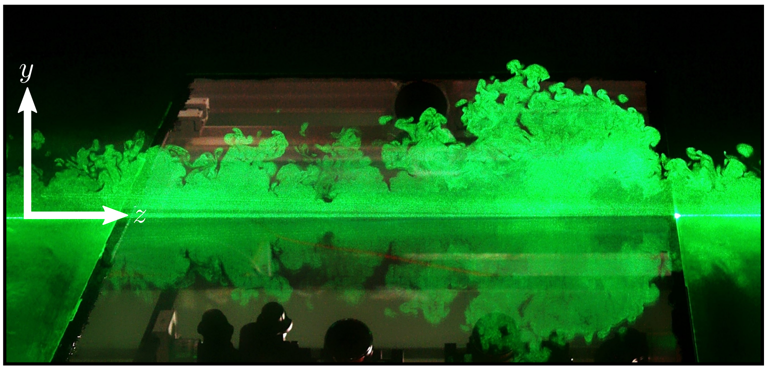

Figure 1.1: Visualisation of a turbulent boundary layer flow in the cross-stream plane (yz-plane).

where a turbulent boundary layer flow is experimentally investigated to improve the physical understanding of the processes within the turbulence.

Earlier studies of turbulent boundary layer flows focus on mean flow and mean flow statistics. In recent years, the understanding of the structural composition of a turbulent boundary layer became one of the key fields in turbulence research (Wallace, 2012; Marusic et al., 2010; Robinson, 1991). Coherent vortical structures are believed to be responsible for a large part of the production and decay of turbulence, for the transport of turbulent kinetic energy and momentum, and for the interaction of different features within the turbulent flow. The concept of turbulent coherent structures is not new, but has often been used in the past to explain processes and observations in the measured mean statistics of a turbulent boundary layer flow (Wallace, 2012; Robinson, 1991). Earlier studies used smoke or hydrogen bubble visualisations to get an insight in the structural pattern of the turbulent boundary layer flow (Kline et al., 1967; Head and Bandyopadhyay, 1981). With advances in optical measurement technology, such as Particle Image Velocimetry (PIV), it became possible not only to make quantitative observations but also to investigate qualitatively turbulent flow fields, as shown in the exemplarily chosen works of Kim and Adrian (1999); Kähler (2004); Dennis and Nickels (2011). In his talk “Highlights of 50 years of Turbulent Boundary Layer Research” at the Marseille colloquium 2011, J. Wallace has summarised previous research on turbulence: “There has been remarkable progress in turbulent boundary layer research in the past 50 years, particularly in understanding the structural organization of the flow. Consensus exists that vortices drive momentum transport but not about the exact form of the vortices or how they are created and sustained.”

One only partly understood structural feature of a turbulent boundary layer flow are large-scale, in streamwise direction elongated structures, which receive increased interest in the turbulent boundary layer flow research. These large-scale structures carry a significant proportion of turbulent kinetic energy and are therefore an important feature of the turbulent boundary layer flow (Hutchins and Marusic, 2007a; Marusic et al., 2010). The possibility of benefiting from these structures or preventing their formation has great potential for improving the control of turbulent boundary layer flows or reducing the skin friction within the turbulent boundary layer flow. The existence of these large-scale structures is generally accepted, but there are various theories about their origin and effect (Hunt and Morrison, 2000; Adrian, 2007; Marusic et al., 2010). That is why the focus of this dissertation is on the experimental investigation of large-scale coherent structures in the turbulent boundary layer flows at technically relevant flow conditions. In detail, the scaling of the structures will be analysed to better understand the structures occurrence and dynamics. In a second step, the focus is on the generation and origin of the large-scale structures. Therefore, the existing attached-eddy model is analysed and improved and a different explanation based on the dynamic interaction processes in the turbulent boundary layer flow is given. Finally, the persistence of large-scale coherent structures on an adverse pressure gradient impact is investigated, to better understand the large-scale structure behaviour in technically relevant flow conditions.

In the following chapter 2, an overview of the fundamentals, theoretical and mathematical description of the turbulent boundary layer flow is given. Also a selected review on past studies concerning coherent structures in turbulent boundary layers is discussed. Based on this literature survey on past research, three fundamental research questions are formulated. As mentioned above, experiments are well suited to investigate boundary layer flows at technically relevant Reynolds numbers. A detailed description of the experimental facility, setup and equipment is given in chapter 3. State of the art laser optical measurement techniques are utilised to capture instantaneous flow fields to qualitatively and quantitatively describe the flow. The results from the measurements are presented, explained and discussed in chapters 4 to 7. In chapter 8, the results of an unique time dependant and three-dimensional volumetric measurement are presented to compare and confirm the results and observations drawn based on the two-dimensional data analysis from the previous chapters.

2

Fundamentals of turbulent boundary-layer flows

Research on turbulent boundary-layer flows has seen vast interest and progress over the past decades, as seen in the review papers by Wallace (2012) and Marusic et al. (2010) and briefly discussed in the introduction, but still complete understanding of the processes, structures and interactions within the turbulent boundary-layer flow has not been achieved. The challenging issues are the natural characteristics of turbulence itself. In general, turbulence is three-dimensional, unsteady, dissipative, diffusive and consists of vortices of multiple scales (Fröhlich and von Terzi, 2008). In contrast to free shear flow turbulence, turbulent boundary layers are bound by a wall where the main shear occurs. This leads to highly anisotropic characteristics. Its shape is not deterministic or constant but consists of vortices and structures of various time dependent sizes, shapes and orientations. Hence, it is necessary to describe the turbulent boundary-layer flow by means of time or ensemble averaged quantities and statistical methods. Those approaches will be described in the following section 2.1.

Many past investigations in wall bounded turbulence focused on the impact of coherent structures on the flow physics and statistics. As argued by Robinson (1991) there must be a motion within the boundary-layer flow that is not spatially random, because otherwise the turbulence production term $\overline{u'v'}$ would be equal to 0, which applies for isotropic turbulence. Assuming that such a structure exists, which is responsible for the conversion of the mean motion into turbulent Reynolds stresses, and the dissipation of turbulence, the understanding of the physics of this structure is the key for understanding the physics of boundary-layer flows itself (Kline and Robinson, 1990). Therefore, an overview of past and current research on coherent structures in a turbulent boundary-layer flow is given in section 2.2.

So far, most studies on turbulent boundary-layer flows were performed in zero pressure gradient boundary layers, which is the canonical reference case. In contrast, most technically relevant and natural flows are subject to pressure gradients. A literature survey of past research on the influence of an adverse pressure gradient in turbulent boundary-layer flows and the corresponding structures is given in section 2.2.3.

2.1. Mathematical description of turbulence and coherent structures

As turbulence is a chaotic flow state, statistical methods are needed for its mathematical description. The models and formulas discussed in the following are taken from the textbooks of Pope (2011) and Schlichting and Gersten (2006), in which turbulence and turbulent boundary layers are discussed in theory and more detail. For additional information the reader should refer to those textbooks.

The description of turbulent flows is in many cases based on a decomposition of the instantaneous flow variables, the Reynolds decomposition. A flow variable

$$\phi = \overline{\phi} + \phi' \tag{2.1}$$

is decomposed into an ensemble average value $\overline{\phi}$ and a fluctuating value ϕ', as highlighted in figure 2.1.

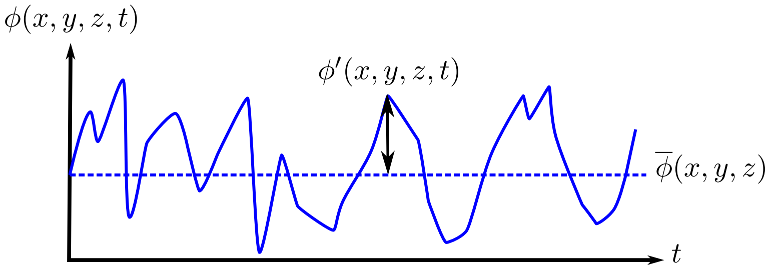

Figure 2.1: Signal of a turbulent flow variable ϕ (blue). The dashed line corresponds to the time averaged quantity $\overline{\phi}$.

To quantify the turbulence it is necessary to measure the magnitude of the fluctuations ϕ'. As turbulence is a statistical process, the RMS value of the time dependant fluctuation

$$\phi_{\mathrm{RMS}} = \sqrt{\frac{1}{N-1}\sum_{n=1}^{N}\phi'^2} \tag{2.2}$$

can be taken as a measure for average absolute intensity of the turbulent fluctuations. The RMS value of ϕ is normally set in relationship with the average value $\overline{\phi}$ to get the relative turbulence intensity. Based on this, the turbulence intensity

$$Tu = \frac{\sqrt{\frac{1}{3}\left(\overline{u'^2} + \overline{v'^2} + \overline{w'^2}\right)}}{\sqrt{(\overline{u}^2 + \overline{v}^2 + \overline{w}^2)}} \tag{2.3}$$

is defined as a measure for the turbulence of the velocity components u, v and w.

To describe the motion of a flow in a continuum without chemical reactions and thermodynamic effects, the Navier-Stokes equations are commonly applied. They are also valid for turbulent flows and are an exact description of the flow. For simplification and statistical modelling, the Reynolds decomposed flow variables are inserted into the Navier-Stokes equations resulting in the incompressible Reynolds-Averaged Navier-Stokes equations without external forces

$$\frac{\partial \overline{u_j}}{\partial t} + \frac{\partial \overline{u_i}\overline{u_j}}{\partial x_i} = -\frac{1}{\rho}\frac{\partial \overline{p}}{\partial x_j} + \frac{\partial}{\partial x_i}\left(\nu\frac{\partial \overline{u_j}}{\partial x_i} - \overline{u_i'u_j'}\right) \tag{2.4}$$

here written in the summation form with the indices $i = 1$ to 3 and $j = 1$ to 3. The tensor

$$\overline{u_i'u_j'} = \begin{pmatrix} \overline{u'^2} & \overline{u'v'} & \overline{u'w'} \\ \overline{v'u'} & \overline{v'^2} & \overline{v'w'} \\ \overline{w'u'} & \overline{w'v'} & \overline{w'^2} \end{pmatrix} \tag{2.5}$$

is the Reynolds stress tensor. It's a symmetric tensor which describes the effect of the turbulence as fictive stresses in the Navier-Stokes equations. This term is the key subject of turbulence modelling, especially for numerical flow simulations.

From a structural point of view, the Reynolds stress tensor is also important. This becomes more obvious by looking closer into the turbulent energy budget. Detailed equations and derivations are given in appendix A.1. Turbulence production for a flat plate zero pressure gradient boundary layer

$$k_\mathrm{p} = -\rho\left(\overline{u'v'}\frac{\partial\overline{u}}{\partial y}\right) \tag{2.6}$$

is mainly driven by the shear stress $\overline{u'v'}$ and wall-normal mean velocity gradient $\frac{\partial\overline{u}}{\partial y}$. The gradient of $\overline{u}$ is a result of shear forces, while the mixed term $\overline{u'v'}$ is a consequence of turbulent structures, as pointed out briefly in the chapter introduction. The other terms in the stress tensor are a measure for the interaction and deformation of turbulent structures or vortices, taking place in the turbulent flow. Hence, the understanding of structures in a boundary layer is crucial for the efficient modelling of turbulent boundary-layer flows.

As mentioned in the introduction, turbulence is a multi scale and dissipative process. In the classical picture of turbulence, the turbulent kinetic energy is transported from large-scale turbulent structures in a cascade process to smaller scales and then dissipated into heat at the smallest scales, known as the Kolmogorov scales η_k. In figure 2.2, the energy distribution as a function of the wave number k is shown qualitatively.

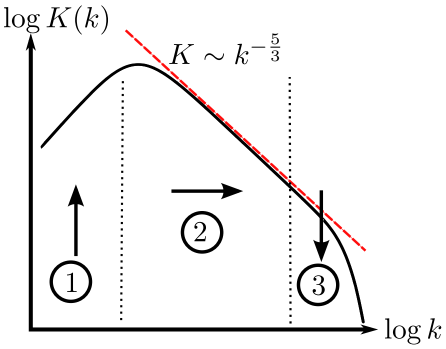

Figure 2.2: Sketch of the energy cascade in the turbulent boundary layer. Characeristic regions are marked: (1) energy carrying large vortices/ production of turbulence; (2) the inertial region; (3) the dissipation region.

The energy cascade within the turbulence can be divided into three different sections based on the flow physics: The energy carrying large vortices (1) where turbulence is produced, the inertial range (2) with the proportionality law of $K \sim k^{-\frac{5}{3}}$ and the dissipation range (3). Pope (2011) provides estimated reference values for the wave numbers k_f up to which the energy is transferred into turbulence and the wave number k_d at which the dissipation range starts.

$$k_f = 6\frac{2\pi}{0.43L};\; k_d = \frac{2\pi}{60\eta_\mathrm{k}} \tag{2.7}$$

The range in between $k_\mathrm{d} < k < k_\mathrm{f}$ is the inertial range, where the energy is transported from larger to smaller scales due to vortex interaction and stretching processes.

In contrast to the large-scales in turbulence, which are highly anisotropic, the Kolmogorov scales can be considered as isotropic due to their small spatial extent. Based on this assumption that the turbulent dissipation approaches a finite threshold for $Re \to \infty$, the Kolmogorov scales η_k and the dissipation ϵ

$$\eta_\mathrm{k} = \left(\frac{\nu^3}{\epsilon}\right)^{\frac{1}{4}}, \epsilon = 15\nu\overline{\left(\frac{\partial u'}{\partial x}\right)^2} \tag{2.8}$$

can be estimated. Pope (2011) suggests a ratio between the largest scales L and the Kolmogorov scales of

$$L/\eta_\mathrm{k} = Re_\mathrm{L}^{3/4} \tag{2.9}$$

based on the Reynolds number $Re_\mathrm{L} = \frac{\sqrt{K}L}{\nu}$ with the velocity scales $\sqrt{K}$ based on the kinetic energy K. Thereby, it is possible to estimate the Kolmogorov scales without measuring the dissipation, which is experimentally difficult.

2.1.1. Scaling of turbulent boundary layers - mean velocity

Numerical flow simulations and experiments in boundary layers are performed under various boundary conditions and flow velocities. To make different data sets comparable, similarity numbers and characteristic parameters are necessary. For turbulent boundary layers, those are mostly based on the time averaged quantities $\overline{\phi}$.

In figure 2.3 left, a fully developed, canonical turbulent boundary layer profile of the average streamwise velocity $\overline{u}$ is shown schematically.

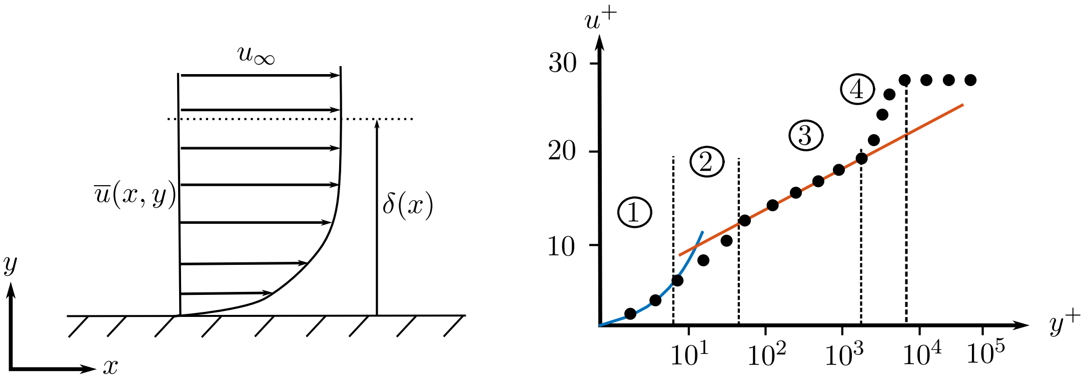

Figure 2.3: Schematic turbulent boundary layer streamwise velocity profile. Left: Profile over a flat plate. Right: Profile (● symbols) scaled in inner variables. Characteristic regions are: 1 - Viscous sublayer, 2 - Buffer layer, 3 - logarithmic layer, 4 - wake region.

As the boundary layer thickness δ is not well defined, the substitute boundary layer thickness δ_{99}, which is defined as

$$\delta_{99} = y(\overline{u} = 0.99 \cdot u_\infty) \tag{2.10}$$

is used as an alternative. Further definitions of characteristic thicknesses in a turbulent boundary layer are the mass deficit thickness or displacement thickness

$$\delta^* = \int_0^\infty \left(1 - \frac{\overline{u}(y)}{u_\infty}\right) dy \tag{2.11}$$

and momentum deficit thickness

$$\theta = \int_0^\infty \frac{\overline{u}(y)}{u_\infty}\left(1 - \frac{\overline{u}(y)}{u_\infty}\right) dy, \tag{2.12}$$

which both define a thickness based on the free-stream velocity lag. The ratio of the mass deficit thickness and the momentum thickness

$$H = \frac{\delta^*}{\theta} \tag{2.13}$$

is called the shape factor. The shape factor is an important indicator to evaluate if there are deviations from a canonical turbulent boundary layer (Klewicki, 2010). For fully developed zero pressure gradient turbulent boundary layers the shape factor equals $H \approx 1.4$ (Schlichting and Gersten, 2006). With increasing Reynolds number, the shape factor decreases to $H \rightarrow 1$ for $Re \rightarrow \infty$ (Klewicki, 2010). Hence, there is no equilibrium ZPG boundary layer that is self-similar but a Reynolds number dependency is present according to Klewicki (2010). As the decrease of parameters such as H in streamwise direction is small, the ZPG can be considered as a self-similar canonical case and therefore be used as a reference case (Townsend, 1956).

Scaling the physical units such as velocity and wall distance with the boundary layer thickness and free stream velocity is refered as outer scaling. In contrast, it is also possible to scale a boundary layer in inner units, also called viscous units, wall units or "+"-units. The inner scaling is based on the friction velocity

$$u_\tau = \sqrt{\frac{\tau_\mathrm{w}}{\rho}}, \tag{2.14}$$

with the wall shear stress τ_w and the density ρ. Based on the friction velocity, the velocity u and wall distance y are scaled

$$u^+ = \frac{u}{u_\tau},\ y^+ = \frac{y \cdot u_\tau}{\nu} \tag{2.15}$$

into viscous units. Utilising the inner scaling, multiple characteristic regions of the boundary layer can be distinguished with the following relations between velocity u^+ and wall distance y^+, as schematically shown in the sketch of an inner scaled turbulent boundary layer in figure 2.3 right. The characteristic regions are:

1. Viscous sublayer: $y^+ < 5 \rightarrow u^+ = y^+$
2. Buffer layer: $5 < y^+ < 70$
3. logarithmic layer: $70 < y^+$ and $y < 0.15\delta \rightarrow u^+ = \frac{1}{\kappa}\log(y^+) + B$

Recent studies question the fixed bounds of the logarithmic layer as given by Schlichting and Gersten (2006) and stated above (Nagib and Chauhan, 2008; Marusic et al., 2013). In their review on the logarithmic layer, Marusic et al. (2013) give a conservative estimate for which the data between $3Re_\tau^{\frac{1}{2}} < y^+ < 0.15Re_\tau$ fall into the logarithmic layer. The constants of the logarithmic law, κ and B, were considered to be universal for all wall bounded flows, but recent studies show an influence of the Reynolds number as well as of the flow itself, e.g. pipe flow or boundary-layer flow (Nagib and Chauhan, 2008). For high Reynolds number zero pressure gradient turbulent boundary-layer flows, the scaling constants are $\kappa = 0.38$ and $B = 4.1$ (Österlund et al., 2000). In turbulent boundary layers under the influence of an adverse pressure gradient the logarithmic layer itself is decreasing and the scaling constants κ and B change (Knopp et al., 2014, 2015; Nickels, 2004). For APG turbulent boundary layers, no generally agreed scaling law or parameter set exists. In their theoretical study of various experimental and numerical data bases, Maciel et al. (2018) focused on the outer scaling of an APG boundary layer providing a set of consistent scaling parameters for the length, velocity and pressure scale. They also provide a detailed overview of previous scaling ideas. Different approaches for the scaling of an APG boundary layer were followed by Knopp et al. (2015)

and Nickels (2004). Their scaling approaches are based on modified inner scaling principles. Boundary layers under an APG influence will be discussed in more detail in section 2.2.3.

The most important similarity parameter in fluid mechanics is the Reynolds number. It represents the ratio between inertia and friction forces. Ensuring similar Reynolds numbers is the necessity to ensure comparability between different data sets from experiments as well as numerical simulations. In boundary layer research, the Reynolds number based on the friction velocity

$$Re_\tau = \frac{u_\tau \cdot \delta}{\nu} = \frac{\delta}{\nu/u_\tau} \tag{2.16}$$

is commonly used. The friction velocity Reynolds number can be interpreted physically as the ratio between the largest and the smallest scales in the boundary layer. The largest scales expected in a boundary layer are in the order of the boundary layer thickness $\mathcal{O}(\delta)$, whereas the smallest scales are in the order of the viscous unit $\mathcal{O}(y^+) = \mathcal{O}(\nu/u_\tau)$ (Klewicki, 2010). In terms of viscous scaling, the friction velocity Reynolds number can be interpreted as the non-dimensional boundary layer thickness in viscous units $\delta^+ = \frac{\delta}{\nu/u_\tau}$. In addition to the friction velocity based Reynolds number Re_τ, Reynolds numbers based on the free stream velocity u_∞ and different characteristic length scales, such as the momentum thickness θ or displacement thickness δ^* are used to characterise and compare boundary layers. In the specific case of a flat plate zero pressure gradient boundary layer, the development length x of the boundary layer in streamwise direction can be used as the characteristic length. The necessary condition for a comparable scaling is a newly developed boundary layer, which is often difficult to achieve in experiments, since the walls of wind tunnels are usually used for the boundary layer experiments.

2.1.2. Scaling of turbulent boundary layers - turbulent fluctuations

In the previous section 2.1.1, the scaling based on the mean flow variables $\overline{\phi}$ was described. Another important quantity of turbulence is the turbulent fluctuation ϕ', which is a measure for the intensity of turbulence as discussed in the beginning of section 2.1. In figure 2.4, the characteristic distribution of the normalised fluctuations $\overline{u'^2}/u_\tau^2$ with the wall distance is plotted for low and high Reynolds numbers under zero pressure gradient, according to Marusic et al. (2010).

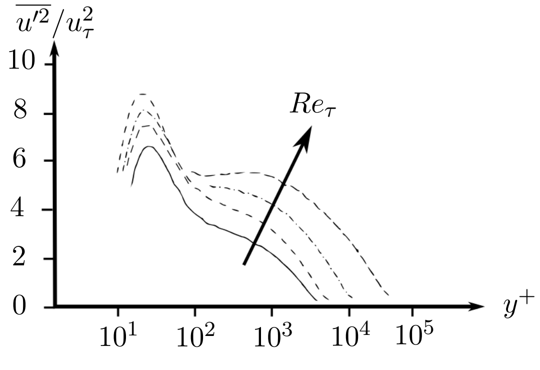

Figure 2.4: Left: Schematic turbulent fluctuations $\overline{u'^2}/u_\tau^2$ profiles in turbulent boundary layers for different Re_τ.

Near the wall at $y^+ \approx 15$ the inner peak in the fluctuation spectra is present, which has an intensity of $\overline{u'^2}/u_\tau^2 = 6 - 8$ depending on the Reynolds number (Samie et al., 2018). This peak is presumably associated with the presence of near-wall streaks in turbulence (Smits et al., 2011). With increasing Reynolds number, a second plateau/ peak is becoming more prominent at higher wall distance (Hutchins and Marusic, 2007a; Marusic et al., 2010). This peak is located in the logarithmic layer, hence different effects within the turbulent boundary layer are responsible. It is supposed that this second peak is a result of the presence of large-scale structures in the logarithmic layer, which are highly energetic (Hutchins and Marusic, 2007b). A detailed discussion of the coherent structures, which are associated with the characteristic peaks in the energy distribution within the turbulent boundary-layer flow, is given in section 2.2.

A different approach to analyse and scale the turbulent fluctuations are energy spectra. For time resolved data with a sampling frequency f_s, a turbulent signal can be analysed up to $f_\mathrm{s}/2$ due to the Nyquist criterion. As experimental techniques such as hot-wire anemometry or high-speed PIV are capable to capture data in the kHz range (Hutchins et al., 2009; Raffel et al., 2018), it is possible to calculate energy spectra from the data using Fourier transformation. An exemplary pre-multiplied energy spectrum can be found in Hutchins and Marusic (2007b). The dimensionless turbulent kinetic energy $k_{u'u'}/u_\tau^2$, calculated based on the turbulent fluctuations, is pre-multiplied with the corresponding streamwise wavelength λ_x, which results in a weighted energy spectrum, showing the energy content relative to the corresponding structure length (Hutchins and Marusic, 2007b; Monty et al., 2011). The wavelength associated with the inner energy peak is $\lambda_x^+ \approx 1000$, the characteristic wavelength of the outer peak $\lambda_x \approx 6\,\delta_{99}$ (Smits et al., 2011).

Under the impact of pressure gradients, the scaling changes significantly. While the inner peak is nearly unaffected by the pressure gradient, the outer peak becomes less energetic for a favourable pressure gradient and more energetic for an adverse pressure gradient. The corresponding wavelength from the spectral analysis increases for the FPG and decreases for the APG (Monty et al., 2011; Harun et al., 2013). The structural consequences of these observations, such as changes in scaling and the persistence of large-scale structures under a pressure gradient impact, are discussed in section 2.2.3 and are subject of the research within this dissertation.

2.1.3. Correlation functions

For the detection of structures in turbulence correlations are commonly used, as exemplary shown by Ganapathisubramani et al. (2005) and Kähler (2004). It is differentiated between auto-correlations and cross-correlations/ two-point correlations. In auto-correlations a signal is analytically compared with itself. The time or length for which the correlation values are positive the signal resembles itself. Accordingly, the time or length of the positive correlation or up to a chosen threshold value is a measure for the size of structures within the turbulence.

In contrast to the auto-correlation, in two-point correlations two signals are compared. For the evaluation in this thesis, mainly spatial two-point correlations are applied to calculate scales from vector fields. The two-point-correlation coefficient $R_{\phi'\phi'}(x,y,z)$ for the flow field ϕ' and the correlation point P is defined as

$$R_{\phi'\phi'}(x,y,z) = \frac{\sum_{n=1}^{N} \phi'(x,y,z) \cdot \phi'(x_\mathrm{P}, y_\mathrm{P}, z_\mathrm{P})}{N \cdot \sigma(x,y,z) \cdot \sigma(x_\mathrm{P}, y_\mathrm{P}, z_\mathrm{P})}, \tag{2.17}$$

normalised with the standard deviation $\sigma(x,y,z)$ of the field ϕ at the corresponding points. The signal at one correlation point P is compared to a whole field for a sufficient number of statistical independent data N. The resulting correlation fields of the single statistical samples are afterwards averaged. A detailed convergence analysis is discussed in section 3.5.2 to ensure that the resulting correlations are not biased due to convergence effects of the mean flow velocity or turbulent fluctuations. Spatial two-point correlations result in a correlation map as exemplarily sketched in figure 2.5 for a wall-normal streamwise $xy-$plane.

The dashed lines enclose different positive correlation regions (red), the dotted line encloses negative correlated areas (blue).

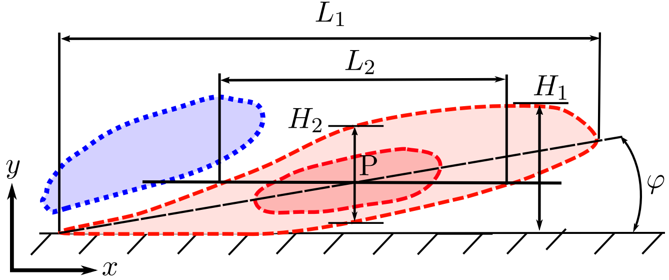

Figure 2.5: Sketch of an exemplary spatial two-point correlation function in the xy-plane. The point P denotes the correlation point, the solid black line a wall-parallel cut-plane. Total correlated structure length L_1, correlated structure length in the cut-plane L_2, correlated structure height H_2 and angle φ with respect to the wall are labelled.

Based on the result from the spatial two-point correlation, the average scales of positive correlated areas can be calculated and labelled. The total length of the positive correlated region in streamwise direction is labelled L_1, the total hight H_1. As indicated in figure 2.5, the total length differs from the measured length when only a cut plane, as indicated by the solid black line, is measured and analysed. Resulting length, width and height calculated from cut planes are labelled as L_2, W_2 and H_2. The angle φ refers to the inclination of a positive correlated region in respect to the wall. Two-point correlations as a measure for spatial scales do not account for statistically distributed changes in size, e.g. a meandering structure, because those are averaged out. Accordingly, the resulting scale is equal or underestimated in comparison to the true spatial extent of a coherent structure.

2.2. Literature review on coherent structures in boundary-layer flows

In this section a literature overview on past research and investigations on coherent structures in turbulent boundary layer-flows is given. In the three sub-sections, the major research subjects of this thesis are covered, followed by their respective research questions which will be addressed in the following chapters of this thesis.

2.2.1. Definition, scaling and dynamics of large-scale structures

There is no universal and exact definition of the term “coherent structure” concerning turbulent boundary layers. In his review paper on coherent structures Robinson (1991) defines a coherent structure as “a three-dimensional region of the flow over which at least one fundamental flow variable (velocity component, density, temperature, etc.) exhibits significant correlation with itself or with another variable over a range of space and/or time that is significantly larger than the smallest local scales of the flow”. Based on this definition, Robinson (1991) distinguishes between eight different types of coherent structures in a turbulent boundary-layer flow:

1. Low-speed streaks in the viscous sub layer ($y^+ < 10$)
2. Ejections of low-speed fluid outward from the wall
3. Sweeps of high-speed fluid inward toward the wall
4. Vortical structures of various forms
5. Internal near-wall shear layers
6. Near-wall “pockets”

7. Large (δ-scale) motions capped by three-dimensional bulges in the outer turbulent/ potential interface
8. Shear-layer "backs" of large-scale outer-region motions

It should be noted here that several of the listed structures are of the same origin or a result of the same structure, as was shown by later research (Adrian, 2007; Wallace, 2012), which will be discussed in the following. The structures 1, 2 and 6 are features of the near-wall cycle. Kline et al. (1967) as one of the first visualised coherent structures near the wall with hydrogen bubbles. They observed that the near-wall flow in a turbulent boundary layer aligns in streamwise streaks of high and low-momentum with a streamwise length between $L_{\text{streak}} \approx 400-1000\frac{\nu}{u_\tau}$. The low-momentum streaks lift up from the wall at a random instance and break up in an instability process. This so called “bursting” process is the key mechanism for turbulence production in the near-wall region and buffer layer. Wallace et al. (1972) analysed hot wire and hot film measurements with the quadrant analysis where turbulent fluctuation combinations $\phi_i'\phi_j'$ are sorted according to their direction. The results show that so called sweep-events (quadrant Q4) with $u' > 0$ and $v' < 0$ and ejection events (quadrant Q2) with $u' > 0$ and $v' < 0$ are the main contributor to Reynolds stress production in the near-wall region, which highlights the importance of coherent structures for the turbulence itself. Furthermore, they observed a sweep-streak interaction in which an inrush of high-momentum fluid from outside (Q4 event) leads to an ejection (Q2 event) of a near-wall streak followed by the described break up and increased turbulence activity. This contradicts the idea that the near-wall cycle is a self-sustaining stand alone feature in the turbulent boundary layer but that interaction between outer flow and the near-wall region takes place. Their early studies describe an instability mechanism of turbulence production, which is different from the mechanism described in the outer boundary layer. Anyhow, these instabilities appear rather seldom and do not explain the total amount of Reynolds stresses produced in the near-wall flow regions of turbulent boundary layers. Based on Kline’s observations, Smith and Metzler (1983) investigated the scaling of the near-wall streaks quantitatively. The spanwise spacing of the near-wall streaks λ_z^+ is approximately $\lambda_z^+ \approx 100$, increasing with the wall distance y. The increase in spacing was explained with varying heights of the near-wall streaks during the upward motion from the wall. Additionally, they found that after a burst of a near-wall streak, low-speed fluid remains close to the wall and creates the basis for the formation of a new near-wall low-speed streak. Smith and Metzler (1983) concluded that the bursting process is self-sustaining and a dominant feature of the near-wall boundary layer.

Evidence for the existence of a different kind of coherent structures in the logarithmic layer were found in experimental investigations decades ago (Grant, 1958; Townsend, 1956). As those structures scale on outer scales with the boundary layer thicknesses δ and can exceed multiple δ in spatial extension, those structures were termed “large-scale structures” (Marusic et al., 2010). About those large-scale coherent structures in the logarithmic layer less is known in contrast to the coherent structures of the near-wall cycle. One particular reason is the mutual size of the structures which can exceed multiple boundary layer thicknesses δ and makes it challenging to capture large-scale structures with experimental and numerical research approaches (Dennis and Nickels, 2011; Smits et al., 2011). Even after years of intensive research, the instantaneous spatial topology of large-scale structures and their statistical impact on the turbulent mixing is still under debate (Marusic et al., 2010; Smits et al., 2011).

Analysing pre-multiplied energy spectra, Hutchins and Marusic (2007a) observed a second peak in the logarithmic layer at a streamwise wavelength of $\lambda_{\text{x}} \approx 6\,\delta$. Due to the long streamwise wavelength, which is significantly longer than the characteristic length δ of the boundary layer, they assumed that this energy peak is associated with large-scale structures elongated in streamwise direction. Using a rake of hot-wire probes, Hutchins and

Marusic (2007b) proved that very long meandering structures occur in the logarithmic layer of a turbulent boundary-layer flow. They named theses coherent regions “superstructures”. With advances in optical measurement techniques, it was possible to capture the large-scale structures visually (Adrian et al., 2000; Hutchins et al., 2012).

Many previous studies rely on Taylor’s hypothesis to reconstruct the large-scale structures. Dennis and Nickels (2008) tested the hypothesis in a turbulent boundary-layer flow at $Re_\theta = 4685$ and a comparison length up to $6\,\delta$ in streamwise direction. Their results show that the reconstruction is precise for the large-scale flow components. In time resolving Stereo-PIV studies using Taylor’s hypothesis to reconstruct the structure length, Dennis and Nickels (2011) showed that the large-scale structures do not exceed $7\,\delta$ length on average, but structures up to $20\,\delta$ were detected as well. Similar structures were found in pipe and channel flows and were termed “very large scale motions (VLSM)” (Kim and Adrian, 1999; Balakumar and Adrian, 2007; Monty et al., 2009). Those VLSM are slightly longer and wider on average compared to the measured scales in boundary layers. The existence of similar structures in different types of wall bounded flows yields that large-scale structures are a characteristic feature of the logarithmic region and outer region of a turbulent boundary-layer flow. Further comparisons between pipe, channel and boundary-layer flows are given in Monty et al. (2009).

In wall-parallel PIV measurements, Tomkins and Adrian (2003) observed that large-scale structures in the logarithmic layer are aligned in a streaky pattern comparable to the low-speed streaks observed by Smith and Metzler (1983) but have much larger spacings in the order of the boundary layer thickness $\mathcal{O}(\delta)$. Also visible in the data of Tomkins and Adrian (2003) and shown later by hot-wire rake measurements from Hutchins and Marusic (2007b) is the meandering behaviour of the large-scale structures. Conditionally analysing PIV data sets at $Re_\tau = 2600$, de Silva et al. (2018) found large coherence in the spanwise velocity within the logarithmic layer but also in the outer boundary layer. They explained this with meandering large-scale structures, which are inclined to the wall and reach up to the outer boundary layer.

In contrast to the magnitude of turbulent fluctuations associated with the near-wall cycle, the average turbulent fluctuations in the logarithmic layer, at the location of the second peak, increase significantly with the Reynolds number (Marusic et al., 2010; Samie et al., 2018). As this second peak in the turbulent fluctuation profile or energy profile respectively occurs at a large streamwise wavelength, it is supposed to be an effect of increased activity of large-scale structures in the logarithmic layer (Hutchins and Marusic, 2007b). Accordingly, large-scale structures gain importance with increasing Reynolds numbers of the observed flow. In a theoretical calculation based on hot-wire results at different Reynolds numbers, Hutchins and Marusic (2007a) estimated a minimum Reynolds number of $Re_\tau = 1700$ to ensure at least an order of magnitude of spatial scale separation between small and large scale structures. Another limit is the existence of the logarithmic layer itself. Considering the boundary layer between $100 < y^+ < 0.15\,Re_\tau$ as the logarithmic layer, a minimum Reynolds number of $Re_\tau = 700$ is necessary for the presence of the logarithmic layer within the turbulent boundary layer (Hutchins et al., 2012). As the upper bound is a function of the friction velocity Reynolds number, the size of the logarithmic layer increases with the Reynolds number. Those two criteria give a lower Reynolds number limit for the investigation of large-scale structures. As maximum Reynolds numbers of current DNS are in the order of $Re_\tau \approx 1300-2000$ (Sillero et al., 2011; Eitel-Amor et al., 2014), the investigation of large-scale structures is primarily dependent on experiments. But also for experiments, achieving higher Reynolds numbers is challenging. According to equation 2.16, either high flow velocities, large boundary layer thicknesses or small kinematic viscosities have to be realised. State of the art wind tunnels enable measurements up to $Re_\tau \sim \mathcal{O}(10^4)$ (Buchmann et al., 2016; Chandran et al., 2017). One approach to investigate turbulent ZPG boundary layers at higher Re_τ in the order of $Re_\tau \sim \mathcal{O}(10^6)$ were the atmospheric surface layer tests (SLTEST) (Hutchins et al., 2012). They proved, using a rake of hot-wires that the statistics scale according to laboratory predictions and using Taylor's hypothesis that the structural pattern is similar to canonical laboratory boundary layers.

Of particular research interest are the dynamics of large-scale structures and their interaction with other coherent structures, e.g. the near-wall streaks, to understand the generation of coherent structures and their effect on the production of turbulence. Comparison of hot-wire signals near the wall and in the logarithmic layer showed a modulating impact of large-scale structures in the outer layer on the near-wall flow (Hutchins and Marusic, 2007b; Mathis et al., 2009). Similar observations were also made by (Schlatter et al., 2009) in DNS and experiments at $Re_\theta = 2600$. Different hints of an interaction between the outer and inner flow are seldom local back-flow events near the wall, found in turbulent boundary layer experiments by Bross and Kähler (2016) and Willert et al. (2018), as well as in DNS of a turbulent pipe flow by Lenaers et al. (2012). Their studies agree that the outer flow has an impact on the appearance of a local reverse-flow event but no generally accepted conclusion or necessary condition can be drawn from their results. Bross et al. (2019) observed in highly resolved 2D and 3D time resolved flow measurements the flow dynamics in the viscous sub-layer, buffer layer and lower logarithmic region. They explained their findings with a conceptual model that explains the interaction of the coherent flow structures and the generation of Reynolds stresses without the instability mechanisms observed before at very low Reynolds numbers.

Research topic 1 - Scaling of large-scale structures in high Reynolds number turbulent boundary-layer flows

As seen in the literature review, the existence of large-scale structures in the logarithmic layer has been proven, but various questions concerning their scaling and interaction are still under debate. One major shortcoming is that many conclusions and observations rely either on single point statistics, low Reynolds number flows or have a limited field of view. Therefore, in a first research step, the scaling and shape of large-scale structures, as exemplariely sketched in figure 2.6, are analysed by means of statistical approaches, e.g. two-point correlations, and observations in instantaneous flow fields derived from optical flow measurements. The aim is to identify characteristic scaling trends in all spatial directions and at different Reynolds numbers. Based on the results conceptual models are derived to explain and understand the scaling. Furthermore, the influence of typical characteristics of a boundary-layer flow such as the intermittentcy and the streamwise momentum of the large-scale structures are taken into account. The results are discussed in chapter 4.

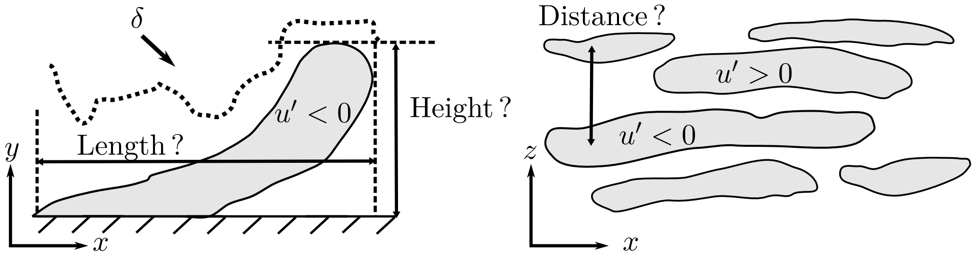

Figure 2.6: Sketch of the scales of large-scale structures concerning research question 1.

2.2.2. Origin of large-scale structures and conceptual models

Many studies also investigated the origin of large-scale structures in the logarithmic layer. The most well known structure-based models of a turbulent boundary layer are the hairpin model (Theodorsen, 1952; Smith, 1984) and the attached-eddy model (AEM) (Townsend, 1956). While the hairpin model allows understanding many aspects of the turbulent motions qualitatively (Adrian et al., 2000; Balakumar and Adrian, 2007), the AEM, first introduced by Townsend (1956) and later extended by Perry et al. (1986) and Marusic and Perry (1995) has been shown to successfully model the single point statistics of turbulent boundary layers, including higher-order statistics quantitatively (Marusic, 2001; Nickels et al., 2007). The AEM, recently reviewed by Marusic and Monty (2019), was originally conceived to represent single point flow statistics in the logarithmic layer based on vortices of arch-like structures that are inclined with respect to the wall. The eddies are supposed to grow with the wall distance and can therefore be considered to be attached to the wall. Energy-containing motions in the flow are described by superposition of the eddies. The original model of Townsend (1956) used generic eddies, whereas the latter improvements by Perry et al. (1986) used more complicated eddy shapes, such as vortex loops or horse-shoe vortices, to also model the spectral energy distribution correctly.

Based on the models, a "bottom up" explanation for the appearance of large-scale structures is provided. Large-scale structures are a result of the alignment of multiple hairpin-shaped vortices into hairpin-packages which introduce low-momentum fluid in their centre according to Adrian (2007). In figure 2.7 a conceptual sketch of the hairpin scenario from Adrian et al. (2000) is shown. The yellow cane or hairpin shaped vortices induce low speed fluid

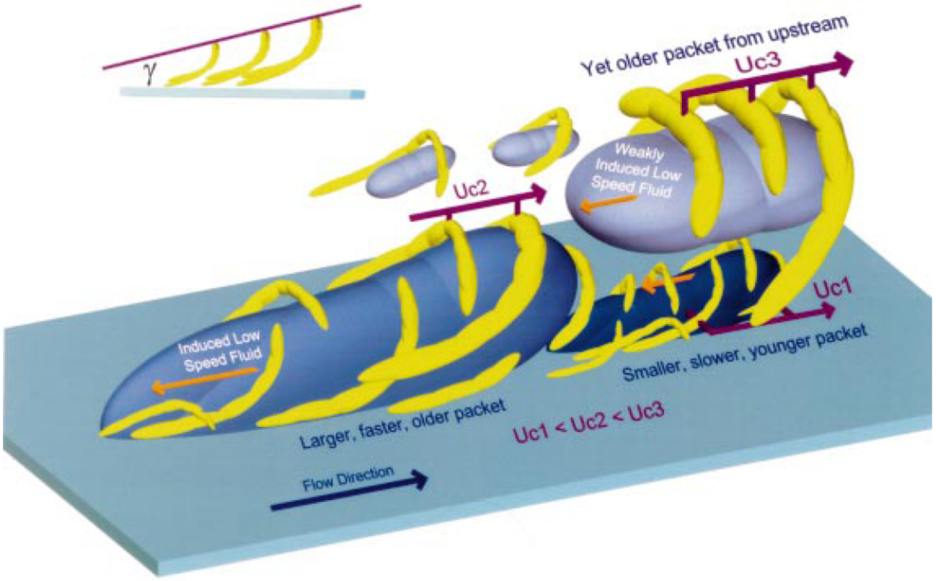
γ
Yet older packet from upstream
Uc3
Weakly Induced Low Speed Fluid
Uc2
Uc1
Induced Low Speed Fluid
Smaller, slower, younger packet
Larger, faster, older packet
Uc1 < Uc2 < Uc3
Flow Direction

Figure 2.7: Conceptual scenario of nested packets of hairpins or cane-type vortices growing up from the wall. These packets align in the streamwise direction and coherently add together to create large zones of nearly uniform streamwise momentum. Large-scale motions in the wake region ultimately limit their growth. Smaller packets move more slowly because they induce faster upstream propagation. Reprinted from Journal of Fluid Mechanics, 422, R. J Adrian, C. D. Meinhart, C. D. Tomkins, Vortex organization in the outer region of the turbulent boundary layer, 1-54, Copyright (2000), with permission from Cambridge University Press.

(blue) in their centres, which has a different spatial extension depending on the wall distance and age of the hairpin package. Very long structures, which exceed multiple boundary-layer thicknesses in streamwise length, are explained as an alignment of multiple hairpin-packages in streamwise direction (Marusic, 2001; Adrian, 2007). The concept of arch- or hairpin-like flow structures were derived from extended flow visualisations at low Reynolds numbers using hydrogen bubbles or smoke (Kline et al., 1967; Head and Bandyopadhyay, 1981). These visualisations show the Lagrangian flow properties, while more recently, PIV measurements revealed the existence of these structures through an Eulerian description (Adrian et al., 2000; Ganapathisubramani et al., 2003).

These models rely on the chosen representative vortical structures, which are tailored in size, strength, inclination angle, wall-normal extension and spatial distribution based on observations from numerical and experimental work. Due to the simplicity of the analytical models, they have a limited predictive capacity but provide insights into scaling behaviours even at high Reynolds numbers where simulations and experiments are impossible or at least hard to obtain. The flow fields predicted by the models are strongly dependent on the chosen eddies or vortex structures. For example, a notable difference between the models is that the hairpin model has long legs elongated in the streamwise direction which cause the well known streaky flow pattern in the streamwise velocity component as outlined in Waleffe (1998).

Even though much evidence for hairpins was found in turbulent boundary layers, this explanation raises many questions, e.g. why structures tend to align in packages or why a statistically random flow should consist of a hierarchical structure pattern. For turbulent flows at low Reynolds numbers, the bottom up model where large-scale structures are formed initially near the wall and grow seems plausible, whereas for high Reynolds number flow, where the separation of scales is large, it tends to be non-physical that structures grow multiple orders of magnitude while convecting downstream in the turbulent boundary layer (Hutchins et al., 2012). Hence, different explanations, which can be best refered as “top down models”, were proposed (Hunt and Morrison, 2000). The top-down view could be described as a sweep-streak interaction in which a sweep of outer layer fluid interacts with flow closer to the wall which leads to a blockage within the flow and creates streamwise vortices as well as small scale turbulence. It is still not clear which mechanism is dominant or if both mechanisms might exist simultaneously in the turbulent boundary-layer flow (Hutchins et al., 2012). Hunt and Morrison (2000) assume that the top-down mechanism is predominant at $Re_\tau > 10000$ or on flow over rough walls, but their conclusions are mainly based on observations and atmospheric data because of the lack of high Re_τ laboratory data for TBL flows.

Research topic 2 - Conceptual models to explain the origin of large-scale structures

The common explanations for the generation and scaling of large-scale structures still raise many open questions. The questions can be targeted by two principal approaches, either improving an existing conceptual boundary-layer model to better understand the structure scaling and origin or find new explanations based on dynamic interactions within the boundary layer. Therefore in chapter 5 the first approach is chosen. The spatial representation of a turbulent boundary-layer flow based on the attached-eddy model is analysed and compared to experimental data towards an improved spatial representation of a boundary layer from the attached-eddy model.

In chapter 6 the second approach is followed. The flow field around a large-scale structure and characteristic flow events, such as ejection or sweeps, are investigated and discussed towards the question of the origin of large-scale structures. The PIV data enables the study of the vortical structure in the vicinity of a large-scale structure, as highlighted in figure 2.8.

The observations yield new insights in the dynamics associated with large-scale structures. Furthermore, a self-sustaining process is introduced as a conceptual model based on the observations and vortical patterns in the flow, which explains the generation of large-scale structures based on an instability mechanism.

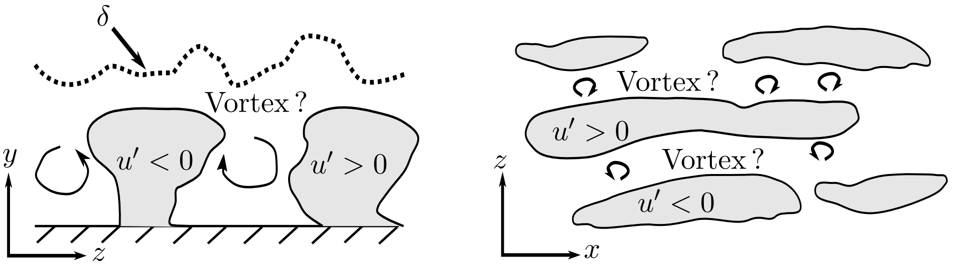

Figure 2.8: Sketch of vortices around large-scale structures concerning research question 2.

2.2.3. Structure of adverse pressure gradient turbulent boundary-layer flow

Turbulent boundary-layer flows under an APG influence differ in many aspects from boundary-layer flows under ZPG (Schlichting and Gersten, 2006; Harun et al., 2013). Their modelling and description is more challenging, as the known similarity and scaling laws mainly rely on the self-similarity of a ZPG boundary layer. Boundary-layer flows, which are subject to an APG for a longer streamwise distance are the most difficult cases, because neither the known scaling laws fit nor is the boundary layer separated, as it is the case for very strong APG conditions (Skåre and Krogstad, 1994). There are multiple experimental as well as numerical studies in literature with regard to APG turbulent boundary-layer flows, but most rely on single-point statistics to analyse APG turbulent boundary-layer flow scaling and scaling laws with comparison to ZPG turbulent boundary-layer flows (Skåre and Krogstad, 1994; Monty et al., 2011; Knopp et al., 2015; Maciel et al., 2018). Another shortcoming of most studies is the limitation to low Reynolds numbers.

In flows with large positive streamwise pressure gradients $\mathrm{d}p/\mathrm{d}x > 0$ but without flow separation, the known similarity laws and scalings are not applicable (Skåre and Krogstad, 1994; Maciel et al., 2018). In comparison to ZPG turbulent boundary layer flows, the logarithmic layer shrinks and the scaling constants κ and B change (Knopp et al., 2015; Nickels, 2004), until the breakdown of the logarithmic law takes places. Maciel et al. (2018) compare different scaling laws and parameters for small and large defect turbulent boundary layers. Based on the findings, Maciel et al. (2018) propose the use of a new set of consistent scaling parameters, which are the pressure gradient parameter β_0, Reynolds number Re_0 and inertia parameter α_0.

Besides the scaling, the effect of the APG strength on the turbulent boundary-layer flow was investigated. Monty et al. (2011) did a parametric study comparing APG turbulent boundary-layer flows at different pressure parameters between $0 \leq \beta \leq 4.74$. They observed a vanishing of the logarithmic layer in the TBL and an increase of the second peak in the turbulence intensity profile with increasing APG. They explained the rise in the second peak with an energisation of large-scale structures under an APG comparable to an increase of the Reynolds number under ZPG conditions. Earlier studies by Skåre and Krogstad (1994) investigated turbulent boundary-layer flows under an APG near separation. By adjusting the experimental parameters carefully, they tried to achieve self-similar conditions, which was nearly fulfilled. Comparing the Reynolds stress ratios, no significant change to ZPG conditions was found, which suggests that the energy distribution between flow components is not changed by the pressure gradient. Furthermore, dissipation and production of turbulence was measured. The production and dissipation is not limited to the near-wall region under an APG. For the production profile a second peak at a higher wall distance is present. Both observations suggest that a change in the structural pattern or interaction processes takes place in an APG turbulent boundary layer. In simulations over a wing section, Vinuesa et al. (2017) confirmed the findings of Skåre and Krogstad (1994) and Monty et al. (2011) at matched pressure gradient parameters β.

In their following study, Krogstad and Skåre (1995) investigated AGP boundary-layer flows from a structural aspect. Using the quadrant analysis, a significant increase of Q4 events was detected. When analysing only the strongest events, an increase in Q1 events was also found. This supports the idea that under an APG reflection of large-scale structures at the wall takes place, which is not present under ZPG. Using two-point correlations to analyse the structure shape, also differences between APG and ZPG turbulent boundary-layer flows were detected. In the spanwise wall-normal plane (yz-plane) a round shape of the $R_{u'u'}$ correlation coefficient occurs close to the wall. This was explained with a squeeze of inrushed fluid associated with the increased Q4 activity.

Studies analysing TBL under different pressure gradients form an energetic viewpoint were done by Harun et al. (2013). Comparing pre-multiplied energy spectra for ZPG, APG and FPG flows, no change in the shape of the spectra is found but the overall energy in the outer region is increased under APG conditions. This suggests that the large-scale structures do not change in character but in strength under pressure gradient influence (Harun et al., 2013). Under an APG, large-scale structures are energised, comparable to a rise of the Reynolds number under ZPG (Harun et al., 2013; Monty et al., 2011). These effects are also visible in figure 2.9, where the broadband turbulent intensity profiles from an APG boundary layer at $Re_\tau = 1900$ are shown. The profiles are decomposed in a small-scale component and a large-scale component, separated at the streamwise wavelength $\lambda_x = \delta$. While only a small increase in turbulence activity is present for the small scale components in the boundary layer at $z^+ > 100$, the intensity of the large-scale components increases significantly with the APG. In line with the energising of large-scale structures, Harun et al. (2013) also found an increased modulation of small scales by large-scale structures when the flow is under an APG influence.

One shortcoming of most of the afore cited studies is the lack of multi-point information because multi-point statistics yield better insight in the turbulent structural pattern and turbulence production. The data is acquired with hot-wire probes and therefore only single-point statistics are possible. A unique study investigating APG turbulent boundary-layer flows was performed in the LML wind Tunnel in Lille (Hain et al., 2016; Cuvier et al., 2017). Combining 16 cameras, an evolving boundary layer over more than 6 m in streamwise direction was captured optically by means of PIV. The utilisation of multiple cameras enabled sufficient spatial resolution even for the very long measurement domain. Another advantage is that the evolution of the boundary layer under APG conditions was observed consistently. Their measurements confirm a second peak in the turbulent production profile which evolves further away from the wall as the boundary-layer flow develops under the APG. Kitsios et al. (2017) used self-similarity under APG conditions to perform a DNS of an APG turbulent boundary-layer flow at the verge of separation. They compare mild APG ($\beta = 1$), strong APG ($\beta = 39$) to a ZPG boundary layer. With increasing pressure gradient, an increase of the wake region between the logarithmic layer and the free stream outer flow, and a decrease of the logarithmic layer itself were observed. They also confirm a stronger outer peak further outside and observed using multi-point statistics changes in the structure pattern, e.g. a shortening of the structures and an increase in principle angle with respect to the wall up

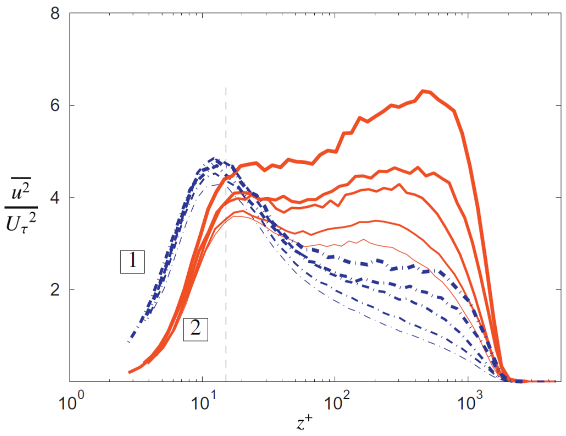

Figure 2.9: Turbulent intensity profiles at $Re_\tau = 1900$ decomposed into a small-scale component with wavelengths $\lambda_x > \delta$ (broken lines) and a large-scale component with wavelengths $\lambda_x < \delta$ (solid lines). The thinnest line represents the ZPG case, the thickness of the line grows with the strength of APG. Wall distance is denoted with z. Reprinted from International Journal of Heat and Fluid Flow, 32/3, J.P. Monty, Z. Harun, I. Marusic, A parametric study of adverse pressure gradient turbulent boundary layers, 575-585, Copyright (2011), with permission from Elsevier.

to 27°. Their observations hint, that APG turbulent boundary-layer flows become more like free shear layer flows than wall bounded flow with increasing pressure gradient.

With increasing impact of the APG, the inflexion of the mean velocity profile in streamwise direction increases. The boundary-layer flow finally can't follow the wall contour but separates (Schlichting and Gersten, 2006). Most studies considering flow separation focus on specific problems, e.g. flows over wings, or on geometry-induced separation, which is not comparable to the flow-induced separation due to increasing APG (Simpson, 1989; Simmons et al., 2019).

Many of the previously mentioned studies focus on APG on the verge of separation, e.g. Skåre and Krogstad (1994); Kitsios et al. (2017), but not on the separated boundary-layer flow itself. Simpson (1989) compares in his review different methods to characterise the separation. He concludes that the structure of a separated and attached flow differ strongly. The main turbulent stresses occur in the middle of the shear layer and are mainly contributed by large-scale structures. Furthermore, they observe a coupling between pressure and velocity fluctuation as well as the energy supplied by the outer flow. In an experimental study, Elyasi and Ghaemi (2019) investigated a turbulent boundary flow with pressure gradient up to flow separation using planar and tomographic PIV. Analysing the structures conditionally they observed a saddle point structure of the stream-lines, as also observed by Simmons et al. (2019) using visualisation techniques. Applying POD to their data, Elyasi and Ghaemi (2019) showed about 42 % of the turbulent kinetic energy is due to large-scale activity with high spanwise motions. It must be noted here that the investigated flow by Elyasi and Ghaemi (2019) must be considered as an influenced boundary-layer flow by the opposite wind tunnel wall, due to the low aspect ratio of the used wind tunnel (Jones et al., 1995).

Research topic 3 - How do large-scale structures react on an adverse pressure gradient impact

Based on the literature survey on adverse pressure gradient boundary layers, it is clear that the pressure gradient changes boundary layer characteristics and has an influence on the structures as well, as exemplarily sketched in figure 2.10. Therefore, in chapter 7, a turbulent boundary-layer flow under an adverse pressure gradient is investigated. The aim is to examine the effect of strong APG conditions on large-scale motions in turbulent boundary layers in comparison to structures in canonical ZPG boundary layers and to resolve, characterise and understand the interaction between large-scale structures and and a beginning flow separation.

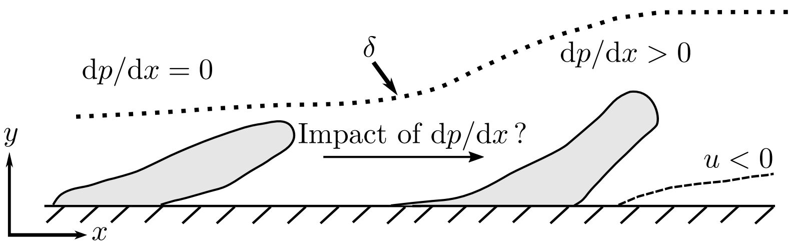
$\mathrm{d}p/\mathrm{d}x = 0$
δ
$\mathrm{d}p/\mathrm{d}x > 0$
y
Impact of $\mathrm{d}p/\mathrm{d}x$?
$u < 0$
x

Figure 2.10: Sketch of large-scale structures under pressure gradient impact concerning research question 3.

3

Experimental facility and measurement setups

In line with the Deutsche Forschungsgemeinschaft (DFG) funded research project “Analysis of turbulent boundary layer subject to pressure gradients at high Reynolds numbers using multiple high resolution camera systems”, turbulent boundary-layer flows are investigated. Focus of this study is to analyse large-scale coherent structures in the logarithmic-layer and outer turbulent boundary layer. As outlined in the introduction and in chapter 2, the understanding of a turbulent boundary-layer flow and especially the structural patterns are crucial for the understanding of turbulence itself, to further improve simulations and technical applications. Most past studies are either limited to low Reynolds numbers or are based on single-point analysis tools, as discussed in the literature reviews on past research and achievements given in section 2.2. For this study, high Reynolds number turbulent boundary layer flows are investigated with advanced optical measurement techniques. The experiments were performed in the Atmospheric Wind Tunnel Munich, where friction velocity Reynolds numbers up to $Re_\tau = 13400$ can be reached. This Reynolds number is an order of magnitude higher than the limit of current numerical studies, as shown in figure 3.1 (Eitel-Amor et al., 2014). Within the facility, it is possible to study turbulent boundary-layer flows experimentally at technically relevant conditions. Details on the wind tunnel are given in section 3.1.

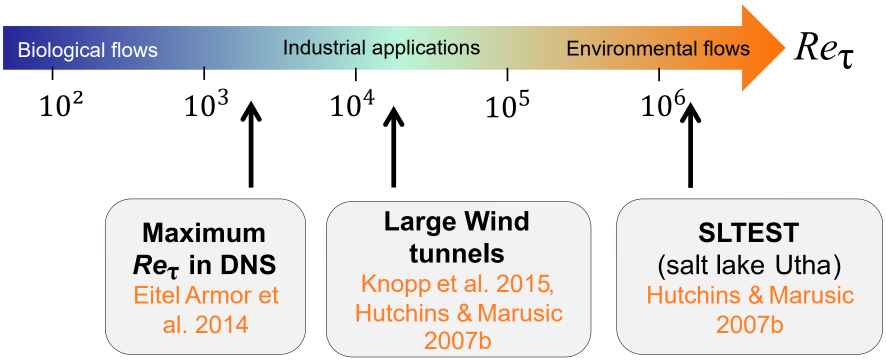
Biological flows
Industrial applications
Environmental flows
Re_τ
10^2
10^3
10^4
10^5
10^6
Maximum Re_τ in DNS
Eitel Armor et al. 2014
Large Wind tunnels
Knopp et al. 2015, Hutchins & Marusic 2007b
SLTEST (salt lake Utha)
Hutchins & Marusic 2007b

Figure 3.1: Friction Reynolds number ranges in turbulent boundary layer flows.

For the analysis of different pressure gradients the side wall of the wind tunnel was equipped with two different boundary-layer models. These models are contractions of the wind tunnel cross-section which lead to a defined pressure-gradient distribution within the boundary layer.

The parameters for model geometry and similarity numbers are described in section 3.2. An overview of the measurements performed on the boundary-layer models is given in section 3.3.

As this work focuses on large-scale coherent structures it must be ensured that for all experimental set-ups the large-scale structures are fully covered, including smaller secondary effects associated with the presence of a large-scale structure. Therefore, in section 3.4 the expected scales of turbulence within the boundary layer are estimated and compared with the resulting field of view and spatial resolution of the measurements. To ensure fully developed turbulent boundary layers and to test new experimental techniques and analysis tools, e.g. local boundary layer seeding with masking of laminar parts, preliminary investigations were necessary. The description of the preliminary tests including the relevant results is explained in section 3.5.

In addition to the planar PIV measurements described in this chapter, three-dimensional particle tracking measurements were performed to detect a large volume within the turbulent boundary layer. Since this experiment uses a different measurement technique, a different seeding system and a different data evaluation technique, the set-up and results are described separately in chapter 8. In addition to the investigation of large-scale structures the main focus of this additional experiment was to test new measurement techniques, which are able to capture large volumes within a boundary-layer flow.

3.1. Atmospheric Wind Tunnel Munich

The experiments presented in this dissertation were performed in the **A**tmospheric **W**ind Tunnel **M**unich (AWM), an Eiffel-type wind tunnel at the Bundeswehr University Munich. A sketch of the wind tunnel is shown in figure 3.2. The wind tunnel has a 22 m long test section with a cross-sectional area of $1.85 \times 1.85\,\mathrm{m}^2$. As the boundary layer development length is several meters before the test point, a large boundary layer thickness δ_{99} of $0.10 - 0.25\,\mathrm{m}$ can be achieved at the measurement locations. This results in a ratio between the wind tunnel width and the boundary layer thickness greater than seven, which, according to Jones et al. (1995) is sufficient to ensure that there is no influence of the opposite wind tunnel wall on the measurements.

In front of the test section a settling chamber and a nozzle with a contraction ratio of 9 : 1 is installed. Within the settling chamber three screens with decreasing mesh sizes are built in for flow conditioning. As the open-area ratio of the last screen is 0.66 no artificial vortices which disturb the natural boundary layer development are expected (Bradshaw, 1965). The flow conditioning and flow contraction result in free stream turbulence intensities of approximately $Tu < 0.2\,\%$ in the free stream at $u_\infty = 38\,\mathrm{m/s}$ (Schulze, 2012).

During the measurements the environmental parameters are monitored and logged. Humidity and temperature are measured with an Ahlborm Alemo MH8D46 anemometer. The uncertainty for the temperature measurement is $\pm 0.4\,\mathrm{K}$ and $\pm 1.8\,\%$ of relative humidity in the relevant measurement ranges. The static pressure and dynamic pressure are measured with a Prandtl tube at the beginning of the test section and captured with a Setra High Accuracy Low Differential Pressure Transducer having an accuracy of $0.073\,\%$ according to the manufacturers specification.

For the PIV measurements the insertion of seeding/ tracer particles is necessary. For the measurements described in section 3.3 either a global seeding inserted in the wind tunnel inlet tower or a local seeding system, which is further described and qualified in section 3.5, were used. The seeding particles are oil droplets generated from Di-Ethyl-Hexyl-Sebacat (DEHS) with Laskin nozzle seeders, which results in mean particle sizes of approximately $1\,\mu\mathrm{m}$ (Kähler et al., 2002). The advantage of oil droplets is their long persistence in air, the

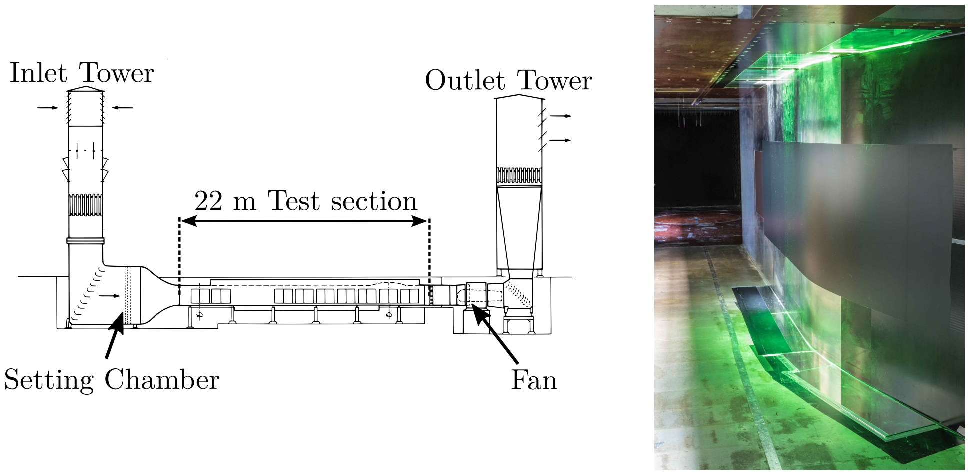

Figure 3.2: Left: Sketch of the Atmospheric Wind Tunnel Munich. Right: Upstream view of the test section with the aluminium boundary-layer model 2 on the side-wall.

simple generation and good time response on acceleration of the flow due to a small Stokes drag (Raffel et al., 2018). The velocity lag u_s due to the Stokes drag is defined as

$$u_\mathrm{s} = u_\mathrm{TP} - u = d_\mathrm{TP}^2 \left(\frac{\rho_\mathrm{TP} - \rho_\mathrm{F}}{\mu} \right) \cdot a \tag{3.1}$$

with the particle diameter d_TP, particle velocity u_TP, particle density ρ_TP, fluid density ρ_F and viscosity μ (Raffel et al., 2018). Using small seeding particles, e.g. DEHS droplets, the velocity lag is little because of the small particle diameter d_TP, hence, a matched density between particle and fluid is secondary as long as buoyancy effects can be neglected. The disadvantage of using seeding particles for PIV purposes which have diameters in the order of $1\,\mu$m is limitation to fields of view (FOV) of approximately $1000 \times 750\,\mathrm{mm}^2$ when a standard Nd:YAG laser is used. The reason is the limited light scattering behaviour and increased occurrence of peak locking due to small particle images (Raffel et al., 2018). For the volumetric measurements described in chapter 8, even less light was provided due to the volumetric illumination. Therefore, helium filled soap bubbles (HFSB) were used as tracer particles due to better light scattering properties. Details on the generation, insertion and characteristics are given separately in table 3.3.

3.2. Boundary-layer models

Focus of this study is the investigation of the scaling and pressure gradient influences on large-scale structures in turbulent boundary layers. To generate pressure gradients the wind tunnel side wall was modified with boundary-layer models consisting of two S-shape deflections. The upwind deflection accelerates the flow and is followed by a flat plate part with zero pressure gradient (ZPG). On the downwind S-shape deflection, the wind tunnel cross section is opened again resulting in a well defined adverse pressure gradient (APG). In the following subsections 3.2.1 and 3.2.2, the two different boundary-layer models, at which the experiments were conducted, are presented. While Model 1 has the focus on attached turbulent boundary-layer flows, the adverse pressure gradient was increased for Model 2 resulting in flow separation. Dimensionless flow parameters as the Reynolds number and Clauser parameter are calculated for each set-up and will be used to denominate the different data sets in the following sections. The measurement set-ups and PIV evaluation are presented in section 3.3.

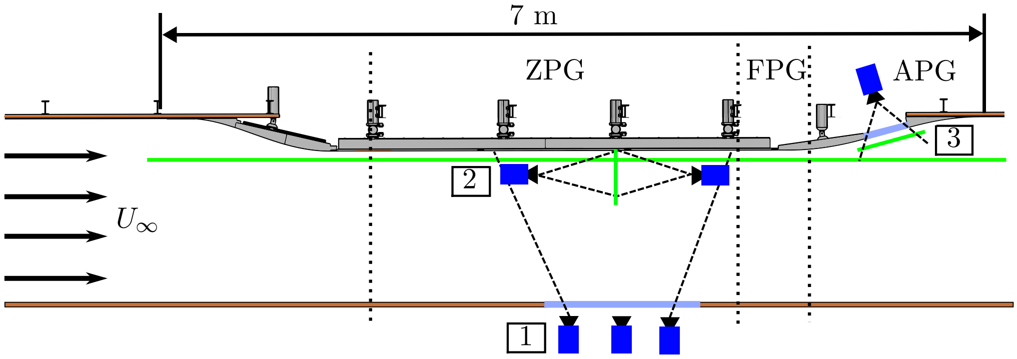

Figure 3.3: Sketch of boundary-layer model 1 (grey). Upstream and downstream of the flat plate sections, the S-shape deflections are visible. The dotted lines indicate the different pressure regimes over the model contour. In the ZPG section the set-up of the wall parallel measurement (1) and stereo PIV measurement (2) are shown exemplary, in the APG section the wall parallel measurement (3).

As the surface of the boundary-layer models is bent and not identical with the wind tunnel side wall and the measurements are taken at various positions along the boundary-layer model, the use of the wind tunnel fixed Cartesian x, y, z-coordinate system is not appropriate for the data evaluation. Therefore, a model fixed cartesian x^*, y^*, z^*-coordinate system is defined. The x^*, y^*, z^*-system is placed in a way that the x^*-direction is always model wall parallel and the y^*-direction normal to the wall. Hence, the system is rotated in z-direction relative to the x, y, z-system, which results in identical spanwise directions $z = z^*$. The origin of the x^*, y^*, z^*-system is shifted on the model wall to the position (x_0, y_0). The relative position x_0 in streamwise direction is given separately for each measurement in section 3.3.

3.2.1. Model 1 - RETTINA

Boundary-layer model 1 was designed and built in cooperation with the German Aerospace Centre (DLR) Göttingen in line with the **Re**liable **T**urbulence and **T**ransition Modelling for **In**dustrial **A**erodynamic (RETTINA) project (Knopp et al., 2014, 2015). The purpose of the model was to investigate the influence of a moderate adverse pressure gradient on a fully developed turbulent boundary-layer flow. This is realised by two S-shape flow deflections as mentioned previously. In figure 3.3 a sketch of the RETTINA model is shown. The dashed lines indicate the regions with different pressure gradient regimes. For the utilisation of optical measurement techniques multiple optical accesses are built into the model and wind tunnel wall near the model as shown in figure 3.3. In addition to the windows within the model and the wind tunnel side wall, the ceiling of the wind tunnel is equipped with windows between $x = -4\,\text{m}$ and $x = 0\,\text{m}$.

To ensure canonical ZPG conditions and to qualify the strength of the APG, pressure measurements were performed over the model with a DTC Initium System. For static pressure measurements the uncertainty of the pressure gauge is $\sigma \pm 0.1\,\%$ for wind tunnel measurements with pressure above 10 psi according to the manufacturer's data sheet. This results in an absolute uncertainty of $\sigma_\text{p} \approx \pm 950\,\text{Pa}$. In figure 3.4 the resulting pressure gradient distribution is plotted. Over the flat plate section approximately 2 m of pure ZPG boundary layer is achieved. The strength APG at the downstream end is not constant but reaches a maximum 1.1 m upstream of the model end at $x = 0$. The APG increases strongly with the inflow velocity and thereby the chosen Reynolds number. An overview of the dimensionless similarity parameters for the quantification of the pressure gradient are given in table 3.1.

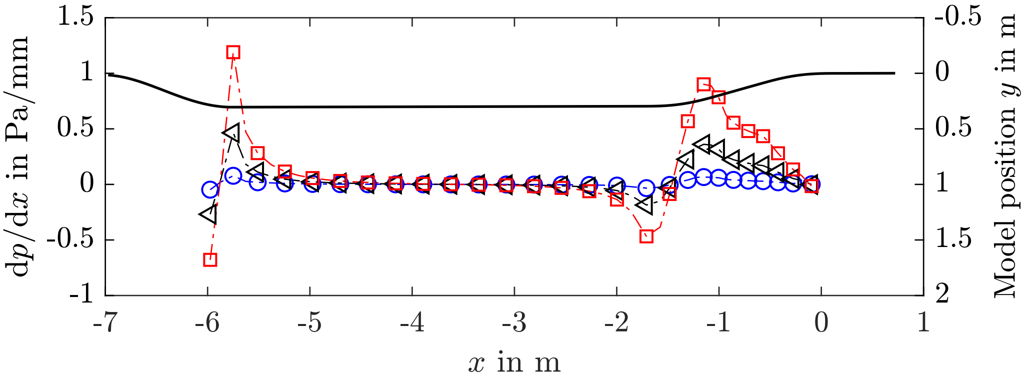

Figure 3.4: Pressure gradient distribution dp/dx over model 1. Symbols correspond to different Reynolds numbers: ○ : $Re_\tau = 4200$, △ : $Re_\tau = 9300$, □ : $Re_\tau = 13400$. The solid black line shows the model geometry.

Table 3.1: Flow parameters of the experiments on model 1

u_0 (m/s)	u_∞ (m/s)	$Re_{\tau,\mathrm{ZPG}}$	$u_{\tau,\mathrm{ZPG}}$ (m/s)	$\delta_{99,\mathrm{ZPG}}$ (m)	$\delta_{99,\mathrm{APG}}$ (m)	Δp_x^+	β	$1/y^+_{\mathrm{ZPG}}$ (μm)	$1/y^+_{\mathrm{APG}}$ (μm)
9.8	12	4400	0.44	0.145	0.210	0.044	24	34.7	74.5
23.2	27.9	9700	0.97	0.148	0.220	0.0145	21	15.9	30
36	43	13800	1.45	0.142	0.211	0.010	22	10.7	18.9

To investigate the influence of the Reynolds number the measurements were taken at three different flow velocities, which result in friction velocity Reynolds numbers of $Re_\tau = 4200$, 9300 and 13400. The friction velocity u_τ was estimated form a Clauser-Chart fit with the log constants $\kappa = 0.385$ and $B = 4.1$ (Österlund et al., 2000) at position $x = -3.1\,\mathrm{m}$ in the ZPG section. Based on the Clauser-Chart fit the wall shear stress τ_w was estimated according to equation 2.14. In table 3.1 a summary of the experimental parameters is given for the ZPG and APG measurement parameters separately. To characterise the strength of the pressure gradient, in case of the APG measurements, the dimensionless pressure gradient Δp^+ and Clauser pressure gradient parameter β

$$\Delta p_x^+ = \frac{\nu}{\rho u_\tau^3}\frac{\mathrm{d}p}{\mathrm{d}x}; \quad \beta = \frac{\delta^*}{\tau_\mathrm{w}}\frac{\mathrm{d}p}{\mathrm{d}x} \tag{3.2}$$

are calculated at the x_0 position,which are denoted in table 3.3. The velocity u_0 corresponds to the the free stream velocity at the beginning of the wind tunnel test section before the contraction of the model and was measured via a Prandtl tube. The free stream velocity over the model is denoted with u_∞.

3.2.2. Model 2 - VicToria

Boundary-layer model 2 is the consequent continuation of boundary layer research under APG impact. As the focus of the model 1 investigations was on attached boundary-layer flows, the APG impact was increased resulting in flow separation. To achieve the increase in APG the model was shifted into the wind tunnel and increased in length in upstream direction.

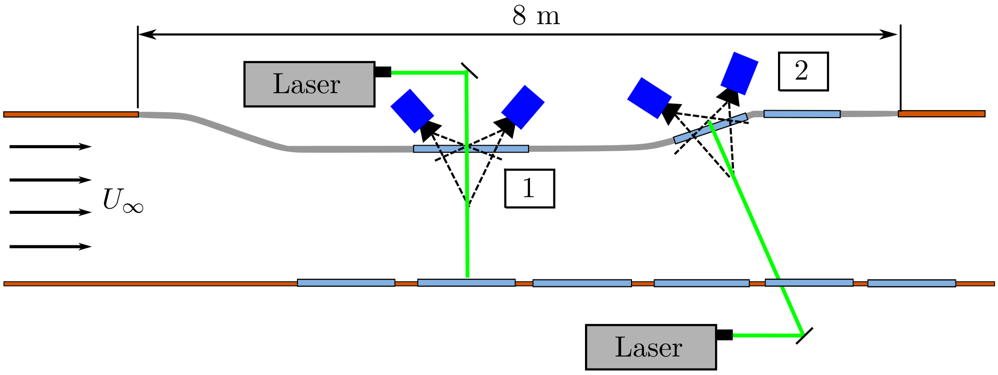

Figure 3.5: Sketch of the boundary-layer model 2 (grey). Two exemplary SPIV measurement set-ups are shown in the ZPG (1) and APG (2). At the downstream end, the sharp edge in the transition to the original wind tunnel wall is visible.

Furthermore, the diffuser half-angle of the straight APG section was increased from 14.4° at model 1 to 18.85° at model 2. The APG of model 2 ends in a sharp edge at $x = 0\,\mathrm{m}$ to stabilise the separation bubble, where model 1 in contrast has a continuous transition from the APG section to the wind tunnel wall. Model 2 was also designed and built in cooperation with the DLR within the Virtual Aircraft Technology Integration Platform (VicToria) project. A sketch of the model with exemplary measurement set-ups is shown in figure 3.5. Besides the change of the model geometry, multiple new windows in the opposite wind tunnel side wall and in the model itself were added to improve the optical access and enable stereo PIV with improved camera positions and angles as well as tomographic measurement set-ups of large flow volumes.

To quantify the pressure gradient distribution and ensure canonical ZPG conditions over the flat plate, similar pressure distribution measurements as for model 1 were conducted with the DTC Initium system described above. The resulting pressure gradient distribution is plotted in figure 3.6. The qualitative pressure gradient distribution is similar to the distribution over model 1 and the maxima of the APG are in the same order of magnitude, but the length of the APG impact is increased. Starting from $x = 0\,\mathrm{m}$ in upstream direction the slope of the pressure gradient $\mathrm{d}p/\mathrm{d}x$ is horizontal, which is a result of the flow separation. Downstream of the sharp edge at $x = 0\,\mathrm{m}$ the flow reattaches and a change of the APG is detectable again.

In table 3.2 the resulting experimental parameters for the model 2 investigations are given. As discussed in section 2.2, large-scale structures are more energetic at high Reynolds numbers. Therefore, for the $Re_\tau = 4100$ case with inflow velocity of $u_0 = 10\,\mathrm{m/s}$, only the pressure gradient distribution and mean flow parameters of the ZPG were measured and evaluated. The further evaluation is focused on the more relevant high velocity flow cases with $Re_\tau = 8400$ and $Re_\tau = 12000$.

As the APG section is subject to flow separation, the classical scaling approaches based on viscous units can't be applied, because calculating the friction velocity u_τ via a Clauser chart fit is impossible with acceptable uncertainty for several reasons. The Clauser chart approach works well for a ZPG flow with multiple data points in the logarithmic layer and known similarity parameters κ and B. In contrast for the APG in model 2, the logarithmic-layer is vanishing and the similarity parameters are under discussion (Knopp et al., 2015). Hence, comparison parameters as Δp_x^+ and β are not defined for the APG of model 2. A detailed analysis of the turbulent boundary layer in the separated APG is given in section 7.2.

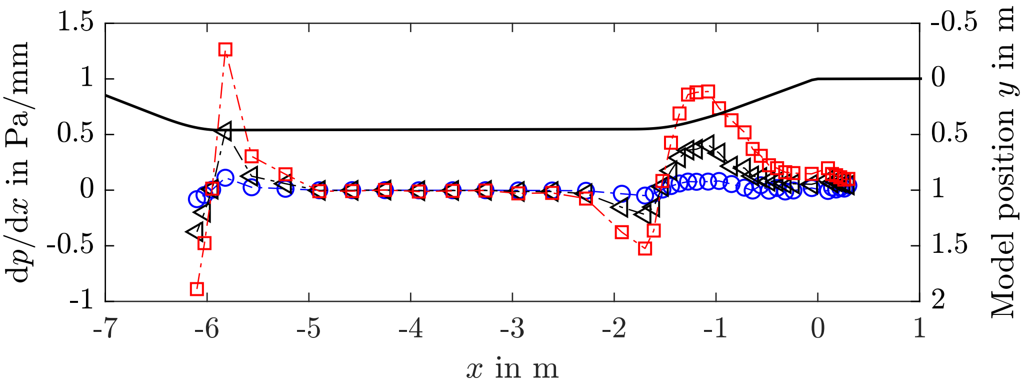

Figure 3.6: Pressure gradient distribution dp/dx over model 2. Symbols correspond to different Reynolds numbers: ○ : $Re_\tau = 4100$, △ : $Re_\tau = 8400$, □ : $Re_\tau = 12000$. The solid black line describes the model geometry.

Table 3.2: Flow parameters of the experiments on model 2

u_0 (m/s)	u_∞ (m/s)	$Re_{\tau,\mathrm{ZPG}}$	$u_{\tau,\mathrm{ZPG}}$ (m/s)	$\delta_{99,\mathrm{ZPG}}$ (m)	$\delta_{99,\mathrm{APG}}$ (m)	$1/y^+_{\mathrm{ZPG}}$ (μm)
9.8	13.3	4100	0.50	0.123	—	29.9
23.1	31	8400	1.12	0.112	0.248	14.0
36	47.9	12000	1.65	0.107	0.24	9.2

3.3. Measurement Setups

Multiple standard 2D2C PIV and stereo 2D3C PIV (SPIV) measurements were conducted on both models. In this section the planar PIV set-ups are described and discussed. The volumetric time resolving measurement set-up is separately explained and described in chapter 8. To analyse large-scale structures in their full spatial extent, a large field of view (FOV) with sufficient spatial resolution must be captured. Therefore, multiple cameras were used in a side by side arrangement. The cameras were either PCO.edge 5.5 sCMOS cameras with a sensor size of 2560 × 2160 pixel and an acquisition rate of 10 Hz or PCO4000 cameras with a sensor of 4008 × 2672 pixel and an acquisition rate of 2 Hz. Illumination was provided by a Spectra Physics Nd:YAG LASER with 400 mJ pulse energy and a repetition rate of 10 Hz or an Innolas Spitligth 400 with 140 mJ pulse energy. The light-sheet thicknesses were approximately 1 mm for the wall-parallel and 2 mm for the SPIV measurements. Ensuring long focal distances, a nearly constant light-sheet thickness even for the large FOV measurements was achieved. The ratio between the light-sheet thickness d_L and the boundary layer thickness δ_{99} is about $\frac{d_\mathrm{L}}{\delta_{99}} \approx 6.9 \cdot 10^{-3}$. Thereby, it is possible to analyse discrete wall-parallel cut planes in the boundary layer.

In addition to the classical PIV measurements, time resolved Stereo PIV (TR-SPIV) was performed over the ZPG of model 2 to get an improved insight into the dynamics of the large-scale structures. Only the middle Reynolds number of $Re_\tau = 8400$ was measured. The illumination for this specific measurement was provided with a Double Head Photonics DM150-532 laser, having an average power of 150 W at 10 kHz. For the experiments a repetition rate of 20 kHz was set using both laser heads intermittently to achieve better il-

Table 3.3: Experimental equipment and positioning of the experiments

Model	Case	Images	Cameras	Laser	Seeding	x_0 (m)
1	ZPG (x^*z^*)	14000	3×PCO.edge	Spectra	global	-3.1
1	ZPG (y^*z^*)	10000	2×PCO4000	Innolas	local	-3.1
1	APG (x^*z^*)	15000	2×PCO.edge	Spectra	local	-0.45
1	APG (y^*z^*)	15000	4×PCO4000	Spectra	local	-0.45
1	Seeding Test	3000	1×PCO.edge	Innolas	both	-3.1
2	ZPG (y^*z^*)	14000	4×PCO.edge	Innolas	both	-3.8
2	APG (y^*z^*)	13650	4×PCO.edge	Innolas	global	-0.43
2	APG (y^*z^*)	4500	4×PCO.edge	Innolas	global	-0.35
2	APG (y^*z^*)	4500	4×PCO.edge	Innolas	global	-0.27
2	APG (x^*y^*)	10000	2×PCO.edge	Innolas	global	-0.35
2	APG (x^*z^*) (TR)	50000	Phantom v2640	Photonics	global	-0.39
2	ZPG (y^*z^*) (TR)	420000	2×Photron SA-Z	Photonics	global	-3.8

lumination of the PIV images. Two Photron SA-Z cameras were set up in a 45° stereo PIV set-up to capture the images. Cropping the camera sensor to 1024×600 pixel a field of view of $0.08 \times 0.16\,\mathrm{m}^2$ was captured for 3.5 s per run. This is equal to $\tau_\delta = u_\infty/\delta_{99} \approx 940$ boundary layer turnover times τ_δ. In total, 6 independent runs were conducted resulting in converged statistics also for large-scale events, such as coherent structures.

To investigate the dynamics of the flow separation and the interaction of large-scale structures with the separation line, time resolved planer PIV measurements were conducted in the APG section of the model. The illumination was also provided by the Photonics DM150-532 laser using $3 - 4.5\,\mathrm{kHz}$ repetition rate. The images were acquired using a Phantom v2640 camera with 2560×2560 pixel resolution.

In the following table 3.3, the measurement parameters over both models are listed. At model 1, wall-parallel (x^*z^*-plane) standard PIV and cross-stream (y^*z^*-plane) SPIV were measured for the ZPG and APG section. In the wall-parallel configuration, multiple planes with relative wall distances of $y^*/\delta_{99} = 0.07;\ 0.14;\ 0.28$ and 0.55 (ZPG only) were measured. To qualify the local seeding system, a seeding qualification experiment was performed in the x^*y^*-plane, which results will be discussed in section 3.5.1. The column “images” in table 3.3 refers to the number of statistically independent PIV images N per test point. The position x_0 refers to the origin of the boundary-layer model coordinate system with respect to the downstream end of the model.

PIV evaluation and vector field calculation was conducted with the commercial software Davis version 8.4 from LaVision. Details and principles of the PIV recording techniques, image evaluation methods for PIV and post-processing of PIV data can be found in the textbooks of Raffel et al. (2018) and Adrian and Westerweel (2011). For the data evaluation the background was subtracted and a linear min-max filter with a filter width of the interrogation window size was applied in a preprocessing step. Vector calculation was performed with a multi-pass algorithm. An overlap of 50 % was set between the interrogation windows. The final interrogation window sizes and additional data of the PIV evaluation is given in table 3.4. For the SPIV measurements, the final spatial resolution is limited by the light-sheet thickness, hence, interrogation windows with approximately the size of the light-sheet thickness were used. This limited the vector spacing to half the light-sheet thickness $0.5d_\mathrm{L}$ as 50 %

Table 3.4: Experimental and PIV evaluation parameters

Model	Case	dt (μs)	Final IW (pixel^2)	Vector spacing (mm)	FOV (m^2)
1	ZPG (x^*z^*)	575; 275; 150	24×24	2.8	1.58×0.47
1	ZPG (y^*z^*)	60; 26; 16	24×24	1.2	0.14×0.37
1	APG (x^*z^*)	230; 90; 55	16×16	0.9	0.23×0.56
1	APG (y^*z^*)	70; 25; 17	32×32	1.0	0.13×0.36
1	Seeding Test	80; 45; 22	16×16	0.6	0.17×0.12
2	ZPG (y^*z^*)	90; 38; 25	24×24	1.0	0.16×0.35
2	APG (y^*z^*)	×; 30; 32	32×32	1.9	0.28×0.29
2	APG (y^*z^*)	×; 62; 40	32×32	1.4	0.31×0.35
2	APG (y^*z^*)	×; 44; 34	32×32	1.4	0.31×0.36
2	APG (x^*y^*)	×; 125; 73	8×8	0.6	0.56×0.33
2	APG (x^*z^*)	×	24×24	2.1	0.36×0.36
2	ZPG (y^*z^*) (TR)	×	24×24 (75%)	1.1	0.07×0.16

interrogation window overlap was chosen (Raffel et al., 2018). After the vector calculation, a outlier detection and replacement was performed to reduce the amount of erroneous vectors.

Vector calculation was done for each camera, respectively each camera pair for the SPIV set-up, separately. The resulting vector fields were stitched together in Matlab afterwards interpolating the data linearly on a common grid to minimise errors due to overlap effects. This stitching of multiple fields results in the large FOV as denoted in table 3.4, which enables the investigation of large-scale structures in their full spatial extent.

3.4. Scale and resolution estimations

Turbulence is inherently chaotic and consists of structures of different spatial and temporal scales, as discussed in chapter 2. Within this section the spatial resolution issues concerning the turbulent scales will be addressed. The field of view that can be captured and the spatial resolution are determined by the used cameras, explicitly the sensor size, pixel size and magnification. This leads to conflicting restraints when measuring turbulent boundary-layer flows. On the one hand, the field of view should be as large as possible, on the other hand all scales should be resolved to get a full picture of the turbulence. Hence, the number of cameras as outlined before depends on the range of scales that should be resolved. With the length of the large-scale structure L and the length of the smallest resolved scales l_{res}, the ratio $\psi = L/l_{\mathrm{res}}$ is important to quantify the range of resolved scales. As the range of scales within the boundary layer is increasing with the Reynolds number (Klewicki, 2010; Pope, 2011), it is not possible to resolve all scales while capturing the large-scale structures at their full spatial extent with the currently available camera and laser equipment. In the following, the expected scales within the boundary layer are estimated, to address the possibilities and shortcomings of the above described experimental set-ups.

Based on equations 2.7 the characteristic wavelength $\lambda = 2\pi/k$ of the beginning of the dissipation region λ_{d} and the end of the large energy carrying scales λ_{f} can be estimated. The wavelength λ_{f} is only a function of the largest expected scale $L_{\max}$. In a boundary layer, those are large-scale structures with a streamwise length of multiple δ, as discussed in section 2.2. Therefore, the largest scales are considered to be of the order of $\mathcal{O}(\delta)$ for the

Table 3.5: Estimated spatial scales within the turbulent boundary layer.

Re_τ	λ_f (mm)	λ_d (mm)	η_k (μm)	ϵ ($\mathrm{m^2/s^3}$)	$\frac{\nu}{u_\tau} \cdot \frac{1}{\eta_\mathrm{k}}$	ψ
4200 (Model1)	10.39	0.69	23.07	11917	1.51	25.9 – 60.4
9300 (Model1)	10.61	0.37	12.42	142058	1.28	26.4 – 61.7
13400 (Model1)	10.18	0.26	8.78	567758	1.22	25.4 – 59.2
4100 (Model2)	8.82	0.62	20.5	19127	1.46	55.9 – 61.5
8400 (Model2)	8.03	0.32	10.61	265991	1.32	50.9 – 56.0
12000 (Model2)	7.67	0.23	7.57	1027124	1.22	53.5 – 48.6

estimations. For the dissipation region wave number λ_d, the Kolmogorov scales have to be estimated according to equation 2.9. The resulting wavelengths are given in table 3.5.

In order to resolve the length of the large-scale structure in most measurements, the streamwise extent of the field of view should be at least $2\,L$. The resolved length scale l_res is determined by the size of the interrogation window (IW) in PIV measurements. The interrogation-window size must be $l/2$ to resolve l_res. As structures with a length of $L \approx 6\,\delta_{99}$ are expected according to Hutchins and Marusic (2007b), the field of view in streamwise direction must be around $12\,\delta_{99}$. For the cross-flow planes, the field of view must be at least 3 characteristic structure spacings Λ to capture an adequate spatial domain. As the characteristic spacing is in the order of $0.7\delta_{99}$, as shown in chapter 4, the field of view should be larger than $2.1\,\delta_{99}$ in spanwise direction. Both restrictions are fulfilled for the measured data sets as seen in tables 3.1, 3.2 and 3.4.

The widest scale separation is present at the highest Reynolds number. In all data sets the Kolmogorov scales are in the order of $\mathcal{O}(\eta_\mathrm{k}) \approx 10^{-5} - 10^{-6}$ m. Those scales can not be resolved with the available equipment for the large FOV. Hence, the range of resolved scales is cut off at the double interrogation-window size. As interrogation-window overlap techniques are used, the spatial resolution is artificially increased and the smallest vortex which can be resolved has the length scale of the interrogation window, which is equal to the double vector spacing given in table 3.4. Based on this, the resolution ratio $\psi = L/l_\mathrm{res}$ is calculated for the ZPG flows and given in 3.5. The range given depends on the different measurements with individual interrogation-window sizes. Spencer and Hollis (2005) studied the effect of subgrid filtering in turbulent flows and give a ratio of $\psi = 10$ as absolute minimum for correct second order statistics, which is fulfilled in this study.

Comparing the resolved scales with the estimated length scales of the dissipation region and energy carrying region shows that for all Reynolds numbers the large, anisotropic, energy carrying structures are captured. The flow field in the vicinity of large-scale structures, such as vortices and shear layers, is also resolved sufficiently. In contrast to the large-scale components, smaller vortices are not resolved and thereby neglected in the analysis. As small scale turbulence is isotropic (Pope, 2011), this does not cause any problem for the description and understanding of large-scale, anisotropic structures in the boundary-layer flows.

The estimated scales discussed so far were calculated based on Pope (2011). According to Klewicki (2010), the friction velocity Reynolds number Re_τ is also a measure for the range of scales, as discussed in section 2.1.1. Hence, the viscous unit ν/u_τ is the smallest expected scale. In table 3.5, the ratio between the viscous unit and the estimated Kolmogorov length scale η_k is calculated for the experimental data sets. The viscous scale is approximately $1.2 - 1.5$ times larger than the estimated Kolmogorov length, but both are in the same order of magnitude. In summary, it can therefore be stated that at least for resolution estimations in terms of boundary layer measurements, the scale ratio based on the friction velocity is sufficient.

3.5. Preliminary Investigations

In line with the experiments and analysis, pre-investigations are required to test systems and analysis tools. As previously mentioned in section 3.1, seeding particles were inserted for the PIV measurements with a local seeding system, which was newly developed for turbulent boundary layer research (Reuther and Kähler, 2018). The built up and qualification of the system is described in subsection 3.5.1. Furthermore, the convergence of the acquired data sets must be ensured to achieve correct statistics and minimise errors. In subsection 3.5.2, a detailed convergence analysis is discussed. Lastly, the applied two-point correlation methods, based on which the coherent structure scaling will be investigated, are tested and qualified for different cases within the convergence analysis.

3.5.1. Qualification of the local seeding system

The choice and insertion of seeding particles is one of the key tasks for reliable PIV measurements (Raffel et al., 2018). Especially for boundary layer experiments in an atmospheric wind tunnel, achieving a homogeneous seeding concentration in the boundary layer and the free potential flow in the wind tunnel centre is challenging, because of lacking turbulence in the laminar core flow only negligible mixing takes place. This problem can be solved by inserting additional seeding particles directly in the turbulent boundary layer. Due to the turbulent mixing the seeding is quickly distributed in the turbulent boundary layer. Furthermore, the use of two different seeding systems allows a control of the seeding amount in the turbulent boundary layer, hence the inhomogeneity of seeding concentration can be reduced to a practical minimum. In figure 3.7 a schematic sketch of the local seeding system installed in the wind tunnel wall is shown. In the AWM the local seeding system is installed approximately 1.5 m after the beginning of the test section. It consists of a wooden box with an internal pipe system. Attached to the box's pipe system is a Laskin nozzle seeder. Through the pipe system, the seeded air is sprayed into the box through small holes to generate high pressure losses. This is necessary to reduce the 1.5 bar overpressure, which is needed to generate the particles in the seeder (Kähler et al., 2002). Spraying the seeded air into the box in a counter flow configuration, the box's back wall can be used as an impactor plate for very large seeding particles. The box itself has the same effect as a settling chamber in a wind tunnel. It calms the flow and increases the mixing of the seeded air. In addition, a screen is installed in the box's exit to the wind tunnel to prevent larger jets from disturbing the boundary-layer flow and avoid Helmholtz resonance.

The key issue adding seeded air to a turbulent boundary layer is not to disturb its natural development. In figure 3.8 the mean velocity profiles in streamwise direction $\overline{u}$ and the normalised turbulent fluctuation profiles $\overline{u'^2}/u_\tau^2$ at the centre of the ZPG of model 1 are shown. For comparison the measurement represented with the dashed line was done with global seeding only, the experiment shown with the × symbols was measured with local and global seeding. As visible in figure 3.8, there is no influence of the local seeding detectable at the measurement location for both tested Reynolds numbers.

Besides adding additional seeding into the turbulent boundary layer, the local system can be used to detect the turbulent/ non-turbulent interface (TNTI) in PIV experimentally (Reuther and Kähler, 2018). Therefore experiments must be done with local seeding only. The intensity difference between a seeded and a not seeded part of the acquired PIV image is used to binarise the image and to calculate a masking function M which is 0 for the laminar

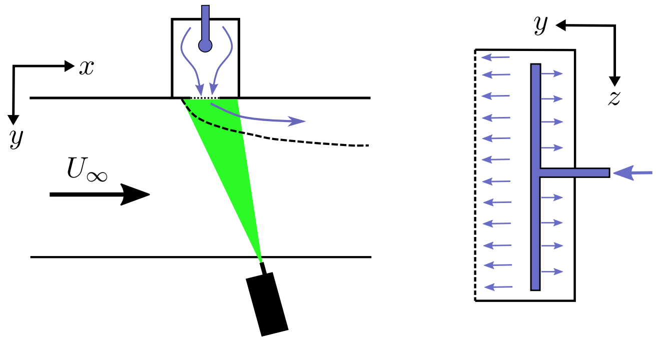

Figure 3.7: Left: Top view on the test section with the local seeding system. Right: Side view of the seeding system box with inner distribution tube.

and 1 for the turbulent part. Based on the mask, the intermittency factor γ which is defined as

$$\gamma(x^*, y^*, z^*) = \frac{1}{N} \sum_{n=1}^{N} M(x^*, y^*, z^*, n) \tag{3.3}$$

with total number of PIV images N can be calculated. The average intermittency factor can be taken as a quantitative measure for the correct capture of the TNTI, as shown by Reuther and Kähler (2018). In figure 3.9 the resulting intermittency factors γ for the ZPG of model 1 at different Reynolds numbers are plotted.

The intermittency factors from the experiments fit well on the comparison data from Klebanoff (1955). For the high Reynolds number $Re_\tau = 13400$ the intermittency close to the wall is overestimated. This is a result of the masking algorithm. For high flow velocities, the overall amount of seeding in the flow decreases. Hence, the masking process takes parts with very low seeding concentration as not seeded and therefore as laminar.

3.5.2. Convergence Analysis

Turbulent boundary-layer flows are inherently chaotic and must be described by means of statistical approaches, as discussed in section 2.1. To minimise the error of the calculated flow properties, especially the spatial scales of the investigated coherent structures, convergence of the flow variables must be ensured. Therefore, the error in the calculation of the fluctuation u' according to equation 2.17 must be minimised. For PIV the measurement error is dependant on the error from the estimation of the pixel displacements $\sigma_{\Delta x}$, which can only be influenced by the measurement set-up, sub-grid displacement estimation and vector calculation itself (Raffel et al., 2018). In contrast, the error from the calculation of the mean velocity and standard deviation can be minimised ensuring statistical convergence. Therefore, a convergence analysis of the mean flow field and higher statistical moments is performed in this section.

In figure 3.10 the convergence of the mean velocity $\overline{u}$ and higher order statistical moments are compared for the SPIV measurements at $Re_\tau = 12000$. The five investigated wall normal positions are chosen to be in the log layer ($y^*/\delta_{99} = 0.075$), the intermittent region ($y^*/\delta_{99} = 0.6$), the free stream ($y^*/\delta_{99} = 1.2$) and two more positions in between at $y^*/\delta_{99} = 0.15$ and $y^*/\delta_{99} = 0.3$, which roughly corresponds to the positions of the wall-parallel measurement locations.

Regarding the mean velocity, a relatively low number of approximately 100 independent vector fields is sufficient for convergence. The normalised mean velocity is increasing with wall distance as it is expected for a turbulent boundary layer. In terms of higher order statistics

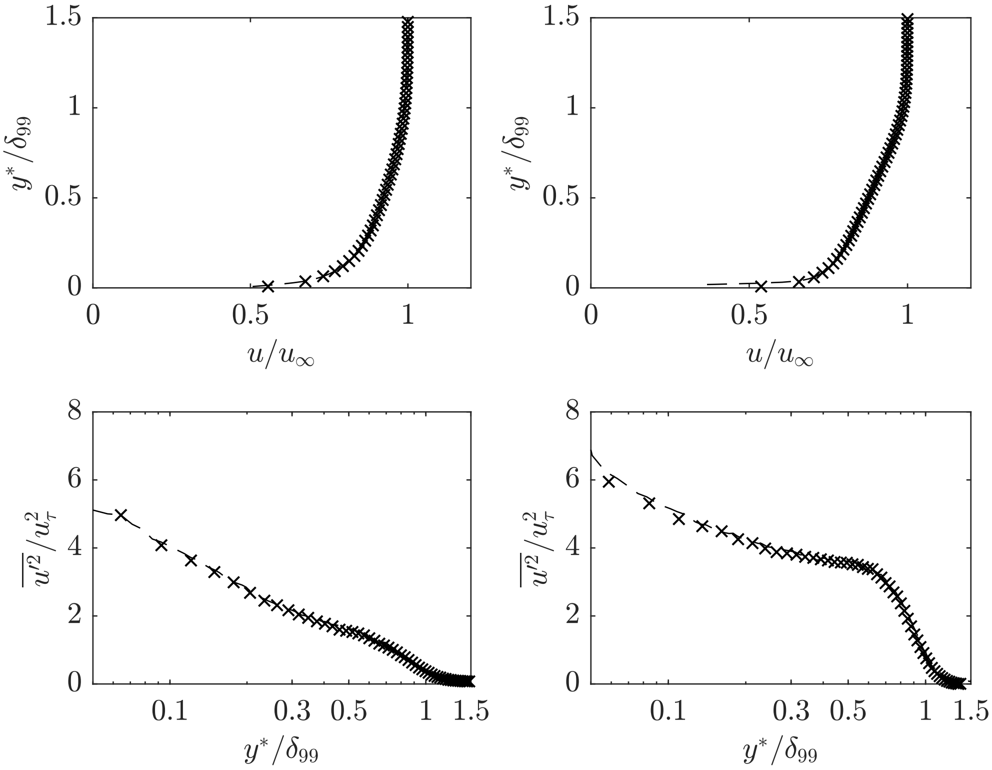

Figure 3.8: Comparison of the mean velocity profiles $\overline{u}$ and normalised turbulent fluctuation profiles $\overline{u'^2}/u_\tau^2$ for Reynolds numbers $Re_\tau = 4600$ (left) and $Re_\tau = 12500$ (right) measured over the boundary-layer model. Dashed line (— —) is the reference case with global seeding, × symbols correspond to measurements with local seeding and global seeding combined.

more images are required. Second order statistics are converged in all tested cases after 500 independent vector fields, third and fourth order statistics require at least 3000 independent vector fields, but the resulting value is still subject to high noise. There are no trends visible in convergence comparing the wall distances in the fully turbulent region. For the two outer wall distances $y^*/\delta_{99} = 0.6$ and 1.2 convergence is worse as there is less turbulence activity. For the wall distance $y^*/\delta_{99} = 1.2$ the third and fourth moment are not plotted because they are way out of bounds compared to the other results due to the small standard deviation σ in this plane.

Physically interpreted, the normalised second order statistical moment is the intensity of turbulence Tu. The intensity of turbulence is decreasing with increasing wall distance which implies that there is less turbulence activity further away from the wall. For the wall distance $y^*/\delta_{99} = 1.2$ the remaining intensity of turbulence is $Tu \approx 0.015$. The wind tunnel is not perfectly laminar in the core flow, but has a remaining turbulence level of $Tu \approx 0.2\,\%$, as discussed in section 3.1. In addition, seldom turbulent events reach up to wall distance of $y^*/\delta_{99} = 1.2$. Furthermore, the measurement uncertainty is higher in the SPIV measurement further away from the wall due to the experimental setup, because the stereo half-angle is decreasing with increasing wall distance. Hence, this number can be considered to be the maximum measurement uncertainty for the SPIV measurement plus remaining turbulence level.

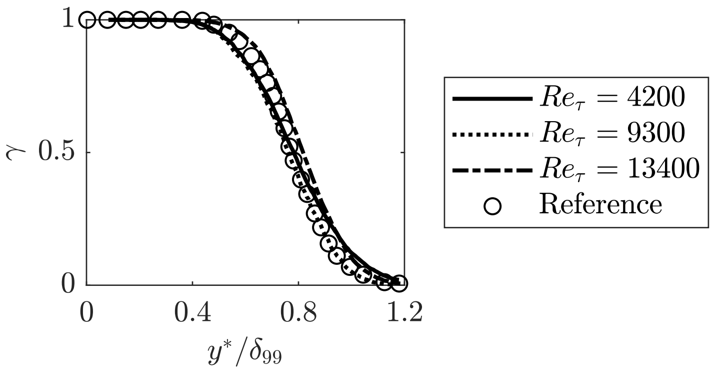

Figure 3.9: Intermittency factor γ calculated for different Reynolds numbers, $\circ$ symbols correspond to a reference case from Klebanoff (1955).

Statistical skewness of the fluctuation distribution, which is the third order statistical moment, is negative for all investigated data sets. Accordingly, the most probable fluctuation is positive. The statistical flatness is around 2.7 for the fully turbulent planes, which is below the kurtosis of a Gaussian distribution which is 3 but close to the measured flatness of 2.8 in fully turbulent flows (Fernholz and Finley, 1996). This implies that there is broadband turbulence as expected for a boundary layer. For the two outer planes, the kurtosis is increasing, which is a result of more seldom bulge events which reach that far away from the wall, resulting in more discrete negative fluctuations. Furthermore, the skewness is decreasing because the average detected fluctuation is small and positive (Reuther and Kähler, 2020). Due to the calculation of the turbulent fluctuation relative to the average, the laminar flow is interpreted based on the Reynolds decomposition as a positive fluctuation.

Besides the convergence of the flow variables, the convergence of the two-point correlation functions itself must be investigated, as the spatial correlation is the key tool used for the structural analysis in the results discussion. In figure 3.11 the correlation coefficient $R_{u'u'}$ in a wall-parallel plane at $Re_\tau = 9300$ is plotted. The four images are calculated using 200, 2000, 4000 and 10000 independent vector fields.

In all images the coarse shape of the positive and negative correlated area is apparent, but the image with only 200 correlated flow fields is not converged and subject to high noise. Between the other three fields no significant changes of the size or shape of the correlated areas occur. At the 10000 correlated flow fields, the correlation function is becoming more symmetric and smooth because statistical errors which are on large time scales, e.g. minor changes of the atmospheric inflow conditions or gusts at the inlet tower, are averaged out.

Within the result analysis in chapter 4, the data will be conditioned on different flow events. Of certain interest are structures associated with high or low-momentum fluid. Hence, it is necessary to condition the data sets on appropriate events. Within a high / low-momentum structure, the absolute value of the turbulent fluctuation $|u'|$ is large. Consequently, the fluctuation at the correlation point P is a possible criterion to identify high and low-momentum structures. To define a proper detection criterion, the local standard deviation σ_u is calculated for each correlation point and only structures with a fluctuation in the correlation point $u'_\mathrm{p} > k \cdot \sigma_u$ for high-momentum, respectively $u'_\mathrm{p} < -k \cdot \sigma_u$ for low-momentum structures, were correlated. The conditioning factor k is a chosen value to distinguish the momentum influence. Due to conditioning, the amount of data which can be used for the correlation and thereby the convergence of the correlation function is reduced significantly. Assuming a perfect Gaussian distribution of the velocity fluctuation u', only 2.28 % of the data can be used to correlate an appropriate structure for a data set conditioned on $u'_\mathrm{p} > 2\sigma$. The real

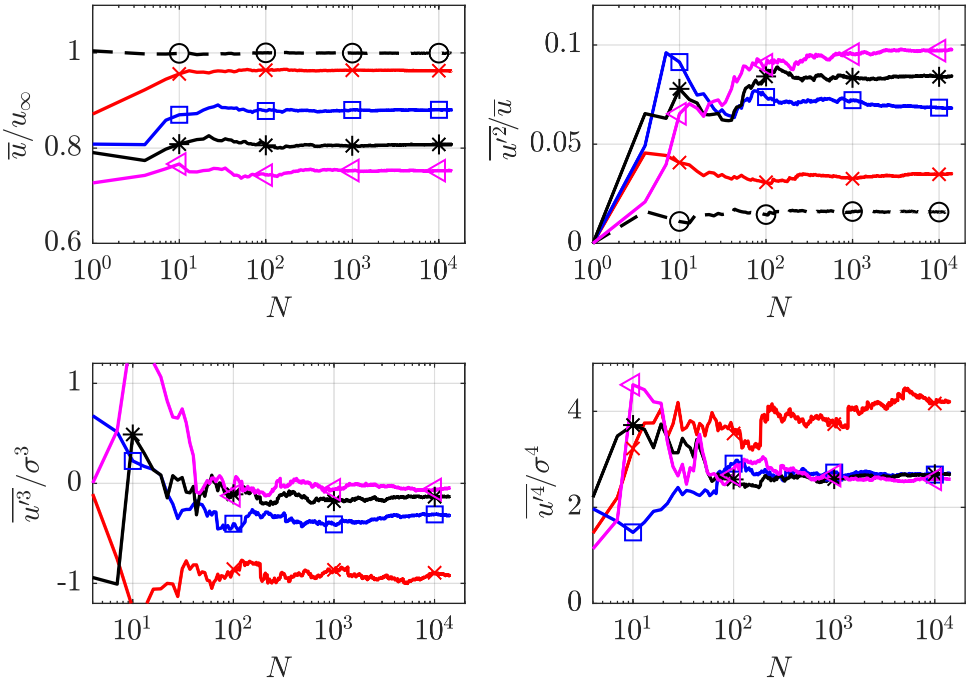

Figure 3.10: Evolution of the mean velocity $\overline{u}$, second, third and fourth order statistical moments of the flow velocity at $Re_\tau = 12000$ at five different wall normal positions. ○ : $y^*/\delta_{99} = 1.2$; × : $y^*/\delta_{99} = 0.6$; □ : $y^*/\delta_{99} = 0.3$; $*$: $y^*/\delta_{99} = 0.15$ and ◁ : $y^*/\delta_{99} = 0.075$

fluctuation distribution, as seen in figure 3.10, is slightly skewed. Hence, the correlations of low or high-momentum structures for one test case are not converging equally.

To overcome the problem of the significantly reduced data set when conditioning on flow events, multiple points are correlated within one image and stitched together afterwards in the central correlation point. This is possible if multiple fluid-dynamically identical points are present in one PIV image. In figure 3.12 the correlation functions from the ZPG cross-stream and ZPG wall-parallel measurements are plotted at a Reynolds number of $Re_\tau = 9300$ for one used correlation point (∘ symbols) and 120 correlation points (solid line). As visible in the plots, there is no difference between the single and the multi-point method for the correlation functions in spanwise and wall-normal directions. Only in streamwise direction, the multi-point correlation function decreases slightly faster, which results in a smaller structure length in comparison. In summery, the multi-point correlation analysis, utilising the point shifting as explained before, results in identical correlation fields and can therefore be used to increase the number of correlation points for the analysis.

In principle, it is possible by using the multi-point technique to achieve convergence of the two-point correlation function with few images and a large number of points. In figure 3.13 this case is evaluated. For the correlation of 200 independent vector fields different numbers of points are correlated. As visible, the 120 point case results in a converged correlation function. Another advantage of the multi-point technique is that slight laser-sheet misalignments and lens abbreviations are averaged out, which otherwise result in asymmetric correlation fields when only one point is correlated.

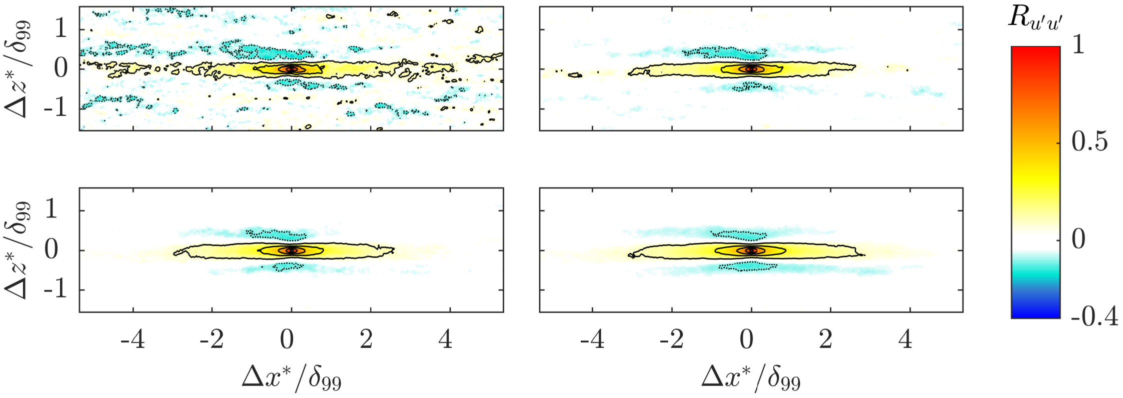

Figure 3.11: Correlation coefficient $R_{u'u'}$ in wall-parallel planes at $Re_\tau = 9300$ and a wall distance $y^*/\delta_{99} = 0.07$ using a different number of flow fields for the calculation. Top left: 200 fields, top right: 2000 fields, bottom left: 4000 fields, bottom right: 10000 fields.

As a rule of thumb, for the 1 point reference case at least $1000 - 2000$ statistically independent flow fields are necessary for convergence. This is in the same order of magnitude as the convergence of the second order statistical moment, which it is expected to be because according to equation 2.17, the correlation coefficient is the sum of the product of fluctuations normalised with the standard deviation. Using multiple points, this limit can be pushed to less flow fields, but still a minimum of approximately 500 statistically independent flow fields are recommended, because this is the lower limit of the convergence of the second order statistical moment.

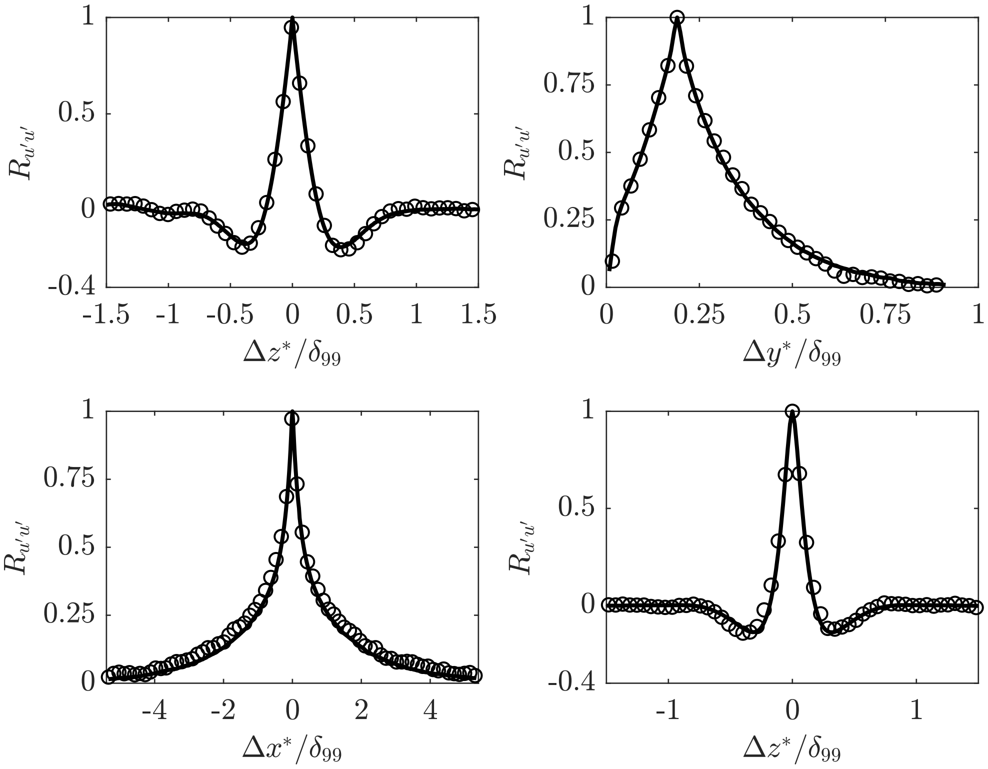

Figure 3.12: Comparison of the two-point correlation function for one used correlation point (○ symbols) and 120 correlation points (solid line) at $Re_\tau = 9300$. Top row: Correlation function in spanwise (left) and wall normal (right) direction from the ZPG Stereo measurement. Bottom row: streamwise and spanwise correlation function from the wall parallel measurements at $y^*/\delta_{99} = 0.07$.

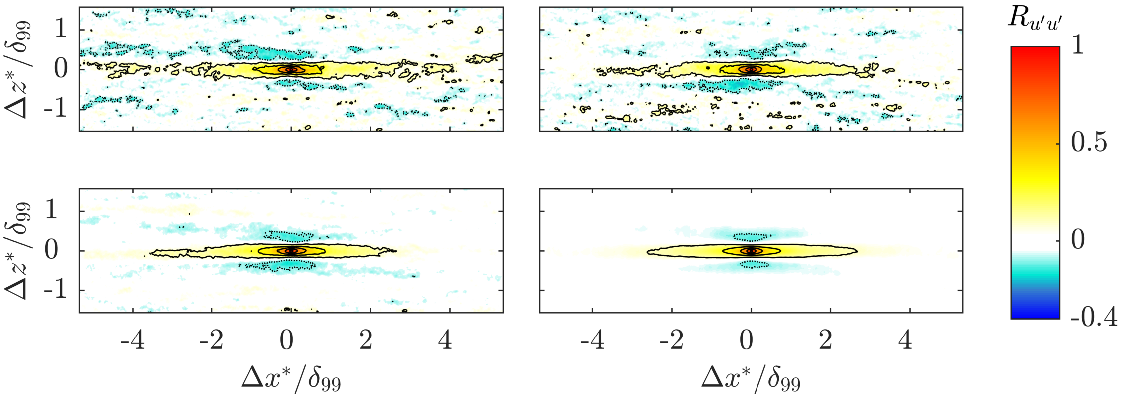

Figure 3.13: Correlation coefficient $R_{u'u'}$ in wall-parallel planes at $Re_\tau = 9300$ and a wall distance $y^*/\delta_{99} = 0.07$ using a different number of correlation points in 200 flow fields. Top left: 1 point, top right: 4 points, bottom left: 10 points, bottom right: 120 points.

4

Statistical analysis of large-scale structures in turbulent boundary layers

In this chapter the results of the measurements on both boundary-layer models are discussed, focusing on the statistical analysis of the scaling of large-scale structures in turbulent boundary-layer flows. The analysis of the scaling is the first approach to understand the dynamics within a boundary-layer flow, because the observed velocity pattern is a direct result of the action of turbulent structures.

The main investigation in this chapter is based on multi-point statistics, such as two-point correlations, and visual observations in instantaneous flow fields. As a first step in section 4.1 the results of the canonical ZPG boundary layer case are discussed, which are the common baseline cases for turbulent boundary-layer flow investigations. The focus is on the scaling behaviour of large-scale structures, the flow fields associated with the structures and the physical interpretation of the observations. Based on the statistics a conceptual model is derived, which explains the observed scaling behaviour of the large-scale structures.

As the scaling behaviour can not be completely explained and understood using a statistical approach, the effect of intermittency is investigated in detail in section 4.2. Furthermore, earlier studies have shown an increase in large-scale energy with increasing Reynolds number (Hutchins and Marusic, 2007b). Therefore, the influence of the streamwise momentum on the scaling of large-scale structures is investigated in section 4.3. This also gives further insight into the dynamics of large-scale structures, as high and low-momentum structures are most likely associated with Q2 and Q4 events in boundary-layer flows and therefore contribute significantly to the turbulence production, as outlined in chapter 2.

4.1. Scaling of large-scale structures under ZPG

In this section the results of the measurements in ZPG turbulent boundary-layer flows are discussed, focusing on the influence of wall distance y and friction velocity Reynolds number Re_τ on the large-scale structure topology. The most intuitive way to get an impression of the coherent structure topology is to examine instantaneous flow fields in wall-parallel planes. In figure 4.1 instantaneous fields of the streamwise velocity fluctuations u' normalised with the local mean velocity $\overline{u}$ in wall-parallel planes are shown. Clearly identifiable are regions of high (red) and low (blue) momentum fluid within the flow, aligned in a streaky pattern side by side.

The pattern is similar to the near-wall streaks topology but the length, width, spatial separation and intensity differ strongly (Smith and Metzler, 1983). Due to the remarkable large field of view of $11\,\delta_{99} \times 3\,\delta_{99}$ several large-scale structures, which extend multiple boundary

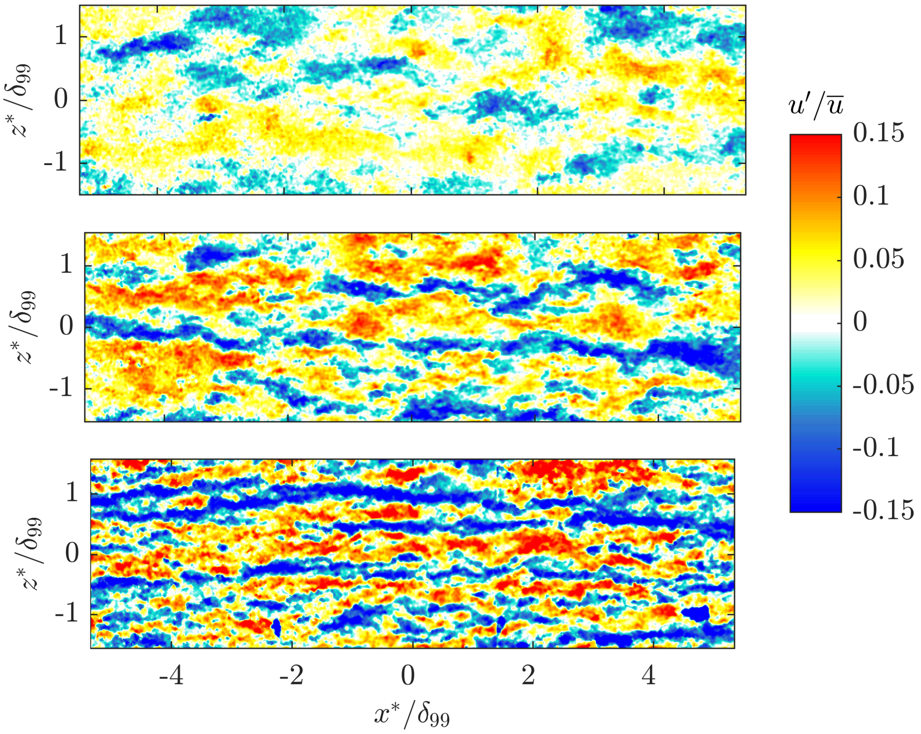

Figure 4.1: Instantaneous flow fields at $Re_\tau = 9300$ in three wall-parallel planes. Top: $y^*/\delta_{99} = 0.55$; middle: $y^*/\delta_{99} = 0.28$ and bottom: $y^*/\delta_{99} = 0.07$. The contours correspond to the normalised velocity fluctuations $u'/\overline{u}$.

layer thicknesses δ_{99} in streamwise length, can be found. The large-scale structures are not straight in streamwise direction, but meander in spanwise direction. This is observable following a region of high or low-momentum. The meandering was also observed by Hutchins and Marusic (2007b) using reconstructed flow fields from Taylor's hypothesis and quantified by Kevin et al. (2019) in wall-parallel PIV measurements. In the planes located at $y^*/\delta_{99} = 0.07$ and $y^*/\delta_{99} = 0.28$ a distinct streaky pattern can be identified in the bottom two plots of figure 4.1. However, in the plane located at $y^*/\delta_{99} = 0.55$ (4.1 (top)), which is located in the intermittent region of the turbulent boundary layer, no streaky turbulent structure can be found rather a distribution of laminar and turbulent regions. The distribution of the laminar and turbulent parts is more spot-wise and less elongated in streamwise direction compared to the inner planes. A similar spatial topology is found in the velocity fields at the other tested Reynolds numbers.

At this point of the discussion it should be noted that the Reynolds decomposition according to equation 2.1 is a chosen point of view which focuses on the high energetic, in the streamwise direction elongated structures in terms of turbulent kinetic energy $K = \overline{u'^2}$. Most parts of the turbulent boundary layer do not correspond to strong fluctuations, but are within the neutral region in between the structures, as can be exemplarily seen in the masked fields in appendix A.2. Large-scale passive structures in a turbulent fluctuation viewpoint based on the Reynolds decomposition with $u' \approx 0$ are not accounted for in the following analysis, as they do not contribute to the correlation function according to equation 2.17. However, the neutral region is also important in terms of the processes within the turbulent boundary-layer flow, because there the interaction and generation of coherent structures takes place, as will be discussed in chapter 6.

It is evident that assigning discrete values to the structure length, width, spacing and turbulent intensity inside a structure is not possible due to the strong variation of the geometrical and kinematic properties of the large-scale structures, but also because a cut through the structures at a certain distance from the wall gives only a partial view and not the total length L_1 of the structure, which is much longer according to Buchmann et al. (2016). To quantify the statistical properties of the structures and their sensitivity with the wall distance and Reynolds number, the vector fields are analysed by means of spatial two-point correlations as described in section 2.1.3.

In figure 4.2 the resulting length L_2 (top), width W_2 (middle) and height H_2 (bottom) calculated from the two-point correlations in cut planes at different Re_τ are shown. As previously shown in literature (Buchmann et al., 2016; Hutchins and Marusic, 2007b) and plotted in figure 4.2 (top), the length L_2 of the structures is relatively constant between $3.5\,\delta_{99} - 4.5\,\delta_{99}$ for the wall distances $y^*/\delta_{99} = 0.07 - 0.28$. There is a slight maximum at $y^*/\delta_{99} = 0.14$. For the outermost plane ($y^*/\delta_{99} = 0.55$), the length L_2 is shortened, as was also observed in the instantaneous flow fields previously.

The applied threshold of $Th = 0.15$ for the length scale calculation was selected at a higher value than values used previously in literature, where the spatial scales were reconstructed from Taylor's hypotheses and hot wire measurements (Hutchins and Marusic, 2007b), because the threshold must be well above the average turbulence intensity Tu and the PIV uncertainty to ensure that the resulting length is not biased by noise or the average fluctuations. The differences in absolute values for the length, when comparing this study with literature, are a result of the chosen threshold Th.

The correlated height H_2 of the large-scale structures is increasing with wall distance. The growth in height is not constant but contains a saddle point between $y^*/\delta_{99} = 0.3 - 0.5$ followed by a point of inflexion between $y^*/\delta_{99} = 0.45 - 0.6$, depending on the used threshold Th for the height calculation. This leads to three different regimes and slopes in the height distribution. A steep increase up to $y^*/\delta_{99} \approx 0.3$, relative constant height between $y^*/\delta_{99} \approx 0.3 - 0.45$ and a slower increase above. Similar observations were also made by Hutchins et al. (2005) in inclined cross-stream PIV measurements at $Re_\tau = 690 - 2800$. They explained the change in the growth rate on basis of the attached-eddy model with a change of the eddy regime from attached eddies to detached eddies. Since the same scaling behaviour is observed in a much higher Reynolds number range, about an order of magnitude higher than in the measurements of Hutchins et al. (2005), this implies that the underlying physical mechanism causing the slope change is not a low Reynolds number effect. The attached eddy hypothesis is a rather generic concept, which does not cover the real flow physics complexity and dynamics completely. Furthermore, the statistical reconstruction with attached eddies is not unique, but the statistical properties observed in a turbulent boundary-layer flow can also be reconstructed with other eddy or vorticity concepts, if the intensity and distribution is properly adjusted as this is a mere fitting process (Pamiès et al., 2009; Zhang et al., 2010). It is more likely, that the slope change is associated with intermittency effects as will be shown in section 4.2. In addition, these observations raise questions about at least one of the assumptions of the attached-eddy model. With increasing Reynolds number, the number of eddy hierarchies is expected to increase according to the model (Nickels et al., 2007). With regard to the observations, this means that a superposition of a different number of eddies of different hierarchies, which are used to model the flow, always have the same growth behaviour in wall-normal direction, which must be a function of the wall distance itself. This restrictive modelled growth behaviour seems to be an unphysical constraint when considering a chaotic flow regime, such as a turbulent boundary layer flow.

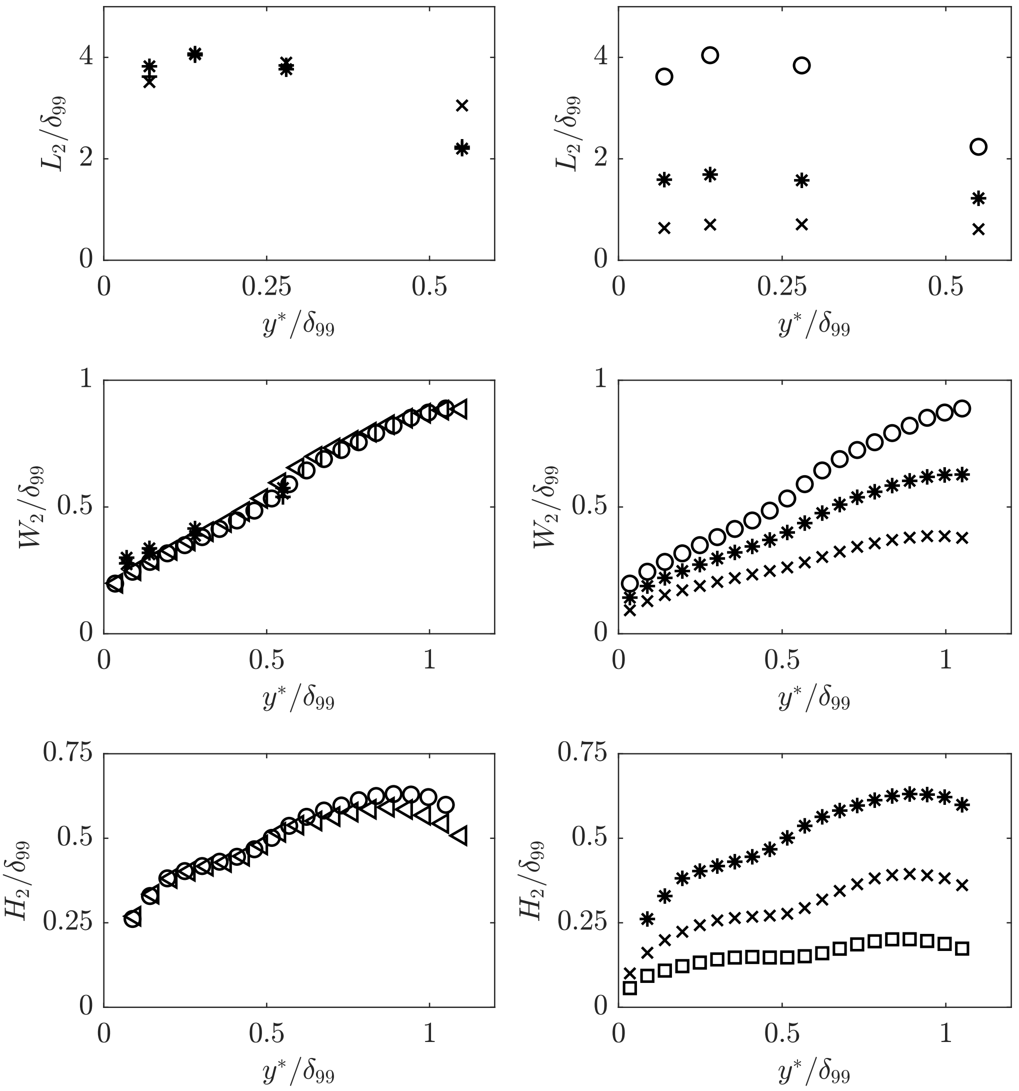

Figure 4.2: Comparison of different structure sizes L_2, W_2 and H_2 as a function of the wall distance y^*/δ_{99} under ZPG. Left column: Comparison of different Reynolds numbers with a constant threshold $Th = 0.15$ (length and width) and $Th = 0.3$ (height). Symbols correspond to $\triangleleft$: $Re_\tau = 12000$; $\circ$: $Re_\tau = 8400$ from SPIV measurements and $*$: $Re_\tau = 13400$; $+$: $Re_\tau = 9300$ and $\times$: $Re_\tau = 4200$ from wall-parallel measurements. Right column: Comparison of different thresholds Th at $Re_\tau = 8400$ for W_2 and H_2 and $Re_\tau = 9300$ for L_2: $\circ$: $Th = 0.15$; $*$: $Th = 0.3$; $\times$: $Th = 0.5$ and $\Box$: $Th = 0.7$.

In contrast to the length L_2 and the height H_2, the calculated width W_2 is increasing nearly linearly with the wall distance y^* up to the edge of the boundary layer. Only a weak point of inflexion is observed at $y^*/\delta_{99} \approx 0.45 - 0.55$. For all Reynolds numbers, the data collapses well, which implies that there is no influence of the Reynolds number on the structure width in the measured range. The observed scaling trend is also independent of the used threshold

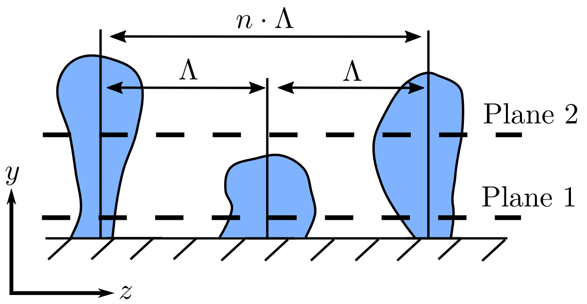

Figure 4.3: Sketch of turbulent large-scale structures (blue) with constant spacing Λ but different shapes and spanwise extensions analysed in two wall-parallel planes (–).

for the width calculation. Hence, the increase in structure width with the wall distance y^* is a physical characteristic of the structures within the flow.

The growth in spanwise direction can also be qualitatively explained by the attached eddy hypotheses of Townsend as often done in the past (Townsend, 1956; Perry et al., 1986). One of the key assumption of the attached eddy hypotheses is that the boundary layer is populated of eddies of various hierarchies. The size of the eddy is a function of the wall distance, hence the eddies can be considered as attached to the wall. A short discussion of the attached eddy concept is given in section 2.2 and in Nickels et al. (2007). One shortcoming of the attached eddy hypotheses as mentioned before is the strong dependency of the predicted results on chosen parameters, e.g. the eddy type and shape, the eddy growth rate with the wall distance and the eddy strength. A different more likely explanation for the observations follows from the impact of varying structure heights on the statistical multi-point analysis. This explanation therefore doesn't rely on chosen fitting parameters. Large-scale structures are constantly generated and appear to have distinct lifetimes within a turbulent boundary layer. Therefore, large-scale structures are observed at different stages of their lifetime in a sustaining cyclic process. The spatial extension therefore must depend on the development stage of the individual structures, and thereby the spatial scales L_2, W_2, H_2 are a function of the observation time. Only long lasting, large structures are present at larger wall distances. Considering large-scale structures with a nearly constant spanwise spacing Λ but various wall-normal heights, as exemplary shown in the sketch in figure 4.3, are statistically analysed in wall-parallel planes, the variation in structure height results in an increased average spacing Λ. This explanation is no inherent contradiction to a growth of an individual structure with the wall distance, because the height variation influence is independent of the structure shape and width. In fact, a combination of both effects, structure growth and statistical influence, is also a possible explanation for observed scaling results.

The effect of the height variation is apparent in the wall-parallel measurements, as plotted in figure 4.4. Discrete spacing, $n \cdot \Lambda_2$, $n \in \mathbb{N}$, are visible in both planes, which are highlighted exemplarily in the plots. For the plane at $y^*/\delta_{99} = 0.28$, the large-scale structures seem wider as well. Those observations support the previous explanation that the observed structure scaling is an effect of statistical height variation and structure growth.

To verify the explanation for the structure scaling in spanwise direction, the instantaneous spacing is quantified. Therefore, a probability density function (PDF) of the structure spacing is calculated based on binarised flow fields. As the spacing of large-scale structures, which arise from the wall is of particular interest, a value of $I = 1$ is assigned to the areas where $u' < -0.1 \cdot \sigma_u$. In the resulting binary field, multiple spanwise lines are analysed per vector field and the spacing between the centres of the regions with $I = 1$ is considered as structure spacing. The advantage of this calculation for the spacing is that it is unaffected by structure growth, because the distance between two structures is defined as the distance between the

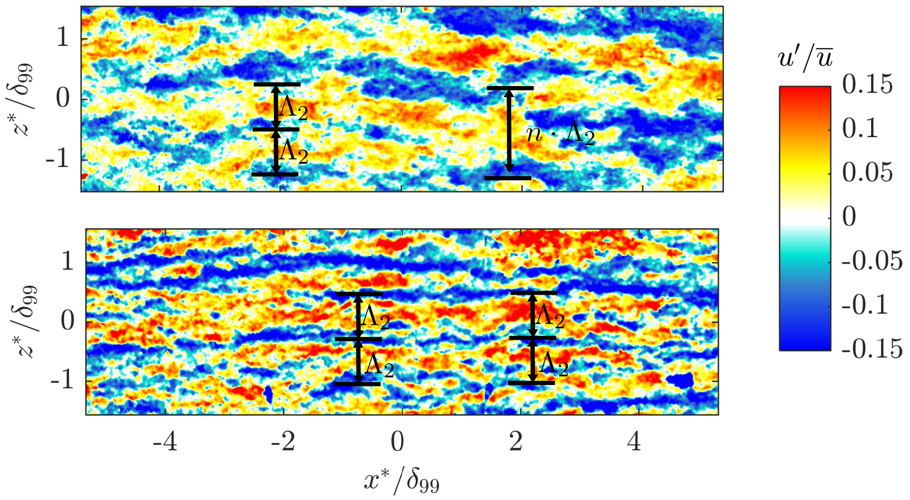

Figure 4.4: Instantaneous normalised velocity fluctuation $u'/\overline{u}$ at $Re_\tau = 9300$ in wall-parallel planes with zero pressure gradient. The structure spacing Λ_2 and multiple spacings $n \cdot \Lambda_2$ in spanwise direction are indicated. Top: Wall distance $y^*/\delta_{99} = 0.28$, bottom: y^*/δ_{99}.

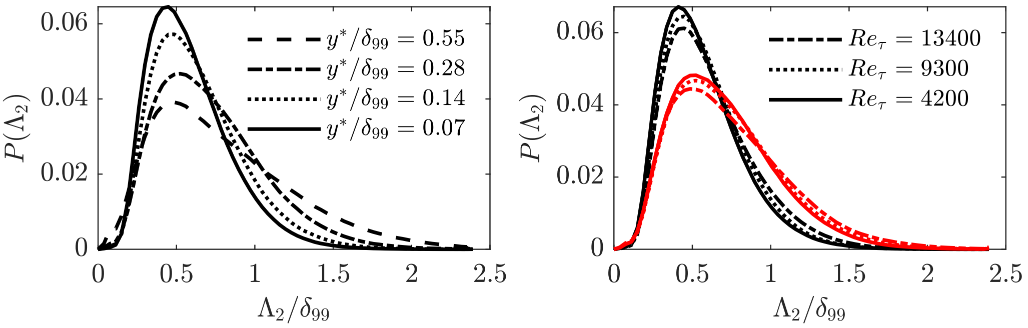

Figure 4.5: PDF of the large-scale structure spacing Λ_2. Left: Comparison of different wall distance for $Re_\tau = 9300$. Right: Comparison of different Reynolds numbers for wall distance $y^*/\delta_{99} = 0.07$ (black) and $y^*/\delta_{99} = 0.28$ (red).

	$y^*/\delta_{99} = 0.07$	$y^*/\delta_{99} = 0.14$	$y^*/\delta_{99} = 0.28$	$y^*/\delta_{99} = 0.55$
μ_{Λ_2}	0.59	0.64	0.73	0.81
σ_{Λ_2}	0.26	0.29	0.34	0.44
$\Lambda_{2,P_{\max}}$	0.45	0.48	0.52	0.49

Table 4.1: Mean μ_{Λ_2}, standard deviation σ_{Λ_2} and most probable distance $\Lambda_{2,P_{\max}}$ of the spacing Λ_2 distribution for different wall-normal locations.

centres of two regions. Hence, it is possible to prove if the height variation as described before has an effect on the calculated structure width or if it is pure growth as postulated by the attached-eddy model. To validate the calculation technique different thresholds for the binarisation were tested, which are shown in appendix A.3. In figure 4.5 the resulting PDF is shown.

The left plot of figure 4.5 shows the spacing distribution as a function of the wall distance. The most probable spacing is between $\Lambda_2 = 0.45 - 0.52$, which corresponds to the most probable distance between two low speed structures. Detailed numbers for the mean, standard deviation and most probable spacing are given in table 4.1. With increasing wall distance, the flatness of the distribution function is increasing. The probability of finding larger spacings Λ_2 rises. In contrast to the expectations based on the proposed height variation model, no distinct second peak at a spacing of $2 \cdot \mu(\Lambda_2)$ occurs. This is a result of the meandering and statistical distribution of the structures within the boundary layer. Also the peak in the PDF has a certain width which shows that there is no exact number for structures spacing without a gap, but a range of spacings that are most likely. In the right plot of figure 4.5, the effect of different Reynolds numbers on the structure spacing is apparent. A certain trend to a wider distribution for increasing Reynolds numbers is visible. A rise in the Reynolds number increases the number of scales present in the turbulent boundary layer (Klewicki, 2010). Hence, the turbulent boundary layer becomes more chaotic and a flatter distribution of the structure spacing is expected and observed. Interestingly, this effect is much smaller than the influence of the wall distance, which proves that large-scale structures are a basic and persistent feature of turbulent boundary-layer flows. It can also be stated based on the PDF of the spacings that the hight variation and gaps between structures arise in increased spatial scales based on two-point correlation analysis and the effect is not due to pure structure growth, but no distinct number for multiple spacings $n \cdot \Lambda$ can be defined. Therefore, the multiple spacing number n is not necessarily a natural number $n \notin \mathbb{N}$ as postulated in the introduction of the height variation theory in the beginning of this chapter.

So far, only the streamwise velocity component u was taken into account. In figure 4.6, the resulting spatial scales from the two-point correlation analysis of the wall-normal velocity component v and spanwise velocity component w are shown. The spatial coherence of the streamwise u velocity is the largest for all cases except the coherence of the spanwise velocity in the spanwise direction. All calculated scales increase with the distance to the wall. To understand the scaling trends, the corresponding events in the boundary layer must be analysed. In figure 4.7 a snapshot of the flow field under ZPG in the cross-stream yz-plane is shown. The colour contours represent the streamwise velocity fluctuation u', while the vectors show the spanwise and wall-normal velocity components. Around $z^*/\delta_{99} = 0$ a strong ejection event (Q2-event) with low-momentum fluid that reaches up to $y^*/\delta_{99} = 0.4$ is present. If a correlation of the streamwise velocity component is made for this event, the entire low-momentum region ($u' < 0$) will be positively correlated. Comparing to the vector field, the ejection itself ($v' > 0$) has a smaller spatial extent. Only inside the core of the low-momentum region is fluid moved away from the wall. At its sides a shear layer is formed, which also decelerates the surrounding flow and thereby results in larger low-momentum region. This smaller internal tube of ejecting fluid explains the smaller correlation of $R_{v'v'}$.

Strong spanwise movements are present at the side of the low-momentum structure, as fluid is sucked in or pushed away by the ejection. Those motions are limited to areas with small wall-normal extension. These observations are in accordance with the calculated scales of $R_{w'w'}$, where the correlated height is smaller by a factor up to 3 compared to the streamwise correlation $R_{u'u'}$. The redistribution of streamwise momentum leads to the characteristic mushroom shape correlation of $R_{u'u'}$, as seen in figure 4.14. In figure 4.7 (left) this process is qualitatively sketched as the grey canes. The redistribution of streamwise low-momentum in the spanwise direction is also affecting the correlated width scales W_2 calculated and plotted in figure 4.2. As discussed before, the increase in width is an effect of the statistical analysis but also of the momentum redistribution, as fluid with similar momentum correlates

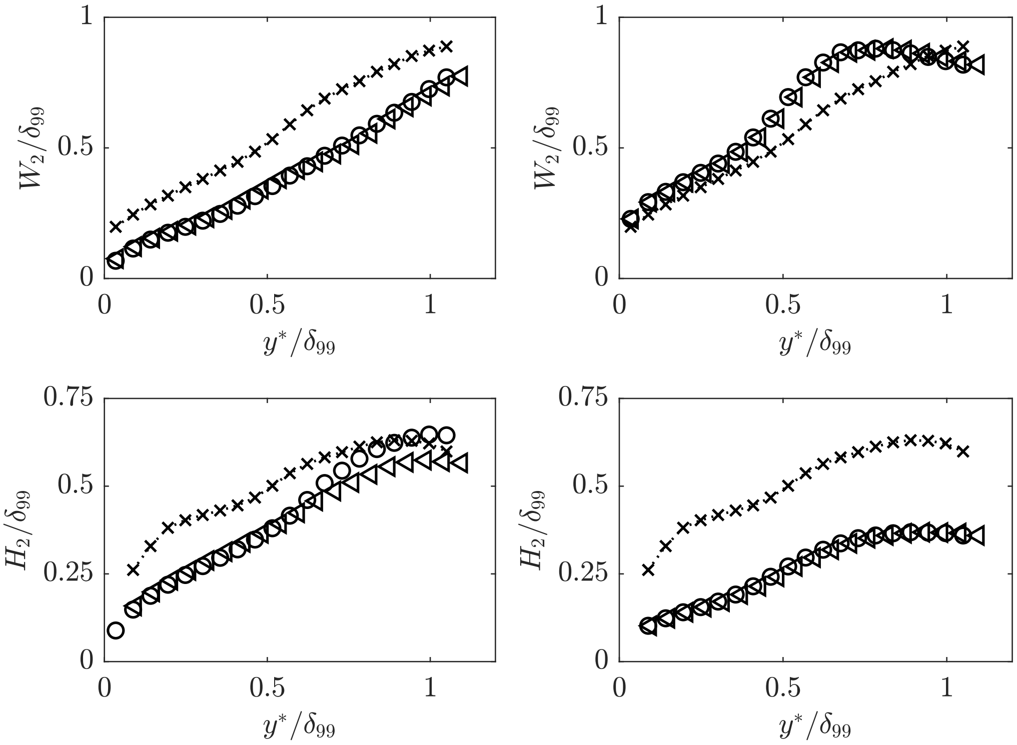

Figure 4.6: Spatial scales from two-point correlations of the wall-normal velocity component ($R_{v'v'}$, left) and spanwise velocity components ($R_{w'w'}$, right) at different Reynolds numbers as a function of the wall distance y^*/δ_{99}. Symbols correspond to different Reynolds numbers: $\triangleleft$: $Re_\tau = 12000$; $\circ$: $Re_\tau = 8400$. The dotted line with the × symbols corresponds to the scales from $R_{u'u'}$ at $Re_\tau = 8400$, which is plotted for comparison reasons.

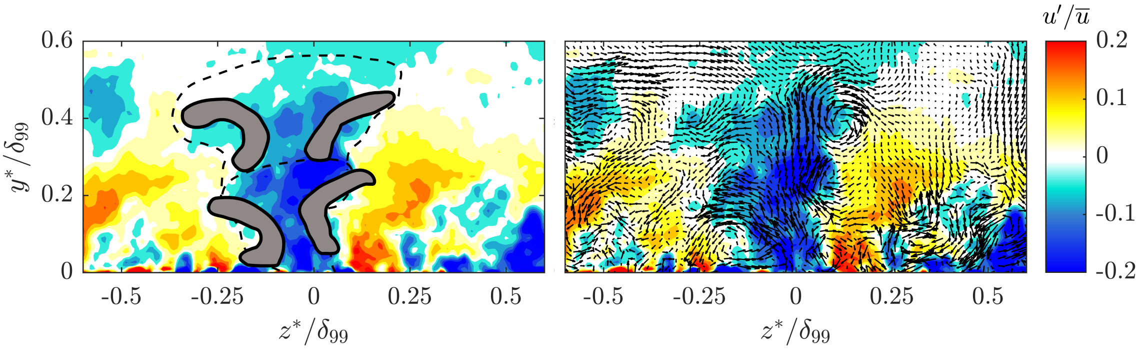

Figure 4.7: Instantaneous velocity fluctuation field $u'/\overline{u}$ in the cross-stream plane yz-plane. Vector arrows (right) represent the in plane velocity fluctuations v' and w'. Redistribution of momentum is highlighted with grey canes and the dashed envelope in the left plot.

positively in the two-point correlation analysis. This observation might be interpreted as a growth of the structure with increasing wall distance, which is not correct in a physical sense as the underlying mechanism is different.

Summarising these observations, it is evident that for the calculation of the spatial extension and scaling analysis of large-scale structures, only the streamwise component must be considered. The correlations of the wall-normal and spanwise velocity components don't represent the spatial scale of the large-scale structure itself, but of physical effects associated with the large-scale structures, as the ejection of low-momentum fluid or spanwise displacement of fluid. Hence, those components must necessarily be investigated for the understanding of the dynamics around a large-scale structure.

4.2. Influence of the intermittency on large-scale structures

At the edge of a turbulent boundary layer, the laminar potential flow from outside the boundary layer is converted into turbulent flow (Reuther and Kähler, 2020). The wall-normal position y^* of the boundary layer edge varies strongly due to this process. Accordingly, the instantaneous boundary layer thickness $\delta(x^*, y^*, z^*, t)$ is not only a function of the position (x^*, y^*, z^*), but also of the time t, as turbulence is an unsteady process (Schlichting and Gersten, 2006). Hence, it is possible to encounter turbulent flow or laminar potential flow at one point, depending on the time of observation. A quantitative measurement for the probability that the flow is turbulent at a distinct wall-normal position is the intermittency factor γ, which was introduced and calculated in section 3.5.1.

Using the characteristics of the flow type (laminar or turbulent), it is possible to mask out the potential flow and analyse only the turbulent part. Different approaches for the detection of turbulent/non-turbulent interfaces (TNTI) are feasible, as discussed in Chauhan et al. (2014) and Reuther and Kähler (2018). Reuther and Kähler (2018) compare different approaches and analyse the influence of intermittency on the calculated flow properties, e.g. velocity profiles or turbulence intensity. In this analysis, the focus is on the influence of intermittency on large-scale structures and their calculated spatial scales. Therefore, the potential flow is masked by the seeding concentration, as described and tested in section 3.5.1. The same system was used by Reuther and Kähler (2018) as a reference case for their masking algorithm.

Figure 4.8 shows an instantaneous flow field in a cross-stream y^*z^*-plane of a turbulent boundary-layer flow with masked laminar parts. Clearly recognisable is the different wall-normal height of the turbulent boundary layer edge, which is highlighted by the thick black line. Several turbulent areas appear to be independent features within the laminar masked part, e.g. at $z^*/\delta_{99} = 1.4$. This is not a masking problem, but a consequence of the three-dimensionality of the turbulent boundary layer. These parts are ends of structures that extend to the wall outside the light sheet. Comparable observations were made by Head and Bandyopadhyay (1981) in smoke visualizations of turbulent boundary layers. They explained these free turbulent parts with ends of tubular vortex loops. At about $z^*/\delta_{99} = 0.5$ there is a comparable characteristic cane shape structure within the plane. A different explanation for unconnected areas was given by Westerweel et al. (2009) analysing a turbulent jet with standard PIV. They argue that the lone-standing turbulent parts are detrainments of turbulence. The origin of the turbulence in the laminar parts cannot be fully deduced from a purely 2D data set and therefore information about the 3D topology of the boundary layer edge is necessary.

Based on the masked fields, it is possible to investigate the influence of laminar parts on the calculated turbulent structure scales. In figure 4.9, the correlation function at the cross-stream y^*z^*-plane is plotted. The red contour lines correspond to the masked case, the black contour lines to the reference case without masking. For the lower correlation point at $y^*/\delta_{99} = 0.53$ (left plot), the shape is similar, but the unmasked case has higher positive correlation to the regions further away from the wall. The point at $y^*/\delta_{99} = 0.53$ is at the beginning of the intermittent region, as can be seen in figure 3.9. If the correlation point is within a laminar flow, the correlation is positive to the outer part. As the intermittency factor

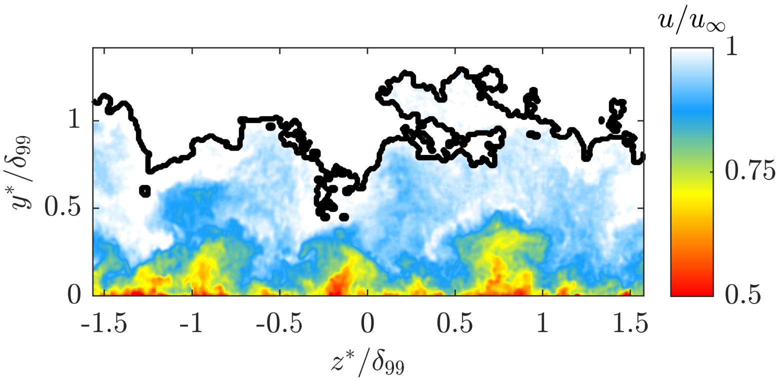

Figure 4.8: Instantaneous normalised velocity field u/u_∞ in a cross-stream plane. Laminar parts are masked out via the seeding approach. The resulting turbulent/non-turbulent interface (TNTI) is highlighted with the black line.

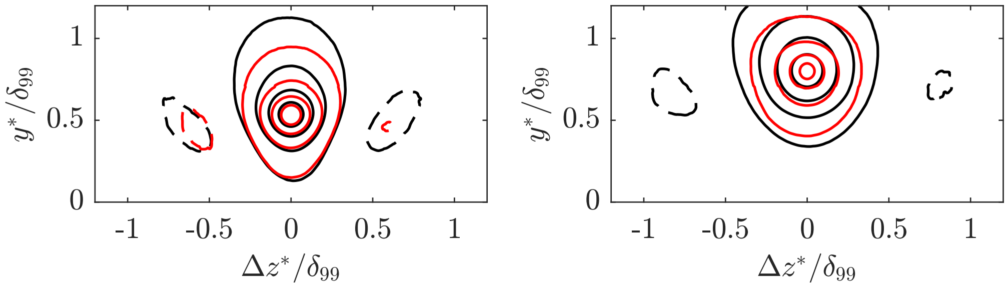

Figure 4.9: Two-point correlation functions for the masked cases (red) and unmasked reference case (black). Contour lines from $R_{u'u'} = -0.1$ to $R_{u'u'} = 0.7$ in steps of 0.2. Dashed line corresponds to negative correlated areas. Left plot: Correlation point at $y^*/\delta_{99} = 0.53$, right plot: $y^*/\delta_{99} = 0.8$

$\gamma \approx 0.9$ is close to 1 at this wall-normal location, the probability of being fully turbulent is higher than being within laminar flow. On average, this effect is therefore only visible for the lower correlation contour lines. For the higher correlation values, no significant difference between masked and unmasked cases are detectable. This changes when a correlation point is selected in the outer boundary layer, as shown in Figure 4.9 (right), where the correlation point is at $y^*/\delta_{99} = 0.8$. For this point, the intermittency factor is $\gamma \approx 0.4$. Accordingly, it is more likely that the correlation point is located within the laminar outer flow. The influence on the correlation is directly visible. For the masked case, no negatively correlated areas appear, as the absolute difference between the fluctuations is small if only turbulent parts are considered. Furthermore, the overall spatial coherence for the masked case is significantly reduced and the positively correlated region is distorted towards the wall. When the laminar external flow is masked, only the turbulent flow originating from the wall is correlated.

To quantitatively analyse the decrease in spatial coherence, the width W_2 and height H_2 are calculated from the two-point correlation function. Besides the shape of the correlation function, the calculated scales also change significantly. The resulting spatial scales are plotted in figure 4.10 at $Re_\tau = 8400$ for $R_{u'u'}$ top row, $R_{v'v'}$ middle row and $R_{w'w'}$ bottom row. The triangular symbols are the unmasked cases, the filled circles are the masked cases. For the width W_2 of $R_{u'u'}$ and $R_{v'v'}$ the increase is similar up to $y^*/\delta_{99} = 0.45$, above the width stays nearly constant for the masked cases. The further away from the wall the correlation point is, the stronger is the influence of the laminar parts in the intermittent region of the boundary layer. As the number of turbulent structures which reach to the point decreases with the wall distance, the laminar region increases in space, hence the spatial coherence of the laminar region is larger with increasing wall distance. The effect is basically the described height variation impact on the statistical analysis in section 4.1 and is a second evidence for the high variation explanation. As the width W_2 stays nearly constant for the masked case this implies that no growth of the structure occurs above this height. In the attached eddy hypothesis, Townsend (1956) refers to this as a detachment of the eddies from the wall. According to Townsend (1956), an eddy in turbulence can be considered as attached as long as it's size is increasing with the wall distance, which is not the case for the masked data above $y^*/\delta_{99} = 0.45$.

Comparable scaling effects are visible for the calculated height H_2 in figure 4.10 right. The change in scaling occurs at the point of inflexion in the height distribution. For the height, a much wider region of constant height between approximately $y^*/\delta_{99} \approx 0.25 - 0.8$ for $R_{u'u'}$ is present. As the correlated height of the structures has a constant value of $0.4\,\delta_{99}$, the spatial extent of the correlated structure is from $y^*/\delta_{99} = 0.05 - 0.45$ in wall-normal direction at the beginning of the region with constant height, assuming the structures are symmetric. Those observations are consistent with the width distribution, where the influence of the intermittency starts at $y^*/\delta_{99} = 0.45$. The earlier influence on the height is due to the observation in wall-normal direction, while the width is calculated in spanwise direction. To better understand the intermittency influence on width and height a schematic sketch is shown in figure 4.11. A structure can at maximum reach a height up to the turbulent/ non-turbulent interface (TNTI) in wall-normal direction, as shown in the sketch in figure 4.11. Down to the wall, the correlation is positive as long as the structure reaches down to the wall and was not lifted up. Combining these observations, the inner slope seen in the height distribution in figure 4.10 is caused by structure growth. Above $y^*/\delta_{99} \approx 0.3$ the structures are lifted up and stay constant in height. The decrease in height above $y^*/\delta_{99} = 0.8$ is a result of two effects. First, only very seldom turbulent ejections events reach above $y^*/\delta_{99} > 1$, as seen in figure 3.9. Second, the field of view only captures the boundary layer up to $y^*/\delta_{99} = 1.25$ which limits the observation of structures in wall-normal direction and results in shorter correlated structure heights the higher and closer the correlation point is to the end of the field of view.

Comparable scaling effects are visible for the calculated height H_2 in figure 4.10 right. The change in scaling occurs at the point of inflexion in the height distribution. For the height, a much wider region of constant height between approximately $y^*/\delta_{99} \approx 0.25 - 0.8$ for $R_{u'u'}$ is present. As the correlated height of the structures has a constant value of $0.4\,\delta_{99}$, the spatial extent of the correlated structure is from $y^*/\delta_{99} = 0.05 - 0.45$ in wall-normal direction at the beginning of the region with constant height, assuming the structures are symmetric. Those observations are consistent with the width distribution, where the influence of the intermittency starts at $y^*/\delta_{99} = 0.45$. The earlier influence on the height is due to the observation in wall-normal direction, while the width is calculated in spanwise direction. To better understand the intermittency influence on width and height a schematic sketch is shown in figure 4.11. A structure can at maximum reach a height up to the turbulent/ non-turbulent interface (TNTI) in wall-normal direction, as shown in the sketch in figure 4.11. Down to the wall, the correlation is positive as long as the structure reaches down to the wall and was not lifted up. Combining these observations, the inner slope seen in the height distribution in figure 4.10 is caused by structure growth. Above $y^*/\delta_{99} \approx 0.3$ the structures are lifted up and stay constant in height. The decrease in height above $y^*/\delta_{99} = 0.8$ is a result of two effects. First, only very seldom turbulent ejections events reach above $y^*/\delta_{99} > 1$, as seen in figure

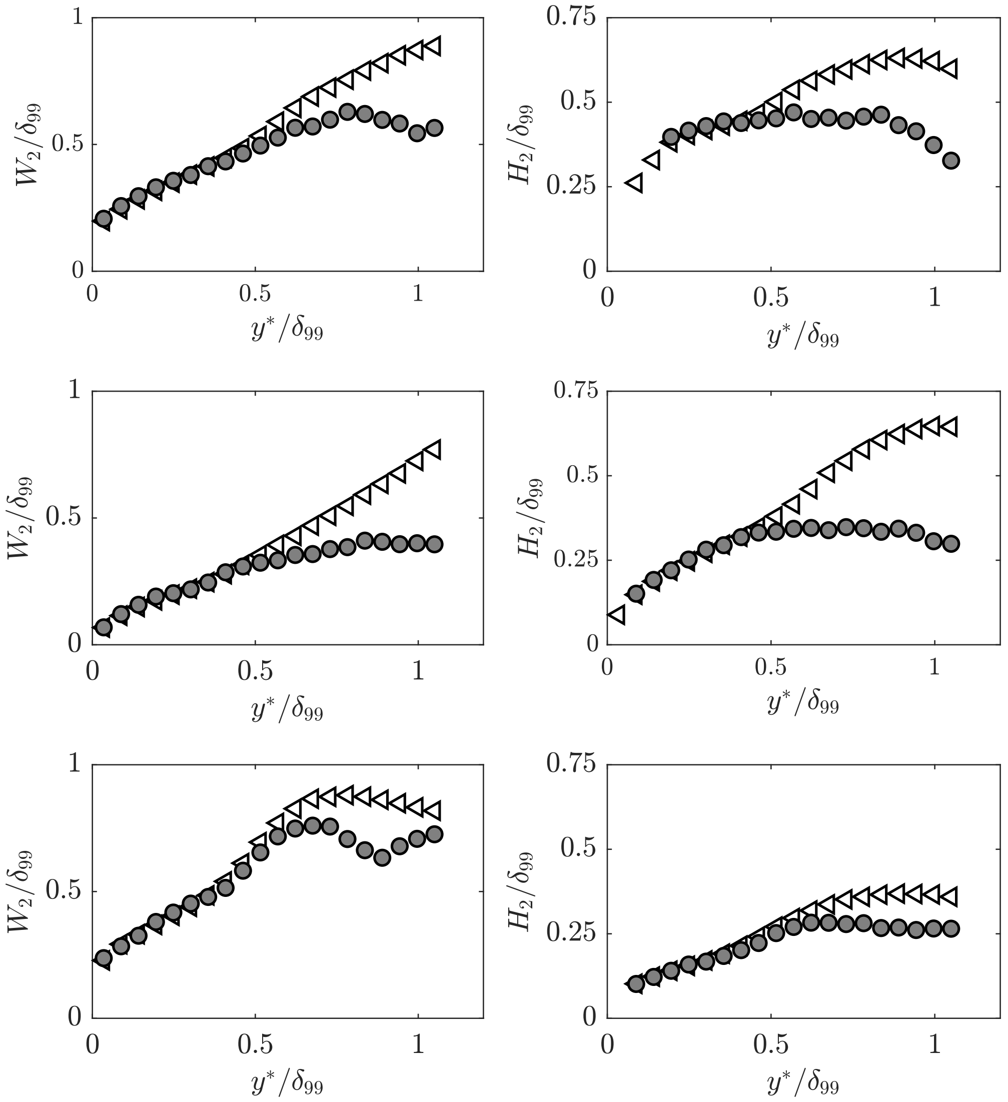

Figure 4.10: Structure width W_2 (left) and height H_2 (right) calculated from two-point correlations of $R_{u'u'}$ top row, $R_{v'v'}$ middle row and $R_{w'w'}$ bottom row at $Re_\tau = 8400$. The $\circ-$symbols correspond to flow fields were the laminar parts are masked out, $\triangleleft-$symbols are the reference case without masking.

3.9. Second, the field of view only captures the boundary layer up to $y^*/\delta_{99} = 1.25$ which limits the observation of structures in wall-normal direction and results in shorter correlated structure heights the higher and closer the correlation point is to the end of the field of view.

Different scaling is observed for the correlation of $R_{w'w'}$. As discussed previously in section 4.1 the positive correlation of w' is associated with the redistribution of fluid around a large-scale structure. The effect of intermittency is small compared to spatial coherence of the other velocity components. Free laminar potential flow has no spanwise velocity component in an ideal, canonical ZPG boundary-layer flow. This means that all spanwise movements are

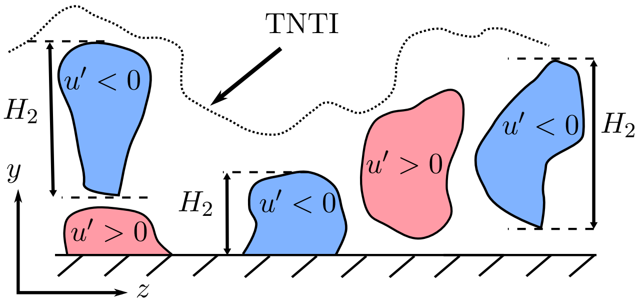

Figure 4.11: Sketch of the spatial distribution of large-scale structures originating from the wall in two different wall-normal planes. The dotted line corresponds to the turbulent non turbulent interface (TNTI).

associated with turbulent structures and occur in the turbulent part. Therefore, the effect of masking the laminar parts is small.

Combining all observations and following Townsend's ideas (Townsend, 1956) the point at which an average structure is not attached to the wall is close to the wall, at approximately $y^*/\delta_{99} = 0.25$, referring to the centre of the structure. Hutchins et al. (2005) also calculated the detachment point of large-scale structures from correlations in wall-normal direction and found detachment in a band between $y^*/\delta_{99} = 0.15 - 0.22$ for a threshold $Th = 0.3$, which is slightly closer to the wall than the change in the scaling observed in this data set. Taking the observations based on the masked fields into account, it is more likely that no different eddy regimes exist within the boundary layer, but that the described changes in scaling above the logarithmic-layer are a result of intermittency influence and the chosen statistical multi-point analysis tools.

4.3. Conditional analysis of large-scale structures

As argued in section 2.2, there must be a coherent structure within the boundary layer, which is neither isotropic nor random and responsible for the turbulence production term $\overline{u'v'} \neq 0$. In order to understand the dynamics of the underlying structures and their connection to the turbulent production term, characteristic events in the turbulent boundary-layer flow must be emphasised and analysed. Therefore, characteristic fluctuations and fluctuation combinations must be identified. A commonly applied tool to analyse the joint probability density distribution of fluctuations in turbulent boundary layers is the quadrant analysis (Wallace, 2016). In figure 4.12 the joint probability density distributions of $P(u', v')$ (left) and $P(u', w')$ (right) are plotted for a wall distance of $y^*/\delta_{99} = 0.07$. The contours correspond to the probability of the fluctuation combinations. While no preferential quadrant can be found for the $P(u', w')$ distribution, the quadrants Q2 and Q4 are over represented in the $P(u', v')$ distribution. A turbulent fluctuation in streamwise direction of $u' \ll 0$ (low-momentum structure) is most likely associated with a Q2 ejection event ($v' > 0$) and therefore with a turbulent low-momentum structure moving away from the wall, whereas a positive fluctuation in streamwise direction of $u' \gg 0$ is most likely associated with a Q4 sweep event ($v' < 0$) (high-momentum structure). The maximum of the $P(u', v')$ distribution is at $u'/u_\tau = 0.4$, at a positive value, which is similar to the observations made in the statistical convergence analysis in section 3.5.2. Physically interpreted, a positive fluctuation, hence a Q4 sweep event, is more probable than an ejection event, but ejection events result in stronger negative fluctuations in streamwise direction. It should be noted here to avoid confusion that Q2 and Q4 refer to a similar kind of events in the boundary layer, but not necessarily to similar structures. A Q2 event for example is associated with both, the lift up and burst

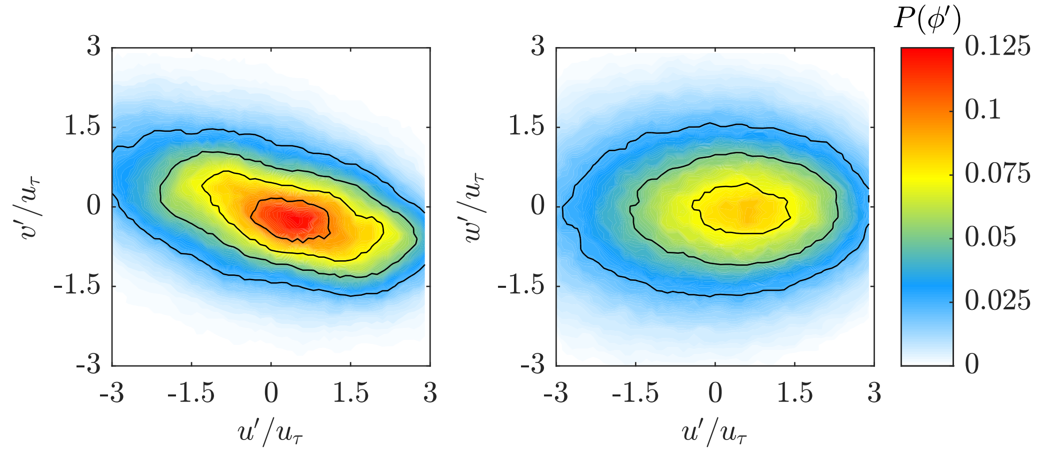

Figure 4.12: Joint probability density distributions of $P(u', v')$ (left) and $P(u', w')$ (right) at $Re_\tau = 12000$ and a wall distance of $y^*/\delta_{99} = 0.07$ under ZPG conditions.

of low-speed streaks, as described in section 2.2, and the events observed further away from the wall, which are a result of large-scale structures/ events in the boundary layer, will be discussed in this section.

To analyse the corresponding flow fields and to characterise the structures associated with the Q2 and Q4 events, the measured flow fields must be conditioned on appropriate events. The conditioning criterion used in this study is based on the standard deviation σ_u of the streamwise velocity distribution. For the analysis, only flow events where $u' > k \cdot \sigma_u$, $k = 0.5$ to 2.75 in steps of 0.25 in case of a Q4-event and $u' < -k \cdot \sigma_u$ in case of a Q2-event are correlated.

In figure 4.13, the resulting correlation planes of the correlation coefficient $R_{u'u'}$ for flow events conditioned on $u'_\mathrm{p} > 1.5\sigma_u$ and $u'_\mathrm{p} < -1.5\sigma_u$ are plotted. For both, high and low-momentum structures, the correlated regions are significantly elongated in streamwise direction compared to the average. The width of the correlated region is also increased. In the case of a high-momentum structure, the positive correlated region is skewed in the upstream direction, whereas for low-momentum structures the opposite is the case. Streamwise length and skewness of the positive correlated region of $L_2 \approx 6\,\delta_{99} - 8\,\delta_{99}$ are in accordance with observations of Buchmann et al. (2016) in a wall-normal xy-plane measurement of a compressible turbulent boundary-layer flow at $Re_\tau = 5100 - 9500$.

In order to understand the skewed shape of the positive correlated regions, the origin of the structure has to be taken into account. This becomes clearer when the conditioned two-point correlations in the cross-stream plane are examined. In figure 4.14, the correlation of the whole data set (left column), the correlation conditioned on $u'_\mathrm{P} > 1.5\sigma_u$ (centre column) and the correlation conditioned on $u'_\mathrm{P} < 1.5\sigma_u$ (right column) is shown. While the negative conditioned fields have a more mushroom-like shape, which extends down to the wall for both plotted wall distances, the positive conditioned correlation fields have a larger extent in wall-normal direction and a more straight shape. The low-momentum structures with $u'_\mathrm{P} < 1.5\sigma_u$ have their origin most likely near the wall and move outwards. For the high-momentum structures, it must be distinguished between the two wall distances. For the inner wall distance of $y^*/\delta_{99} = 0.13$, considering the height variation explanation given in section 4.1, an observed high-momentum structure is a result of structure gaps between low-momentum structures which correlates positively. The structures with $u'_\mathrm{P} > 1.5\sigma_u$, which have their origin in the outer boundary layer, are most likely inward moving fluid which belongs to larger eddies of turbulence with scales in the order of $\mathcal{O}(\delta)$.

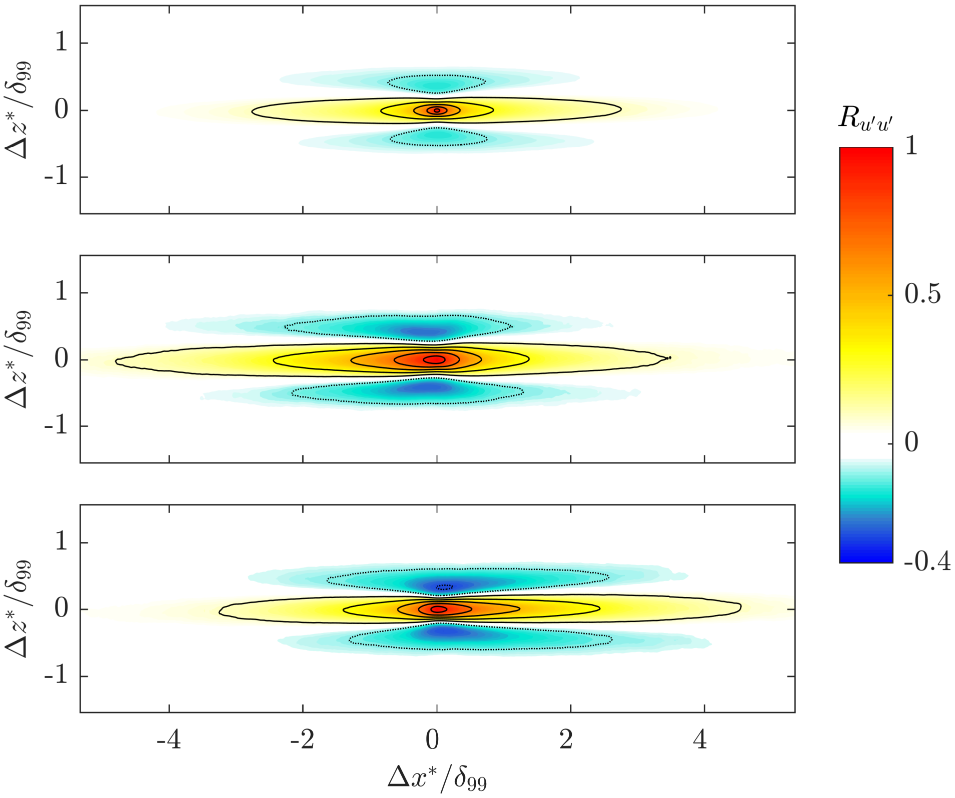

Figure 4.13: Two-point correlation in a wall-parallel plane with wall distance $y^*/\delta_{99} = 0.14$ and Reynolds number $Re_\tau = 9300$. The upper graph shows the correlation for all data. The middle graph the correlation $R_{u'u'}$ for fields conditioned on $u'_\mathrm{P} > 1.5\sigma_u$ the lower graph conditioned on $u'_\mathrm{P} < 1.5\sigma_u$.

In the bottom row of figure 4.14, the effect of the intermittency on high and low-momentum structures is qualitatively compared. Due to the stronger effect of the intermittency in the outer boundary layer, only the correlation point at $y^*/\delta_{99} = 0.55$ is shown. As expected, based on the discussion in section 4.2, the correlation of a low-momentum structure originating from the wall is unaffected by the masking of the laminar outer flow, whereas the spatial coherence of a high-momentum structure is significantly reduced.

The skewness observed in figure 4.13 of the two-point correlation field is a result of the position of the correlation point close to the wall. As seen in the quadrant analysis, the high and low-momentum structures are associated with strong wall-normal movements, which are inherently bound by the wall at their beginning or end respectively. Considering the correlation point is within a low-momentum structure, the structure most likely moves away from the wall. The correlation point can either be at the start of the structure, which leads to a very small spatial correlation, or the tail of the structure, which results in skewness of the two-point correlation field in downstream direction. For a high-momentum structure, the explanation is vice versa because an inward motion is bound at the wall. The correlation point is most likely at the downstream end of the structure and the positive correlation is skewed upstream.

To quantify the resulting structure scales, the length, width and height are calculated based on the two-point correlations and plotted in figure 4.15. The structure length L_2 is increased for high and low-momentum structures compared to the overall calculated length.

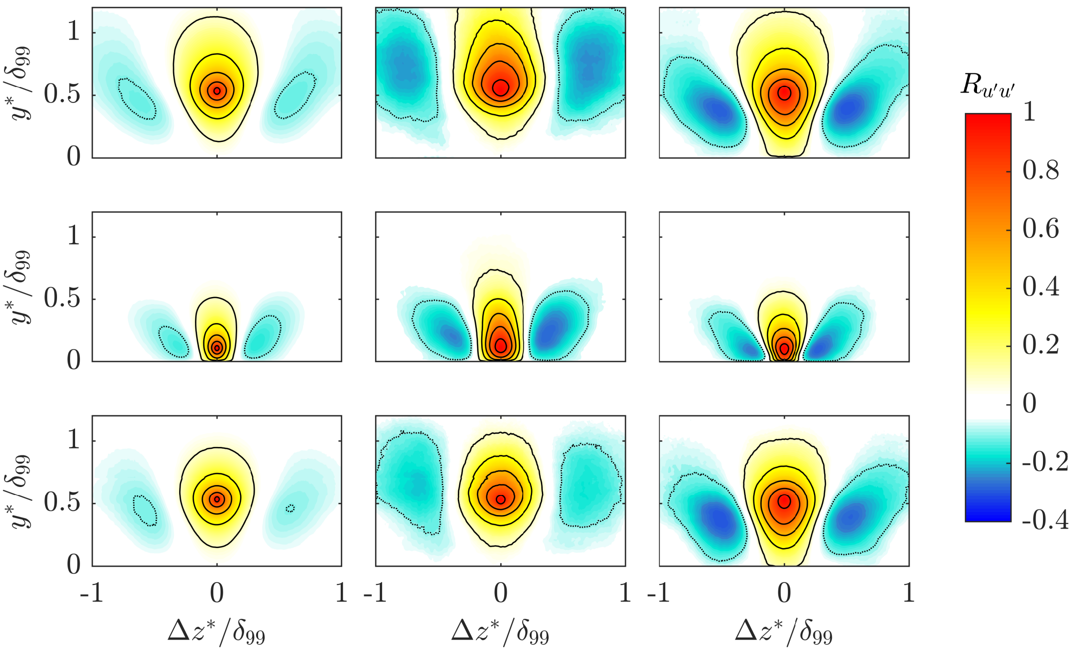

Figure 4.14: Two-point correlation of all data (left column), conditioned data on Q4 sweep events (middle column) and conditioned on Q2 ejection events (right column). Top row: Correlation point at $y^*/\delta_{99} = 0.55$. Middle row: Correlation point at $y^*/\delta_{99} = 0.18$. The bottom line shows intermittency masked fields for wall distance $y^*/\delta_{99} = 0.55$. Solid lines represent positive correlated areas with $R_{uu} = 0.1,\ 0.3,\ 0.5,\ 0.7,\ 0.9$, dotted lines negative correlation with $R_{uu} = -0.1,\ -0.3$.

In section 4.1 a maximum of the length was observed at $y^*/\delta_{99} = 0.14$, which is shifted further away from the wall to $y^*/\delta_{99} = 0.28$ for the conditioned structures. Comparing high to low-momentum structures, the high-momentum structures are slightly longer on average. The conditional analysis has also an impact on the calculated structure width. The width is slightly higher for high-momentum structures up to $y^*/\delta_{99} = 0.55$. Above, the width of high-momentum structures is decreasing rapidly. This is an effect of the increasing intermittency, where high-momentum is associated with potential flow and not turbulent structures any more (Reuther and Kähler, 2018). The scaling of low-momentum structures is similar to the trend shown in figure 4.2 and can thereby be interpreted as the structure size. The height of the conditioned structures is increased compared to the average calculated height H_2. In contrast to the complete data set, the conditioned cases have a strong velocity component in the wall-normal direction. This leads to redistribution of fluid with similar momentum in wall-normal direction which increases the spatial coherence in wall-normal direction as fluid with similar momentum correlated positive and therefore results in an increased correlated height. For the height of high-momentum structures, two maxima are detected which suggests multiple structural regimes.

As large-scale structures carry a significant proportion of the turbulent kinetic energy in the boundary-layer flow (Hutchins and Marusic, 2007b), the influence of the turbulent kinetic energy $\langle u'^2 \rangle / u_\tau^2$ on the large-scale structure scaling is of particular interest. In figure 4.16, the correlated structure length L_2 and width W_2 as a function of the normalised turbulent kinetic energy $\langle u'^2 \rangle / u_\tau^2$ for three different Reynolds numbers are plotted. As expected, the length increases with the turbulent kinetic energy. This points out that large-scale elongated

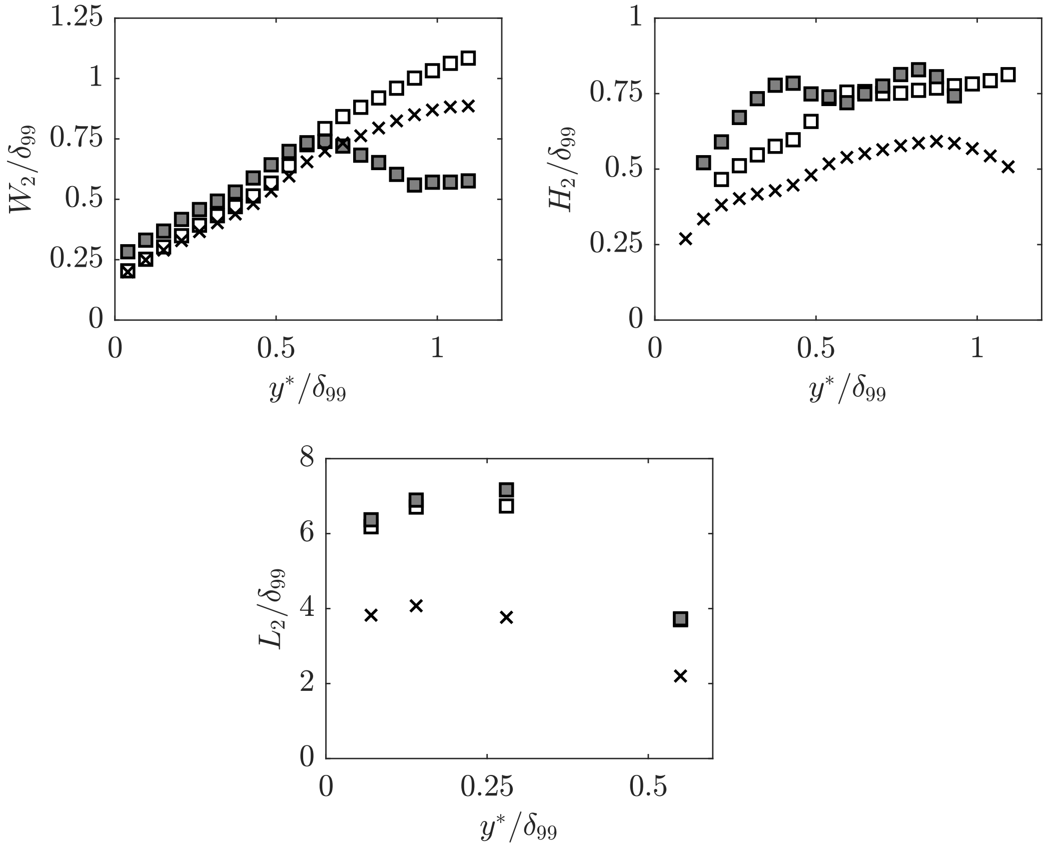

Figure 4.15: Spatial scales from two-point correlations $R_{u'u'}$ at $Re_\tau = 12000$ (W_2 and H_2) and $Re_\tau = 13400$ (L_2). The × symbols are the reference case with all data correlated, filled symbols correspond to high-momentum structures with $u'_\mathrm{P} > 1.5\sigma_u$. Empty square symbols to low-momentum structures with $u'_\mathrm{P} < 1.5\sigma_u$.

structures in streamwise direction are associated with regions of high turbulent kinetic energy within the boundary layer, as shown previously in hot-wire measurements by Hutchins and Marusic (2007a). They found in pre-multiplied energy spectra that the characteristic wavelength λ_x of structures connected to the outer peak in the energy spectra around $y^*/\delta_{99} = 0.06$ is approximately $\lambda_x = 6\,\delta_{99}$. This is in the same order as the calculated length scales from the conditioned two-point correlation analysis of the PIV data sets and thereby confirms the measurements of Hutchins and Marusic (2007a) using a different measurement technology, which is not relying on Taylor's hypotheses to reconstruct spatial scales.

Many studies in literature (Hutchins and Marusic, 2007a; Marusic et al., 2010; Smits et al., 2011) state that large-scale structures in the logarithmic-layer are the explanation for the second peak or plateau in the turbulent kinetic energy spectra. The observation of an increase in structure length with increase in turbulent kinetic energy proves this connection as well. The innermost plane at $y^*/\delta_{99} = 0.07$ is roughly at the location of the second peak and the connection between structure length and energy was made using conditional flow analysis.

Furthermore, an influence of the Reynolds number is detectable in the conditioned data. The higher the Reynolds number, the longer are the structures. This is in line with observations and results of previous studies, where increased turbulent kinetic energy near the outer peak in the boundary with increasing Reynolds number (Fernholz and Finley, 1996) and an increase in large-scale activity with increasing Reynolds number (Hutchins and Maru-

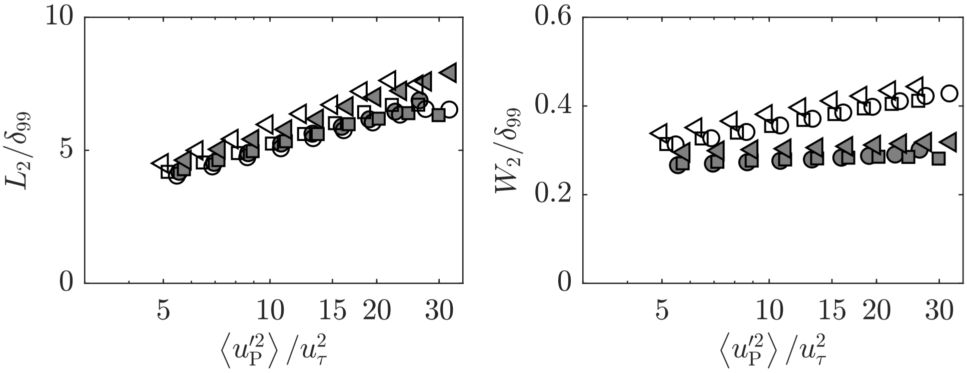

Figure 4.16: Large-scale structure length L_2 (left) and width W_2 (right) for different turbulent kinetic energies in the correlation point P measured at a wall distance $y^*/\delta_{99} = 0.14$. Symbols correspond to different Reynolds numbers: $\bigtriangledown$, $Re_\tau = 4200$; $\square$, $Re_\tau = 9300$; $\circ$, $Re_\tau = 13400$. Empty symbols correspond to low-momentum structures, filled symbols to high-momentum structures.

sic, 2007a; Mathis et al., 2009) was detected. In addition, a slight difference in turbulent kinetic energy between high and low-momentum structures can be observed. On average, low-momentum structures carry more turbulent kinetic energy than high-momentum structures of comparable length. This result corresponds to the calculated statistical skewness as shown in the figures 3.10 and 4.12. Besides the impact of the turbulent kinetic energy on the structure length, the width is analysed and the resulting width W_2 is shown in figure 4.16 (right). Interestingly, the width for low-momentum structures is nearly constant, independent of the turbulent kinetic energy, while the width of the high-momentum structure increases with the transported turbulent kinetic energy.

The increase of the spatial length with the turbulent kinetic energy decreases in rate with increasing turbulent kinetic energy. Assuming a limited growth, it is possible to extrapolate the maximum length which can be expected within the boundary-layer flow as a function of the turbulent kinetic energy. The structures length and width accordingly, are defined as

$$L_2 = L_{2,\mathrm{max}} - c_1 \cdot e^{-c_2 \cdot \langle u'^2 \rangle / u^2_\tau}, \tag{4.1}$$

with the limit $L_{2,\mathrm{max}}$ in case of the length and the fitting coefficients c_i. The maximum expected structure length based on this extrapolation is $L_{2,\mathrm{max}} \approx 8.5\,\delta_{99}$. This is consistent with the maximum structure length as shown in figure 4.16 and with the results of Dennis and Nickels (2011), who reconstructed structures up to $9\,\delta_{99}$ in their experiments using the Taylor hypothesis. The limitation of the structure length within a turbulent boundary-layer flow is in contrast to observations in investigations of boundary layers of internal flows, such as pipe and channel flows, where structures up to 20 characteristic length scales (e.g. pipe radii) have been observed (Kim and Adrian, 1999).

4.4. Summary of the statistical analysis

The work and discussion within this chapter focused on the statistical analysis of large-scale structures to gain a better understanding of their average occurrence, size and persistence. The well-known streaky structural patterns were identified at technically relevant Reynolds numbers and the scaling behaviour described in the literature could be confirmed. New scaling explanations, such as height bias in statistical interpretation, were derived. By combining large spatial data sets, conditional analysis and statistical methods, the influence of intermittency and streamwise momentum on the calculated structure scales and the derived conclusions were investigated. This analysis forms the basis for the following work in this dissertation, which focuses on the origin of large-scale structures and their persistence under the influence of an adverse pressure gradient. Fundamental understanding is a necessity, as an initial knowledge of the existing large-scale structures in a turbulent boundary-layer flow are crucial to derive new concepts and improve existing models.

5

Towards an improved spatial representation of a boundary layer from the attached-eddy model

In the previous chapter 4, large-scale structures were analysed and discussed on the basis of statistical approaches. This allows for the examination of average trends and scaling. To achieve a more complete understanding, conceptual models have to be formulated, evaluated and improved. The analysis and figures presented in the following are taken and adapted from Eich et al. (2020) with permission from the American Physical Society. The study was performed in cooperation with the University of Melbourne, Prof. Marusic, and University of New South Wales, Dr. de Silva, who also generated and provided the synthetic flow fields.

While single-point statistics can be well represented by a large number of different analytical models or eddy distributions (Pamiès et al., 2009; Zhang et al., 2010; Marusic and Monty, 2019), larger differences are observed in instantaneous spatial fields and multi-point statistics, likely due to the existence of other key structures in the flow and/or the overly simplified representative structures used. Recent works on the AEM have shown that some pertinent instantaneous spatial features of turbulent boundary layers can be reproduced by the representative structures employed in the AEM, e.g. uniform momentum zones or coherence of the spanwise velocity (de Silva et al., 2016, 2018). Despite these outcomes, further refinement of the structural composition in the AEM is necessary to improve its predictive capability of instantaneous spatial flow fields. To illustrate these shortcomings, figure 5.1 shows

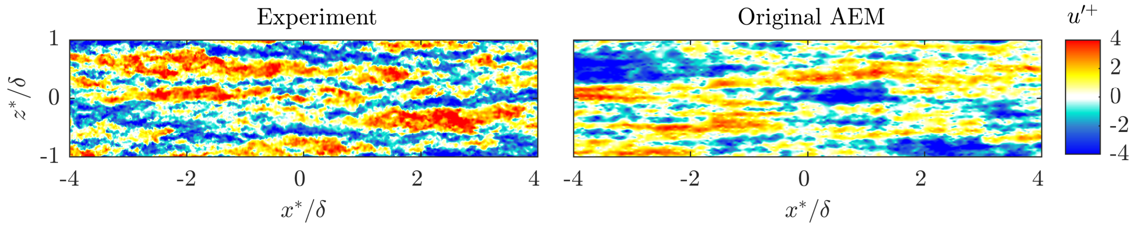

Figure 5.1: Instantaneous streamwise velocity fluctuations u'^+ on a wall-parallel plane (x^*z^*) at wall-normal height of $y^*/\delta \approx 0.06$ (within the logarithmic region). Left: Experimental data at $Re_\tau \approx 4200$. Right: Synthetic flow field generated based on the attached-eddy model at $Re_\tau = 3200$.

colour contours of the streamwise velocity fluctuations u on a wall-parallel (x^*z^*) plane in the logarithmic region of a turbulent boundary layer.

The left plane corresponds to an experimental flow field at $Re_\tau = 4200$ and the right plane corresponds to a synthetic velocity field computed from a hierarchy of representative structures from the AEM model, to be detailed further in subsequent discussions (see also Woodcock and Marusic (2015); de Silva et al. (2016)). Despite the absolute values of the streamwise velocity fluctuations u'^+, being of the same order of magnitude and the flow features being qualitatively similar, some significant differences are visible. For example, the synthetic AEM flow-fields consist of regions of high (red) and low (blue) momentum that are always aligned in the streamwise or mean flow direction, which is consistent with how the representative structures are prescribed in the model (Marusic and Perry, 1995). The experimental flow field, however, is composed of elongated structures, which meander in the streamwise direction while convecting downstream. The meandering can be understood by considering the mutual interaction between the streak like flow motions and by assuming that the attached eddies or hairpin vortices have vortical legs of different strength and are not necessarily always symmetric. In this case, the stronger leg can bend the streak more than the weak leg. This asymmetry results in the meandering nature of the streaky motion. Alternatively, it can be assumed that the attached eddies or hairpin vortex legs have the same strength but the orientation of the structure is slightly angled to the flow direction. Recent works by Kevin et al. (2019) quantified this behaviour.

Accordingly, in this chapter, a subtle modification to the placement of eddies in the AEM model is explored to introduce the meandering nature of these structures towards improving the spatial representation of the model. While this chapter focuses on the improvement of an existing, static, conceptual model, the following chapter 6 will address the large-scale structure origin based on a dynamic approach.

In contrast to the other parts of this dissertation, in this chapter δ corresponds to the boundary layer thickness calculated based on a composite fit (Chauhan et al., 2007), which has been reported to be better suited when drawing comparisons to the synthetic AEM flow fields (de Silva et al., 2016). As the AEM is composed based on viscous scaling, the turbulent fluctuations are normalised accordingly. The corresponding experiments and scaling parameters are given in chapter 3.

5.1. Synthetic AEM flow fields

The synthetic flow fields from the AEM are computed based on a packet of Λ-eddies described in Marusic (2001) which is depicted in figure 5.2. To date, this representative eddy has been shown to provide a good statistical representation of a turbulent boundary layer in the log-layer region (Marusic and Perry, 1995). A comprehensive mathematical description and instructions on how to generate the AEM flow fields can be found in Woodcock and Marusic (2015) and de Silva et al. (2016) respectively. To summarise, the vortex rods that constitute each Λ-eddy are assumed to contain a Gaussian distribution of vorticity about its core. To obtain a corresponding velocity field, Biot-Savart calculations are performed over all vortex rods present in a single representative eddy. This process is then repeated for each eddy within a packet and at different hierarchical length scales (Marusic and Perry, 1995). It is noted that the representative length scales of eddies follow a geometric pattern, which can be exploited to minimise the computational cost due to the self-similarity of the structures at different hierarchical sizes. The assumption of self-similarity is supported by Sharma et al. (2017). Further, the spatial population density and domain size are held constant and selected such that the mean streamwise velocity profile in the logarithmic region satisfies the logarithmic-law constants (de Silva et al., 2016).

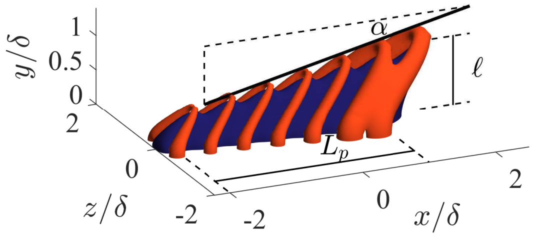

Figure 5.2: Schematic of a typical representative Λ eddy used to generate the synthetic flow fields from the attached-eddy model, adapted from de Silva et al. (2016). The blue region corresponds to the low-momentum region that forms beneath the packet of Λ eddies and the red region corresponds to a higher-speed region.

5.2. Results and Discussion

5.2.1. Comparisons of the original AEM configuration with experimental data

The qualitative comparison between the synthetic AEM flow fields in figure 5.1 revealed some clear differences. To quantify these observations, statistical two-point correlations functions are computed for both databases. The results are presented in figure 5.3, which shows the two-point correlation function $R_{u'u'}$ for a wall-parallel plane at the same wall-height ($y^*/\delta = 0.06$), shown previously through instantaneous u contours in figure 5.1. A comparison of the positive regions of $R_{u'u'}$, reveals that results from the synthetic AEM flow fields are wider in the spanwise direction and more elongated in the streamwise direction. This can be explained through assumptions in the model. Specifically, the elongated correlations in x^* are caused by streamwise aligned eddies within a packet, which induces fluid with relatively similar velocity in their core region (blue region in figure 5.2), while between packets high momentum flow regions are generated dependent on the spanwise separation. Furthermore, the placement of eddies is such that they are all aligned to the flow direction, while the experimental data exhibits that these regions of coherence appear to meander and are not necessarily always aligned to the direction of the flow (Kevin et al., 2019). These spatial differences are inherently associated with the dynamics of the eddies in a turbulent boundary layer and their spatial organisation, which is aimed to address towards better representing these flow structures instantaneously in the attached-eddy model.

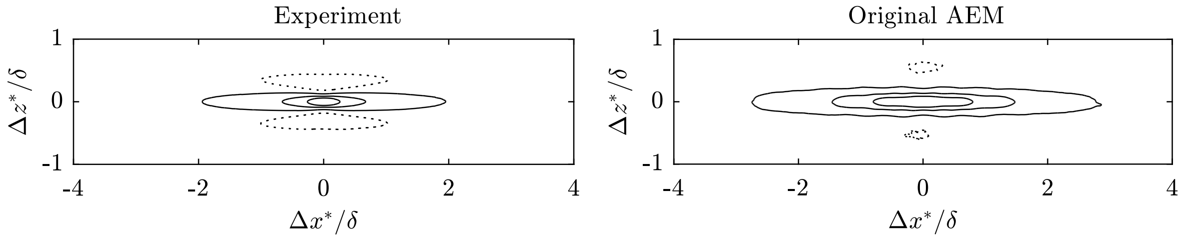

Figure 5.3: Two-point correlation coefficient $R_{u'u'}$ computed on a wall-parallel plane at $y^*/\delta = 0.06$. Left: Experimental database at $Re_\tau = 4200$. Right: AEM synthetic flow fields at $Re_\tau = 3200$. Solid lines represent positively correlated contour levels of $R_{u'u'} = 0.1,\ 0.3,\ 0.5$ and the dotted lines show negative correlation contour at $R_{u'u'} = -0.05$.

5.2.2. The influence of meandering structures in the attached-eddy model

From its conception, the placement of representative eddies in the AEM is considered to be aligned with the direction of the flow (Perry et al., 1986; Marusic, 2001). Instead, based on the preceding discussions, to include a degree of meandering in the flow structures, it is considered that the eddies are allowed to be angled to the direction of the flow. Specifically, a a parameter θ is introduced that corresponds to the angle between the major axis of the representative Λ- eddies and the flow direction, illustrated in figure 5.4. To introduce this modified AEM configuration the distribution of θ is based on the meandering angle distribution reported by Kevin et al. (2019) for coherent regions of streamwise velocity in turbulent boundary layers.

A PDF of the imposed distribution of θ is reproduced in in figure 5.4. In addition, results from a Gaussian fit to the same distribution (solid line) reported by Kevin et al. (2019) is included along with a second distribution with an increased standard deviation (dashed line) . These distributions will be employed in the subsequent discussions to assess the influence of the distribution of θ. It should be noted, the proposed methodology to introducing meandering of the representative structures in the AEM without any modification to the eddy shape, minimises any impact on the mean-flow statistics which have been reported to be in good agreement to experimental data (Woodcock and Marusic, 2015; de Silva et al., 2016). To quantify the influence of the meandering on the flow velocities, the probability distribution of the streamwise u'^+ and spanwise w^+ fluctuations from the modified and original synthetic AEM flow fields are compared to the experimental data in figure 5.5. The results reveal minimal impact on u' while w' appears to better represent the experimental data.

Figure 5.6 shows colour contours of streamwise velocity fluctuations of the original AEM configuration (top), the modified AEM configuration (centre) and the reference experimental data (bottom). Results are presented at two wall-normal heights of $y^*/\delta \approx 0.06$ and $y^*/\delta \approx 0.23$. Qualitatively, the results reveal that the large-scale streamwise coherence in the modified AEM synthetic flow fields is a closer match to the experiments and exhibits meandering characteristics, similar to those from the experimental databases.

To further quantify this behaviour, the modified AEM configuration flow fields are analysed employing two-point correlations. The resulting $R_{u'u'}$ is shown in figure 5.7 at $y^*/\delta = 0.06$, $y^*/\delta = 0.23$ and $y^*/\delta = 0.45$, which reveals that the streamwise extent of the positively correlated region of $R_{u'u'}$ from the modified AEM configuration flow fields is better matched to the experiments at all wall-normal heights considered. A closer inspection of the positive

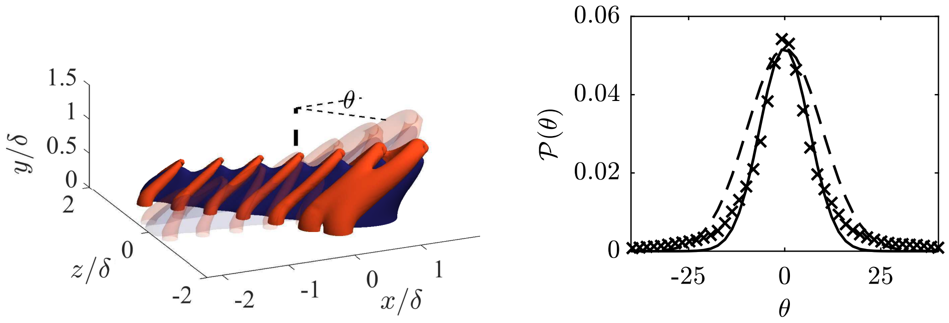

Figure 5.4: Left: Schematic illustrating the meandering angle θ which is imposed on the representative AEM structures. Right: Probability distribution of θ, where $\theta = 0$ corresponds to the streamwise direction x^*. × symbols: Distribution based on results reported by Kevin et al. (2019). Solid line (-): Gaussian fit of the experimental data with similar standard deviation σ. Dashed line (- -): Gaussian fit of the experimental data with increased standard deviation 1.5σ.

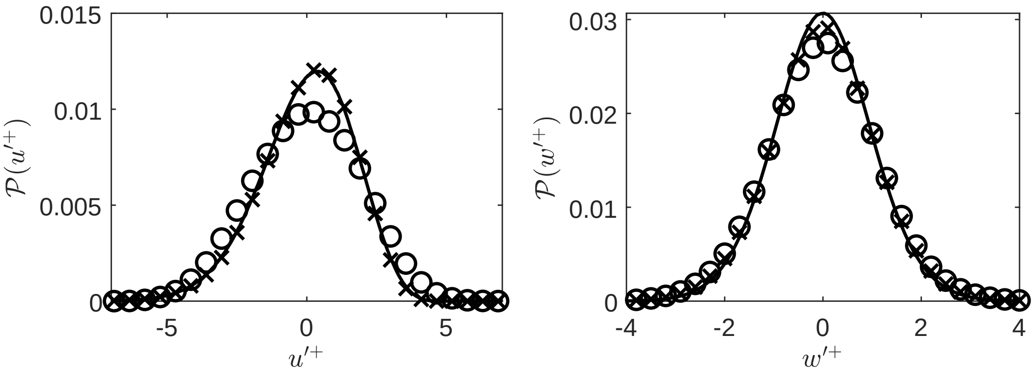

Figure 5.5: Probability distribution of the streamwise u'^+ (left) and spanwise w'^+ (right) fluctuations in a wall-parallel plane at $y^*/\delta = 0.07$. Black line (-) corresponds to the original AEM. × symbols correspond to the modified AEM. ∘ symbols represent the experimental data at $Re_\tau = 4200$.

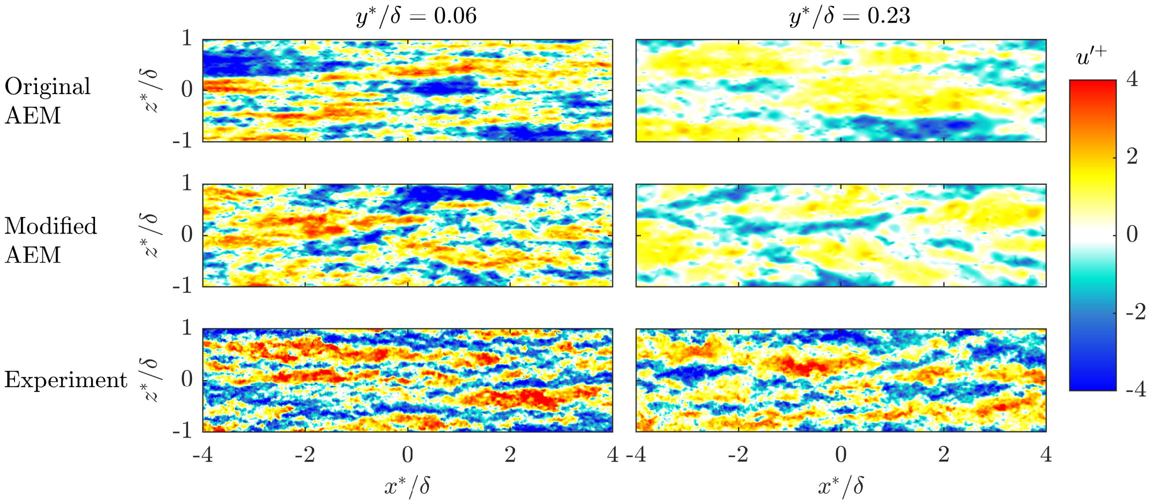

Figure 5.6: Comparison of instantaneous streamwise velocity fluctuations fields u'^+ based on the original AEM configuration(top), the modified AEM configuration (middle) and experiments (bottom). Left column: Wall distance $y^*/\delta = 0.06$. Right column: Wall distance $y^*/\delta = 0.23$.

correlation contours from the original AEM flow fields reveals a wavy shape due to the fixed spacing between the Λ-eddies in a packet and the forced streamwise alignment of all eddies, while the experimental results exhibit a narrow neck flanking the correlation point (see also (Hutchins and Marusic, 2007b)). This behaviour from the experiments also appears to be better reproduced from the modified AEM flow fields due to the asymmetry introduced due to the meandering imposed on the eddies.

In contrast to the streamwise extent, the width of the positively correlated regions in the spanwise direction is larger in the AEM flow fields. However, this is likely due to exact physical dimensions of the representative eddy shape, which has been chosen here to follow recent works (Woodcock and Marusic, 2015; de Silva et al., 2016). These works have shown that flow statistics computed employing this eddy-shape provides a logarithmic-law constant and Reynolds stresses that is in good agreement to experiments, therefore, the chosen represen-

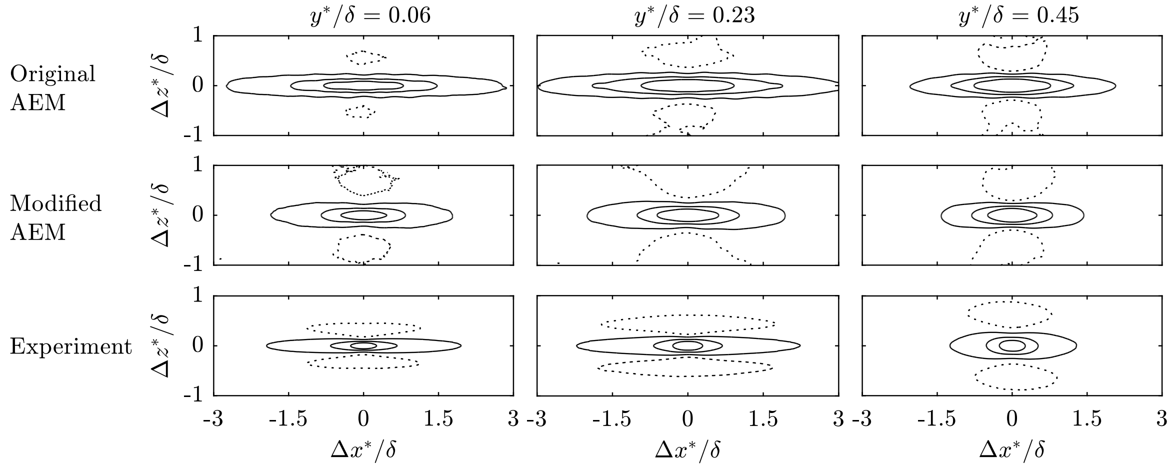

Figure 5.7: Two-point correlation coefficient $R_{u'u'}$ for wall-parallel planes at $y^*/\delta = 0.06$ (left column), $y^*/\delta = 0.23$ (middle column) and $y^*/\delta = 0.45$ (right column). Top row: original AEM configuration at $Re_\tau = 3200$. Middle row: modified AEM configuration at $Re_\tau = 3200$. Bottom row: Experiment at $Re_\tau = 4200$. Solid lines represent contour levels of $R_{u'u'} = 0.1,\ 0.3,\ 0.5$ and the dotted lines correspond to a contour level of $R_{u'u'} = -0.05$.

tative eddy forms a good baseline for the present study. It must be stressed that the present contribution is to introduce meandering to the representative eddies in the AEM towards better representing the instantaneous structures in a turbulent boundary layer.

To quantify this behaviour further, a length scale L and width scale W are calculated from the wall-parallel two-point correlation functions using a threshold of $R_{u'u'} = 0.15$ and is presented in figure 5.8. As expected, the length L of the modified AEM configuration is reduced due to the meandering and appears to better match the experimental data. To study the influence and sensitivity of the meandering angle distribution, three different distributions $P(\theta)$, as shown in figure 5.4, are tested. The results reveal that the general trend is consistent for the angle distributions. Specifically, only small differences in the length L is observed between the original distribution from Kevin et al. (2019) and a Gaussian fit, while a fit with a 50 % increase in standard deviation leads to increased meandering and therefore a slightly shorter structure length.

In addition to the streamwise length L, the spanwise width W is analysed and plotted in figure 5.8. The influence of the meandering on the width is small. In contrast to the length L, the general scaling trend is not well reproduced by the AEM. This trend is directly related to the chosen eddy shape and size and can therefore be improved by further refinement of the representative eddy employed in the AEM. Furthermore, as all eddies in the AEM are wall-coherent or “attached” to the wall inclusive of the largest eddies that extend to the outer edge of the boundary layer, the resulting width, W, from the two-point correlations is likely to be overestimated closer to the wall.

5.2.3. Cross-plane results

To draw further comparisons on the spatial coherence in the synthetic flow fields from the AEM, the cross-stream y^*z^*-plane is explored. To this end, figure 5.9 shows a comparison of instantaneous flow fields in the y^*z^*-plane from the experimental and synthetic AEM datasets. Qualitatively, a comparison between the original and modified AEM flow fields reveals that the meandering of the representative structures introduced to the model induces an asymmetry/tilt on this plane, which is closer to the behaviour observed from the

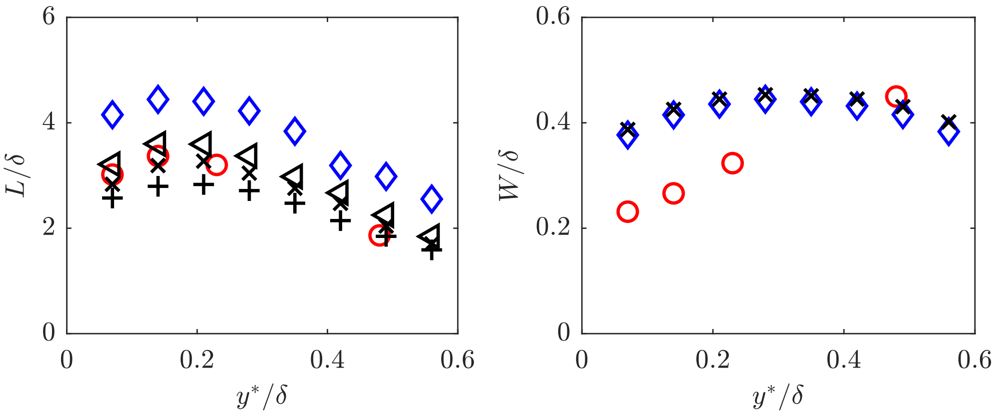

Figure 5.8: Comparison of the original AEM configuration (◇ symbols), the modified AEM configuration (× symbols) and the experimental data at $Re_\tau = 4200$ (○). × symbols correspond to results computed based on the angle distribution $P(\theta)$ form Kevin et al. (2019), while the ◁ and + symbols correspond to results computed from Gaussian distributions fitted to $P(\theta)$ with a standard deviation of $1\,\sigma$ and $1.5\,\sigma$, respectively. Left: Streamwise length L. Right: Spanwise width W. Length and width are calculated from the wall-parallel two-point correlations using a threshold of $R_{u'u'} = 0.15$.

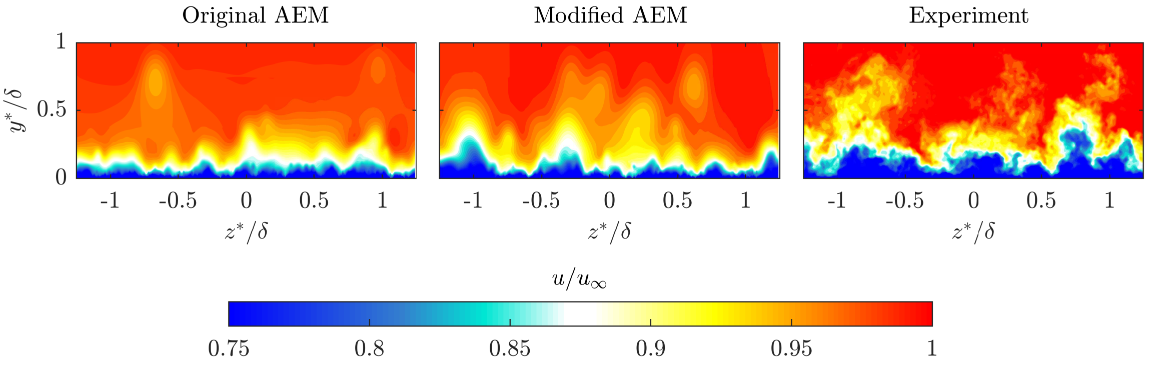

Figure 5.9: Instantaneous colour contours of streamwise velocity u/u_∞ on a cross-stream y^*z^*-plane. Left: Generated flow field based on the original AEM. Middle: Flow fields based on the modified AEM configuration. Right: Experimental data.

experiments (see also Kevin et al. (2019); Jiménez (2018)). To quantify this observation, $R_{u'u'}$ computed in the y^*z^*-plane is presented in figure 5.10 for a correlation point at a wall distance of $y^*/\delta = 0.24$. The results from all the datasets exhibit positively correlated regions flanked by regions of negative correlation, highlighting the similarity between the model and experiments. However, results from the AEM model are dominated by the largest representative eddy with a height of δ. Specifically, the AEM exhibits that the positively correlated regions of $R_{u'u'}$ near the wall are wider and become narrower with increasing y^*. This concurs with the Λ shaped eddy employed to generate the synthetic flow fields, which has a triangular form in the y^*z^*-plane. For the experimental data, the opposite is the case with a narrower region close to the wall, which is primarily due to all the structures in a turbulent boundary layer not being wall-coherent as defined by the AEM. Therefore, future refinements to the AEM are likely to involve the inclusion of wall-incoherent flow features, particularly in the wake region (see also Hwang and Sung (2018)).

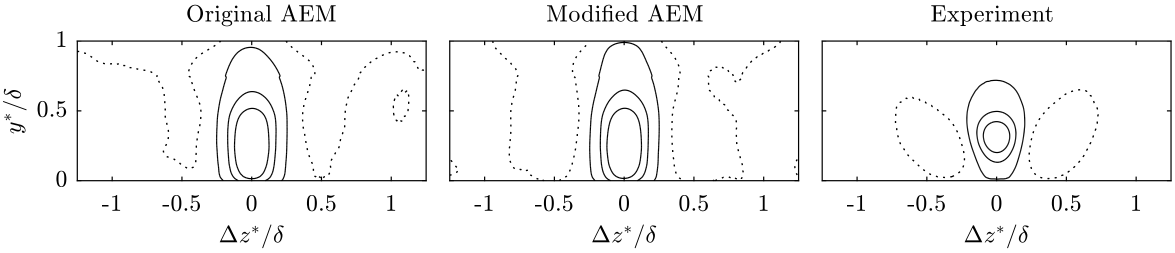

Figure 5.10: Two-point correlation coefficient $R_{u'u'}$ for a correlation point at $y^*/\delta = 0.24$. Left: Original AEM configuration. Middle: Modified AEM configuration. Right: Experimental data. Solid lines represent positive correlated areas, dotted lines negative correlation.

Overall, the modified AEM configuration improved the spatial representation of the streamwise velocity component u of the synthetic flow fields by the AEM in the logarithmic region. Absolute deviations in width or height are parameters which themselves depend on the eddy shape used and the chosen eddy size. Furthermore, the two-point correlation provides a measure of the spatial scales, e.g. the width, based on a chosen threshold. One should also keep in mind that small-scale turbulence influences the magnitude of the positive correlation on average and is not present in the AEM when moved away from the wall. On the other hand, the PIV fields are inherently spatially low pass filtered by the measurement technique. Specifically, the spatial resolution of a PIV measurement is directly dependent on the final interrogation window size or double the vector spacing, which equals 160 viscous units for wall-parallel measurements and 140 viscous units for the cross-stream plane measurements.

5.2.4. Analysis of the spanwise velocity component

In the preceding discussions, the streamwise velocity fluctuations u' was examined. Recent works by Sillero (2014); de Silva et al. (2018), also highlighted particular patterns in the large-scale spanwise coherence of the spanwise velocity within turbulent boundary layers. In a similar fashion, figure 5.11 shows the instantaneous spanwise velocity fluctuations w^+ between the synthetic AEM flow fields and the experiments on wall-parallel planes at $y^*/\delta = 0.06$ and $y^*/\delta = 0.23$. The results show a strong periodicity in flow direction for the original AEM configuration (top), while the modified AEM configuration (centre) and the experiments (bottom) exhibit better agreement. Similar to the flow fields of u'^+ in figure 5.6, the AEM flow fields appear less turbulent, especially in the plane further away from the wall at $y^*/\delta = 0.23$, due to the absence of small-scale turbulence in the AEM with increasing y^*.

To quantify the spatial features in the w' coherence further, figure 5.12, shows $R_{w'w'}$ computed on x^*z^*-planes at $y^*/\delta = 0.06$ (left column), $y^*/\delta = 0.23$ (middle column) and $y^*/\delta = 0.45$ (right column). The results reveal that the spatial extent of the coherence for w' is less compared to u', which is in line with previous observation in literature, Hutchins et al. (2005); Sillero (2014); de Silva et al. (2018). A strong periodicity in $R_{w'w'}$ is observed from the original AEM configuration flow fields with a wavelength equal to eddy spacing with the representative packet eddy employed. This artificial periodicity is significantly reduced by the meandering introduced in the modified AEM configuration, leading to an improved agreement to the experiments. Further, the spatial extent of the w coherence also appears to be better matched between the modified AEM configuration and the experiments.

The contours of $R_{w'w'}$ exhibit a squarish shape from all datasets similar to that reported by Sillero (2014); de Silva et al. (2018). Inspired by these observations on the x^*z^*-plane, contours of $R_{w'w'}$ from the y^*z^*-plane are shown in figure 5.13 for the modified AEM configuration and experiments. Results are computed at $y^*/\delta = 0.2$ (black) and $y^*/\delta = 0.8$ (red).

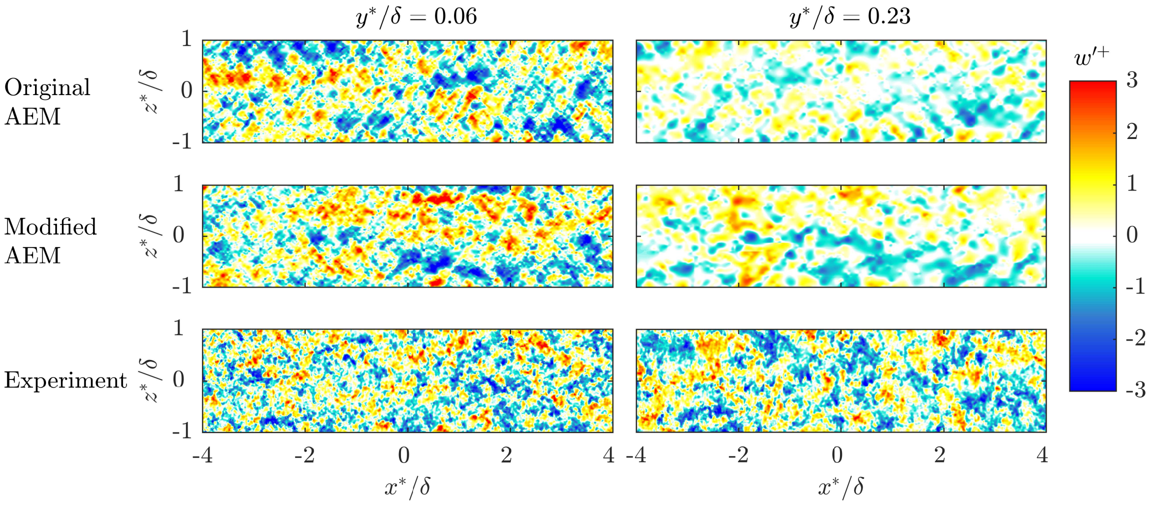

Figure 5.11: A comparison of instantaneous spanwise velocity fluctuations v^+ based on the original AEM configuration(top), the modified AEM configuration (middle) and experiments (bottom). Left column: Wall distance $y^*/\delta = 0.06$. Right column: Wall distance $y^*/\delta = 0.23$.

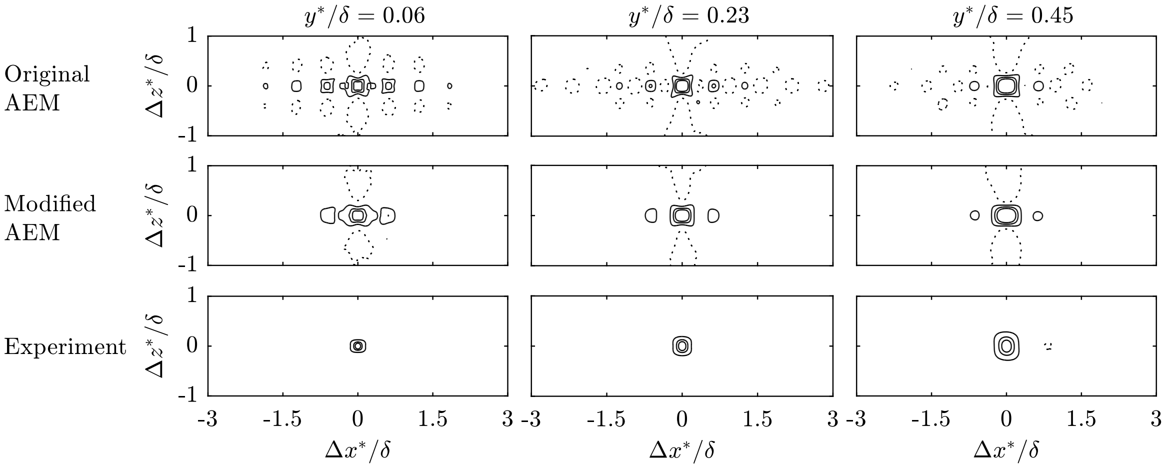

Figure 5.12: Two-point correlation coefficient $R_{w'w'}$ for the spanwise velocity fluctuations computed on wall-parallel planes at $y^*/\delta = 0.06$ (left column), $y^*/\delta = 0.23$ (middle column) and $y^*/\delta = 0.45$ (right column). Top row: Original AEM configuration at $Re_\tau = 3200$. Middle row: Modified AEM configuration at $Re_\tau = 3200$. Bottom row: Experiment at $Re_\tau = 4200$. Solid lines represent contour levels of $R_{w'w'} = 0.15,\ 0.3,\ 0.45$ and the dotted line corresponds to a contour level of $R_{w'w'} = -0.075$.

To emphasise the influence of w, the fields are conditioned on $w' < -0.5\sigma_{w'}$ and $w' > 0.5\sigma_{w'}$, where $\sigma_{w'}$ corresponds to the standard deviation of w'. At $y^*/\delta = 0.8$, the conditional results reveal a strong diagonal orientation dependent on the sign of w' in both the experiments and the modified AEM flow fields similar to the findings of Sillero (2014); de Silva et al. (2018) on the x^*z^*-plane. These findings also agree with the conceptual ‘leaning’ behaviour discussed in (Kevin et al., 2019). Closer to the wall at $y^*/\delta = 0.2$ all databases reveal a squarish/elliptical shape, however, if $R_{w'w'}$ is conditioned on the direction of w', the same diagonal orientation is observed, albeit less pronounced, particularity in the experiments. Further, the coherence from the AEM fields exhibits a larger spatial extent with increasing y^* as the eddy size in-

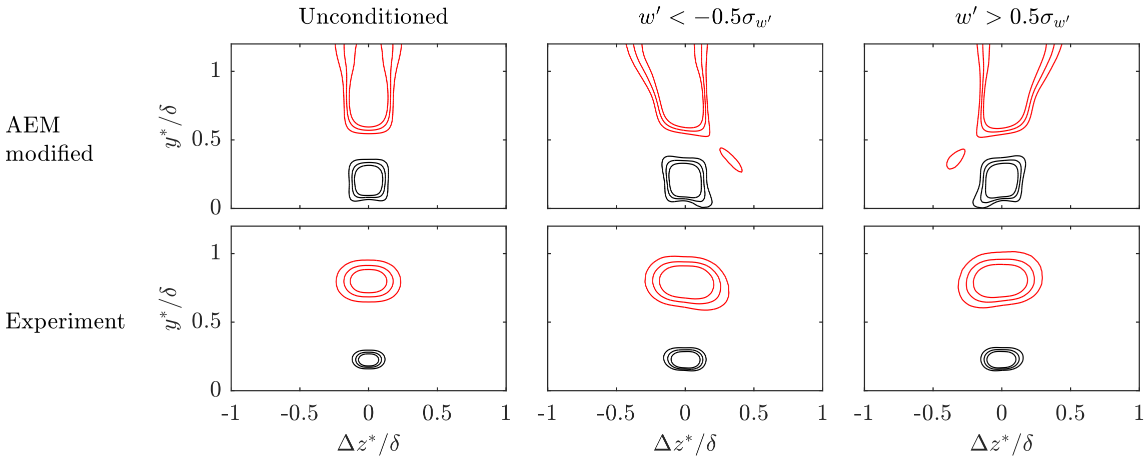

Figure 5.13: Conditioned two-point correlation coefficient $R_{w'w'}$ for a correlation point at $y^*/\delta = 0.2$ (black) and $y^*/\delta = 0.8$ (red). Top row: modified AEM configuration. Bottom row: Experimental data. Solid lines represent contour levels at $R_{w'w'} = 0.3,\ 0.4,\ 0.5$. The left column represents all data, middle column conditioned in the correlation point on $w' < -0.5\sigma_{w'}$, right column conditioned on $w' > 0.5\sigma_{w'}$.

creases with the wall distance. This effect is directly visible when comparing the correlation results at $y^*/\delta = 0.2$ and $y^*/\delta = 0.8$. To improve the spatial representation, it is, therefore, necessary to decorrelate large eddies from the wall. In the experimental data, this effect is inherently present, because all turbulent structures are not "attached" to the wall, which leads to a decorrelation in the near-wall region.

6

On the origin of large-scale structures

In this chapter, the question of the origin of large-scale structures in a turbulent boundary layer flow is addressed. Many theories about the origin have been developed in the past, of which a brief overview is given and discussed in section 2.2. Most of the earlier theories are based on a statistical analysis, visualisation techniques and single-point data. In recent years, quantitative field measurements such as PIV and numerical flow simulations were used to review and extend the existing explanations. The following analysis approaches this question from a perspective based on observations of instantaneous spatial flow fields, whereby the flow field in the vicinity of large-scale structures is also investigated. Based on these observations and a literature review, a conceptual model based on vortex dynamics is introduced in section 6.1. To quantify the observations in the instantaneous flow fields and to support and verify the conceptual model, the vortex structure within the turbulent boundary layer flow is discussed in section 6.2.

One major problem in turbulence research is that similar data and observations can be interpreted differently. Therefore, the introduced conceptual model is reviewed in section 6.3 in contrast to existing models, such as the hairpin theory or the attached eddy model, to highlight similarities and differences.

6.1. Introduction of a conceptual self-sustaining process

To understand the origin and dynamics of large-scale structures, the flow field in the vicinity of the structure has to be studied. Therefore, the cross-stream plane SPIV measurements are the best suited, because all three velocity components are measured and a picture of the whole boundary layer up to $1.2\,\delta_{99}$ is captured. In figure 6.1 the fluctuation field in a cross-stream yz-plane is shown. Red contours correspond to high-momentum fluid, blue contours to low-momentum fluid. Up to $y^*/\delta_{99} = 0.3$, high- and low-momentum fluid appears intermittently. These are large-scale streamwise structures, aligned in a streaky pattern in spanwise direction (Hutchins and Marusic, 2007b; Tomkins and Adrian, 2003). In between the areas of comparable momentum, regions with high shear in streamwise direction are created due to the streamwise velocity difference. Considering the in-plane flow field, illustrated by the vector arrows in figure 6.1, a three-dimensional flow field is apparent. At $z^*/\delta_{99} = 0.15$ a strong ejection event ($v' > 0$) penetrating into the outer boundary layer is visible. The ejection is connected with a spatially large area of low-momentum, as also discussed in detail in section 4.3. At the head of the ejection event, small vortex structures are present. These structures are presumably hairpin necks, as observable in figure 2.7. On both sides of the ejection, different larger vortices are present. These vortices are responsible for the outward motion of the ejection event and on their other side for a sweep of high-momentum fluid into

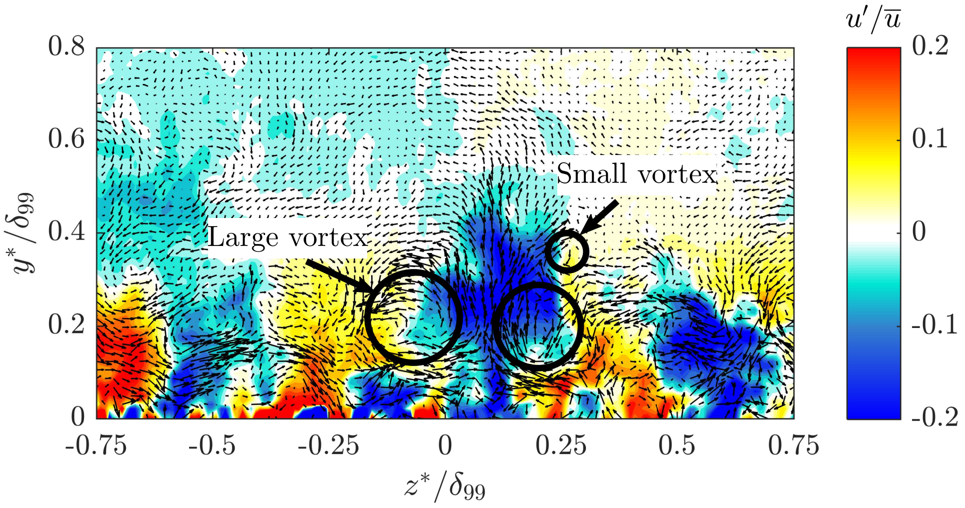

Figure 6.1: Instantaneous velocity field in the y^*z^*-plane at $Re_\tau = 12000$. Contour levels correspond to the normalised streamwise velocity fluctuations $u'/\overline{u}$. The vectors show the in-plane velocity fluctuations v' and w' in wall-normal and spanwise directions. Significant vortices are highlighted.

the near wall region. In effect, the vortices are redistributing streamwise momentum within the boundary layer, as high-momentum fluid is shifted towards the wall and low-momentum fluid into the outer boundary-layer region. Another instantaneous flow field of the same plane is shown earlier in figure 4.7 and can be used for comparison. In figure 4.7 the same principal features are found around the ejection event at $z^*/\delta_{99} = 0.25$. Two small vortex structures at the head of the structure are also apparent.

In an analytical study, Waleffe (1997) proved the potential of a self-sustaining process within turbulent shear flow to generate meandering structures from streamwise rolls which redistribute the mean shear. Due to the redistribution of the mean shear streaks are produced, and additionally the mean velocity exhibits a strong spanwise component. The spanwise motions lead to a wave like instability which energises the streamwise vortices. Strong spanwise motions associated with ejections were also found and quantified the statistical analysis in chapter 4.

The findings of Waleffe's (1997) study do not explicitly explain all the observations in the turbulent boundary layer flow, but lead to the idea of a related self-sustaining process within the turbulent boundary layer flow. In figure 6.2 a self-sustaining regeneration process of large-scale structures based on large streamwise rolls is schematically shown. It consists of three principal steps. In a first step 1, a large streamwise vortex redistributes the mean streamwise momentum. High-momentum fluid $u' > 0$ from the outer boundary layer is shifted closer to the wall and vice versa. As the differences between the velocity at a certain wall-normal position y_i and the redistributed fluid increases with the distance between the position y_i and the origin of the fluid, this results in high streamwise velocity gradients in spanwise direction between fast (red) and slow (blue) regions in the flow. Between those regions, areas with high shear occur. This leads, in the second step of the process, to a Kelvin-Helmholtz instability which generates vortices with its rotational axis normal to the wall. While the wall-normal vortices convect downstream, they are bent due to the mean velocity gradient normal to the wall, which is shown in step 3 in figure 6.2. As the flow further away from the wall is faster on average, the vortices are bent towards the wall which finally results in a

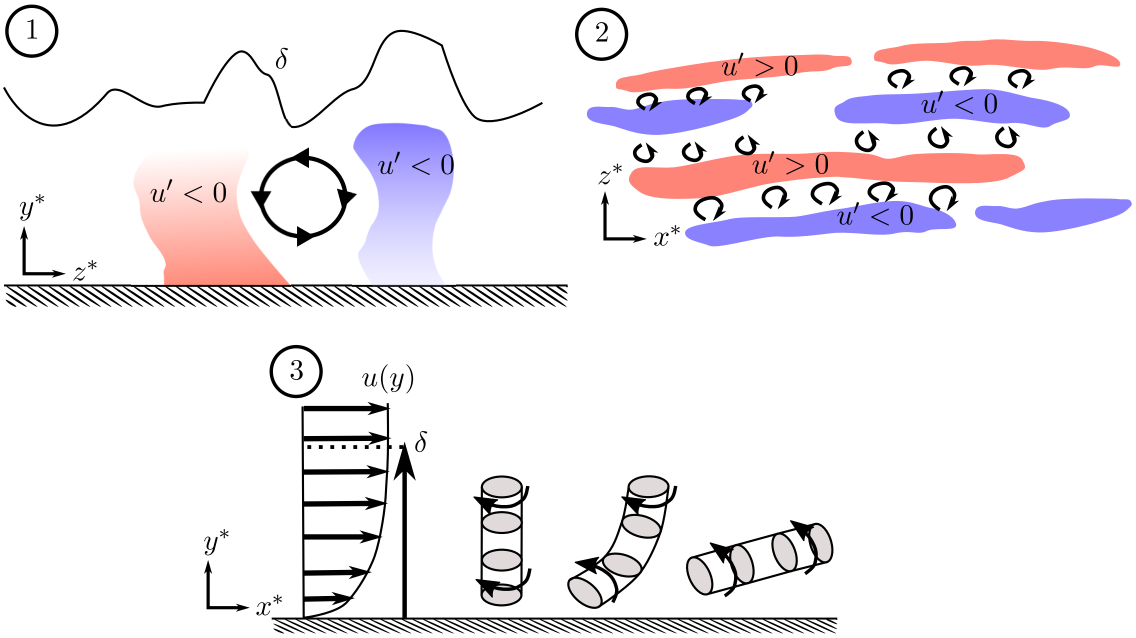

Figure 6.2: Pricipal sketch of the self-sustaining process of large-scale structure generation. 1: Redistribution of mean momentum due to large streamwise vortices. 2: Kelvin-Helmoltz instability in the wall-parallel plane due to resulting streamwise velocity gradients. 3: Bending of vortices caused by the mean velocity profile leads to streamwise vortices.

quasi streamwise vortex. Due to the spanwise motion induced by the large vortex, the small bent Kelvin-Helmholtz vortices are energised, which leads to large-stream wise vortices and closes the self-sustaining process. Hence, the origin of large-scale structures can be explained by the redistribution of the momentum as shown mathematically by Waleffe (1997).

Once this process is initiated, it is self-sustaining. A major open question is where the beginning of this process, namely the first streamwise vortices, come from. This question cannot be answered by the data presented in this thesis, but a time-resolved measurement or simulation of the boundary layer development and transition process is necessary at a sufficiently high Reynolds number. At this point, it can only be assumed that the streamwise vortices are either a feature of the transition process, such as a remainder of the Λ-shape vortices which occur during the transition, or that random turbulent vortices start the process initially.

6.2. Characterisation of the vortices in the turbulent boundary layer

The self-sustaining process concept introduced and explained above relies on instantaneous observations. Therefore, it is necessary to investigate if the described process is generally present and a characteristic feature of a turbulent boundary layer flow. To find experimental evidence and to validate the mechanism, the vortical structure of the turbulent boundary layer flow is quantified in the following in two steps. In section 6.2.1 the size, strength and spatial distribution of the vortices in the turbulent boundary layer flow is analysed. Afterwards, the path of detected vortex cores is reconstructed from time-resolved data in section 6.2.2.

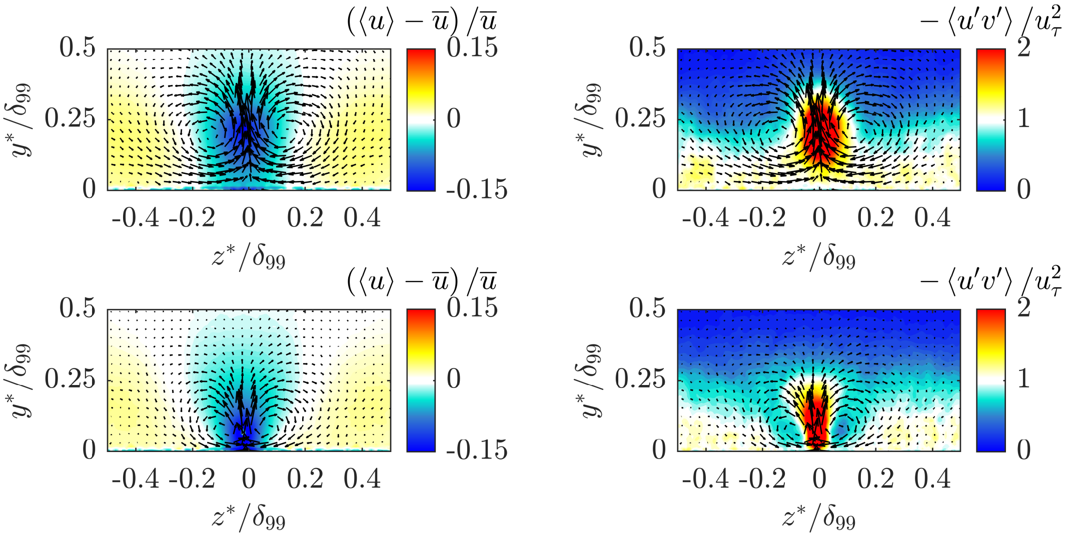

Figure 6.3: Left: Conditional averaged streamwise velocity fluctuations $(\langle u \rangle - \overline{u})/\overline{u}$. Vectors indicate the in-plane velocity components at $Re_\tau = 12000$. Condition was set to $u' < 1\sigma_u$. Right: Conditionally averaged shear stress $-\langle u'v' \rangle / u_\tau^2$ at $Re_\tau = 12000$. Top row: Condition applied at wall distance $y^*/\delta_{99} = 0.23$, bottom row: $y^*/\delta_{99} = 0.07$.

6.2.1. Vortex size and distribution

In order to identify the vortices, which on average have an influence on the structures, conditionally averaged flow fields are calculated. The data is conditioned on strong ejection events at wall distances $y^*/\delta_{99} = 0.23$ (top row) and $y^*/\delta_{99} = 0.07$ (bottom row), for which $v' > 0$ and $u' < -1.5\,\sigma_u$. In the left column of figure 6.3 the conditioned mean deviation field $(\langle u \rangle - \overline{u})/\overline{u}$ is plotted, with the in-plane velocity components represented by vectors. The two flanking vortices are also present in the averaged flow fields, which is not the case for the smaller vortices above the ejections. This proves that flanking vortices are a necessary feature of an ejection, whereas the top vortices are a random result induced from shear on top of an ejection. Comparable patterns were described in the predictive model by Marusic et al. (2010).

The plots in the right column of figure 6.3 show the conditional averaged Reynolds shear stresses $-\langle u'v' \rangle / u_\tau^2$, which are a measure for the turbulence production in a ZPG turbulent boundary layer flow, as discussed in section 2.1. Within the ejection, the turbulence production is increased strongly in comparison to the rest of the boundary layer. This highlights the importance of coherent events within the turbulent boundary layer flow for the generation of turbulence itself. Closer to the wall, below $y^*/\delta_{99} < 0.25$, positive values of the turbulence production are present, above the production drops gradually to zero. As proven in section 4.3, strong sweep and ejection events are associated with in streamwise direction elongated structures. Hence, large-scale structures are connected with the turbulence production in the turbulent boundary layer flow.

In the following, the size and circulation of the flanking vortices in the conditional averaged flow fields and of vortices detected in the instantaneous flow fields in the cross-stream yz-plane at $Re_\tau = 12000$ are analysed. The vortex detection is based on the method introduced and tested by Graftieaux et al. (2001), which provides a robust detection technique for vortices in instantaneous PIV flow fields. Based on this, the circulation is estimated as the sum of vorticity within the core radius r_0 of the vortex times the core area A_0. This is possible as

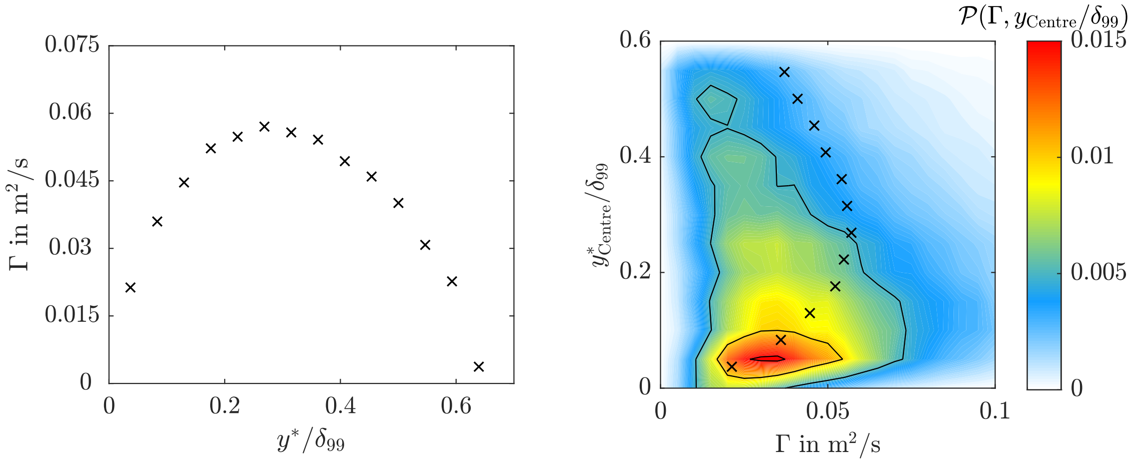

Figure 6.4: Left: Circulation Γ of the flanking vortices from the conditionally averaged fields at $Re_\tau = 12000$ as a function of the wall distance y^*/δ_{99}. Right: Joint probability distribution of the vortex circulation Γ and the wall distance of the vortex centre $y^*_{\mathrm{Centre}}/\delta_{99}$ at $Re_\tau = 12000$. × symbols correspond to the conditioned vortex circulation shown in the left plot.

the vector spacing Δx is approximately one order of magnitude smaller than the diameter d of the flanking vortices, as is shown in appendix A.4, where the technique is also explained, tested and qualified in detail.

In figure 6.4 (left) the average circulation Γ of the conditional flanking vortices as a function of the wall distance of the vortex centre $y^*_{\mathrm{Centre}}/\delta_{99}$ is shown. The strongest contributing vortices to the ejection have their centre at a wall-normal position of $y^*/\delta_{99} = 0.28$. In the outer boundary layer, above $y^*/\delta_{99} > 0.6$, no distinct flanking vortices cen be detected. Figure 6.4 (right) shows the joint probability distribution of the circulation Γ and the wall distance of the vortex centre $y^*_{\mathrm{Centre}}/\delta_{99}$ calculated from detected vortices in 14000 instantaneous flow fields. The × symbols represent the distribution from the conditional averaged analysis shown in figure 6.4 (left). The flanking vortices in the conditional fields are close to the wall ($y^*_{\mathrm{Centre}}/\delta_{99} \approx 0.05 - 0.1$) in the most probable area of the joint probability distribution. Further outside, the conditional average flanking vortices have a higher circulation than the most probable vortices. This is a result of two effects. First, the conditioning on a strong ejection event involves stronger vortices than an average ejection. Second, due to the continuity of fluid, the conditioning on a strong ejection leads to an equal inward movement on average, which results in a more ideal vortex than detected in the instantaneous flow fields. This leads to an overestimation of the circulation strength in the conditioned fields.

So far, the vortices were assumed to be a general feature in the boundary layer flow. This is only true, if in all instantaneous flow fields vortices are detected. Therefore, the number of detected vortices is analysed and plotted in figure 6.5. The left plot shows the average number of vortices as a function of the wall distance in 12 discrete bins with a bin width of $0.05\,\delta_{99}$. The maximum number of vortices is detected in the logarithmic layer or directly above. Overall, the vortex population density is decreasing with the wall distance. Near the wall structures are generated and interact dynamically with the presence of vortices. Further outside, the turbulent fluid is pushed out by the ejection into the laminar potential flow and new high-momentum fluid is is converted into turbulence (Reuther and Kähler, 2018).

The cumulative number of vortices detected on average in instantaneous fields is plotted in figure 6.5 (right). On average 14 large vortices, with a core diameter of at least 8 vectors,

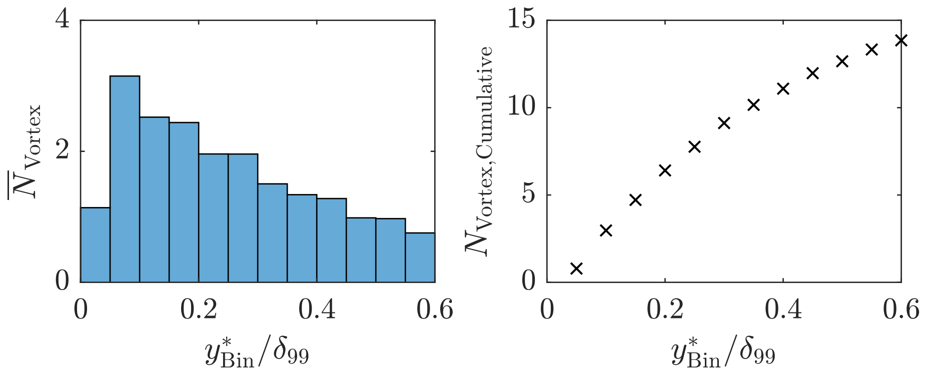

Figure 6.5: Left: Average number of vortices per bin at $Re_\tau = 12000$. Right: Cumulated number of vortices at $Re_\tau = 12000$.

are detected per instantaneous flow field. Hence, the vortices are present in all fields in a sufficient number and can therefore be considered as a general feature.

In figure 6.6 (left) the joint probability distributions of the vortex core diameter d/δ_{99} and the wall distance of the vortex centre $y^*_{\mathrm{Centre}}/\delta_{99}$ is plotted. Closer to the wall, it is more likely to detect a vortex. Also the vortices are slightly smaller close to the wall but the overall influence of the wall distance on the distribution of the vortex core diameter d/δ_{99} is small. This shows that the vortex generation and driving mechanism is not primarily limited to the near wall region, but vortices are present and can in general also be generated at various heights, as long as sufficient shear instability is present. It should be noted here that due to the uncertainty analysis discussed in appendix A.4, only vortices with at last 8 vectors core diameter were accounted for in this analysis.

The plot in figure 6.6 (right) shows the joint probability distribution of the circulation Γ and the vortex core diameter. Evidently, the larger the vortex diameters are, the more likely is an overall higher circulation. In summary it can be stated that large flanking vortices with comparable strength are present in instantaneous flow fields and average flow fields which proves that the vortices are a principle flow feature, associated with sweep and ejection events, and therefore with elongated structures.

So far, the flow fields in the cross-stream y^*z^*-plane are analysed. The important mechanism of the self-sustaining regeneration process is that vortices generated from streamwise shear with their rotation axis normal to the wall are bent and result in streamwise vortices. In order to make this connection, the flow fields in the wall-parallel planes are taken into account and examined. In figure 6.7 the instantaneous flow field in a wall-parallel x^*z^*-plane is plotted with vortex centre locations highlighted. Most of the vortex centres are in the shear layer region between high- and low-momentum structures. To quantify this observation, the probability distribution of the velocity fluctuations from all data points in the wall-parallel planes and the locations with a detected vortex centre are calculated. The probability distribution is plotted in figure 6.8. While a broader distribution is present for the complete data set, which is skewed towards positive fluctuations, the distribution of the fluctuations conditioned on a vortex centre is narrower and nearly Gaussian. The most probable fluctuation in the vortex centre is $u'/u_\tau \approx 0$. Hence, the vortex core is most probably in the neutral region/ the shear layer in between large-scale structures.

Examining the shape of the structures in figure 6.7 more closely, focusing on the shear layer, a Kelvin-Helmoltz formation is visible at the side of the strong high-momentum structure at $z^*/\delta_{99} = 0.9$. But also vortices are identified, which are not directly linked to a Kelvin-Helmholtz structure like pattern.

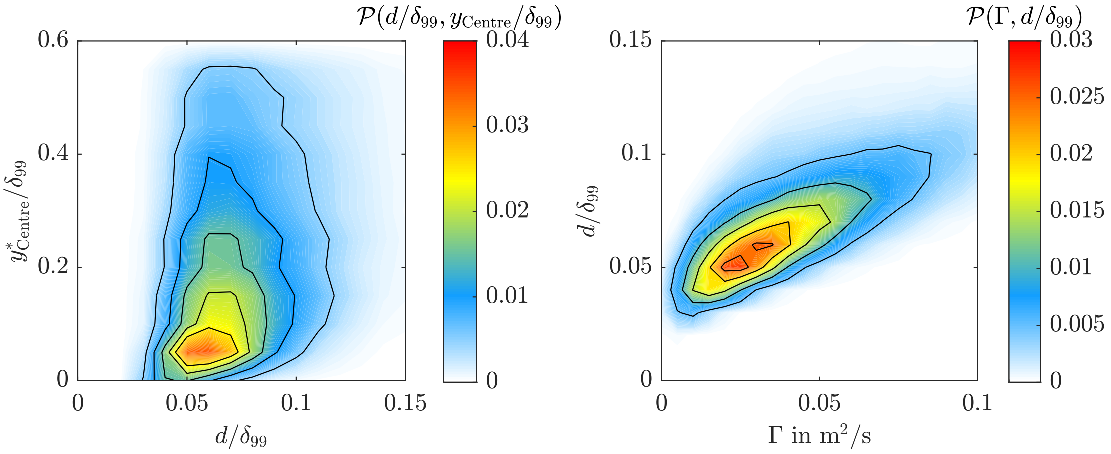

Figure 6.6: Left: Joint probability distribution of the vortex core diameter d/δ_{99} and the wall distance of the vortex centre $y^*_{\text{Centre}}/\delta_{99}$ at $Re_\tau = 12000$. Right: Joint probability distribution of the vortex core diameter d/δ_{99} and the circulation Γ of the vortices at $Re_\tau = 12000$.

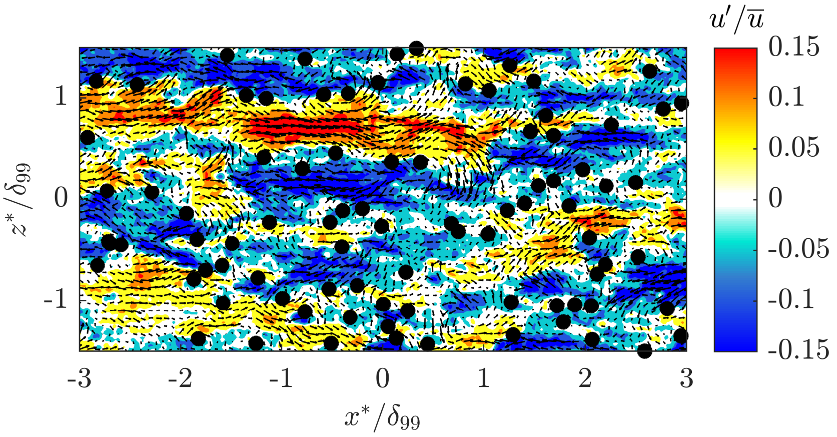

Figure 6.7: Instantaneous normalised velocity fluctuation $u'/\overline{u}$ at $Re_\tau = 13400$ and a wall distance $y^*/\delta_{99} = 0.14$. • symbols correspond to identified vortex centre locations, the vectors to the instantaneous in-plane velocity field.

Both results support the idea that vortex generation is taking place due to shear instability in streamwise direction. For the formation of Kelvin-Helmoltz instability in a shear layer, no minimal velocity difference is necessary but the instability occurs when a small disturbance is present and fanned (Nieuwstadt et al., 2016). Clearly, stronger velocity differences/ shear layers promote the generation. This is different to buoyancy driven Kelvin-Helmholtz instabilities, where defined density gradients are necessary for the instability onset (Nieuwstadt et al., 2016).

To combine the findings, the vortex structure in the wall-parallel plane is quantified similarly to the analysis in the cross-stream plane. In figure 6.9 the joint probability distributions of the vortex core diameter d/δ_{99} and the circulation Γ in wall-parallel planes at $y^*/\delta_{99} = 0.07$ (left) and $y^*/\delta_{99} = 0.28$ (right) at $Re_\tau = 13400$ are plotted. For comparison, the distribution from the cross-stream plane is plotted as dashed lines. Between the wall distance no distinct differences in the general trend are present. Closer to the wall, at $y^*/\delta_{99} = 0.07$, the

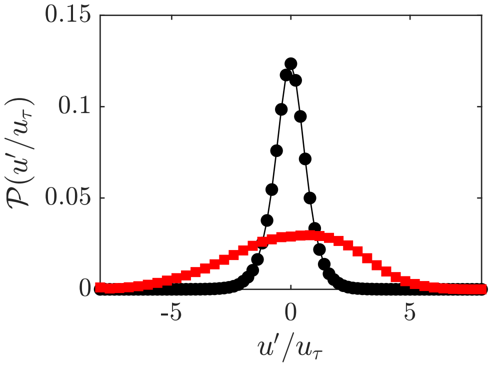

Figure 6.8: Probability distribution of the normalised fluctuations u'/u_τ in a wall-parallel plane at $y^*/\delta_{99} = 0.14$ at $Re_\tau = 13400$. ● symbols correspond to fluctuations in a vortex centre location, 🟥 symbols to the complete data set.

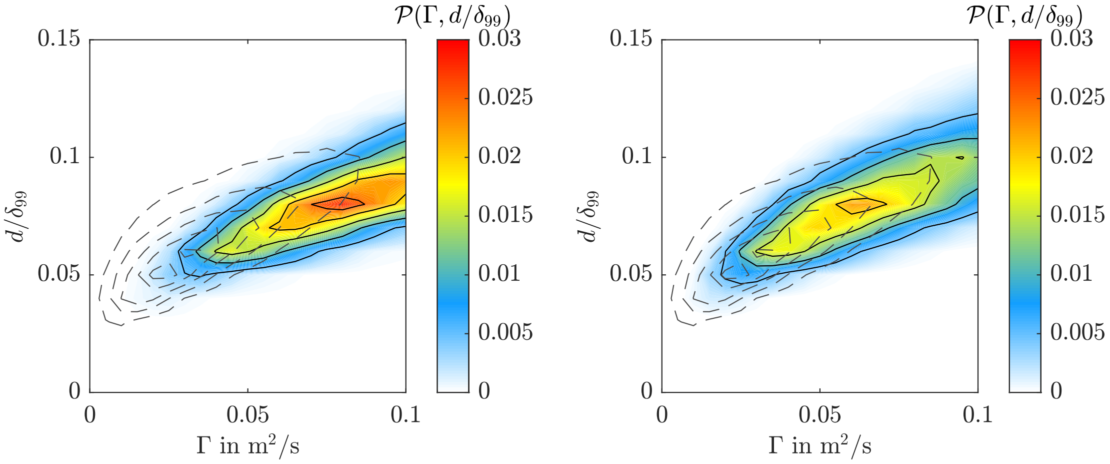

Figure 6.9: Joint probability distribution of the vortex core diameter d/δ_{99} and the circulation Γ of the vortices at $Re_\tau = 13400$ in wall-parallel planes. Left: Wall distance $y^*/\delta_{99} = 0.07$. Right: Wall distance $y^*/\delta_{99} = 0.28$. Dashed lines represent the distribution in the cross-stream plane at $Re_\tau = 12000$ from figure 6.6 (right).

maximum probability is higher, while for the higher wall-distance the distribution is broader. Furthermore, the distribution closer to the wall is shifted towards higher circulations, which shows that the vortices near the wall are stronger for an identical diameter. Comparing the results from the wall-parallel planes with the cross-stream plane, the same trend is present. The larger the vortex diameter, the higher is the circulation on average. Due to the coarser spatial resolution in wall parallel planes, only vortices with larger diameters are detected. That explains the shift towards larger diameter d/δ_{99} values for the wall-parallel planes.

Following the line of thought of the self-sustaining process introduced in section 6.1, the previous discussion leads to a key question: If the vortex generation instability is solely associated with shear, why aren't the large flanking vortices produced by the ejection event, but not by streamwise shear? There are two physical arguments that contradict this idea: First, the velocity difference of the wall-normal velocity v between sweep and ejection events is significantly smaller than the velocity difference between high- and low-momentum structures in streamwise direction. Therefore, it takes longer to generate large vortices from an initially small disturbance. The velocity difference, hence a measure for the shear, between a sweep and ejection is approximately $\Delta v \approx 0.04-0.1u_{\infty}$, while the difference in streamwise direction is $\Delta u \approx 0.2-0.3u_{\infty}$. The second argument is a mere time constraint. The ejection is naturally bound by the boundary-layer thickness, which might be pushed further out locally due to the ejection. Hence, the time to generate a vortex in wall-normal direction is small. Taking the average wall-normal velocity v of an ejection event conditioned according to the events in the beginning of this section at $y^{*}/\delta_{99} = 0.23$ as a reference, an ejection event lasts in maximum $0.03-0.04\,\mathrm{s}$, which equals approximately $12-17$ boundary layer turnovers at the highest Reynolds number $Re_{\tau} = 12000$. In contrast, the inclination of structures in streamwise direction is $7^{\circ}-15^{\circ}$ near the wall, increasing up to 45° in the outer boundary layer (Adrian et al., 2000; Buchmann et al., 2016). This provides more time for instability to develop larger vortices.

6.2.2. Vortex paths

In the previous section, the focus was on the size and distribution of vortices, to connect the self-sustaining process hypothesis with instantaneous and average flow fields. To understand the dynamics and the inclination with respect to the wall of large-scale structures, the path of the flanking vortices must be analysed. If the flanking vortices are regarded as potential vortices, their path can be analytically calculated. According to the law of Biot-Savart, a vortex induces a velocity field $u_{\Theta} = \frac{\Gamma}{4\pi r}$ based on its circulation Γ and the distance of the observation point r to the vortex centre. If only the two flanking vortices are considered, this would result in a pure upward motion of the vortices while convecting downstream with the flow. But due to the presence of the wall in a boundary layer, the mirrored vortices must be considered as well. The induced velocity field of the mirrored vortices leads to a decrease of the distance between vortex centres while moving away from the wall. A detailed mathematical description of the analytical path of potential vortices is discussed and calculated in appendix A.5. Assuming constant circulation and a decreasing vortex distance, the induced wall-normal velocity in between the flanking vortices is increasing with the wall distance and thereby the structure angle increases, as was also observed in previous studies (Adrian et al., 2000). It should be noted that this is an idealised point of view. Turbulence is chaotic, accordingly, it is highly unlikely to find two flanking vortices with identical circulation at a similar wall distance. This asymmetry leads to slanted vortex paths and structures in the boundary layer, as are observed in simulations and experiments.

The motion of vortex centres is reconstructed from the time-resolved SPIV data at $Re_{\tau} = 8400$ and plotted in figure 6.10 for a subvolume of the time-resolved SPIV data. The figure shows the wall-normal direction over a non-dimensional time t/τ_{δ}, with the boundary layer turnover time $\tau_{\delta} = \frac{\delta_{99}}{u_{\infty}}$. This representation is possible using Taylors hypothesis. The convection velocity was chosen to the free-stream velocity u_{∞}, which leads to an overestimation of the streamwise vortex centre position. Following the vortex path in figure 6.10, an average motion of the vortex cores away from the wall is present, which supports the afore mentioned analytical description.

From a structural standpoint, two effects must be differentiated. First, the path of the vortex as described above. The second effect is the impact of the vortices on the flow, which leads to a redistribution of fluid in spanwise direction, as discussed in section 4.1. Thereby, it is possible to observe an increase in streamwise large-scale structure sizes, calculated from two-point correlations, even if the induced velocity fields from the vortices is bringing the vortices closer together.

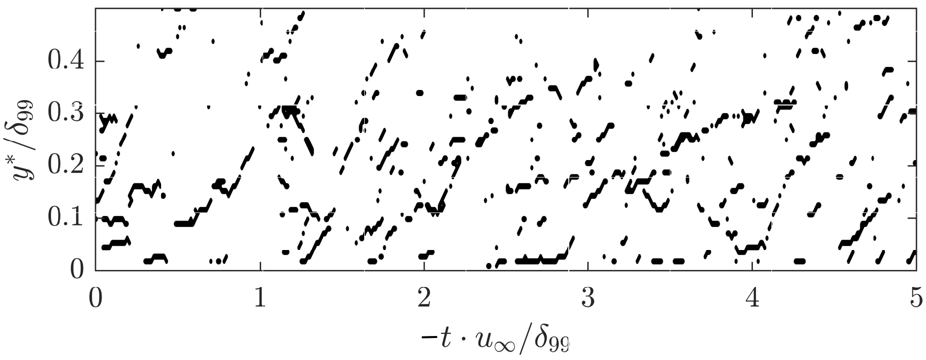

Figure 6.10: Detected vortex centres (•) from time-resolved data at $Re_\tau = 8400$.

6.3. Comparison with existing theories and models

One of the difficulties in turbulence research is the different interpretation of similar measurements, observations and data. This often leads to controversy and various explanations. In the following, the self-sustaining flanking vortex model (SSVM) will be discussed and reviewed in comparison to different existing structure origin and dynamic explanations from literature, namely the hairpin model (Head and Bandyopadhyay, 1981; Adrian et al., 2000), the attached eddy model (AEM) (Townsend, 1956), and the sweep-streak interaction (Hunt and Morrison, 2000). All concepts were introduced in section 2.2.

The principal difference is the question of primary structure. While the hairpin model takes hairpins or packages of hairpins as the primary structure, which induce low-momentum streaky fluid in their core region, the low-momentum regions are the secondary structures. In contrast, in the SSVM the longitudinal vortex, which redistributes the streamwise momentum, is the primary structure. Observed hairpins or small shear vortices flanking sweep and ejection events are the secondary structures created from local shear. In the sweep-streak interaction described by Hunt and Morrison (2000), a blockage due to a sweep event creates longitudinal vortices.

Therefore, the generation process described by Hunt and Morrison (2000) is driven by sweep events. All three models have in common that they rely on shear instabilities and the necessity of longitudinal vortices. In the hairpin model, streamwise vortices develop into horseshoe vortices which are stretched and bent, resulting in haripins with streamwise legs. In contrast, in the SSVM a wall-normal vortex is bent resulting in the streamwise vortex. One similarity between the static hairpin theory and the dynamic SSVM is the underlying bending and stretching process, which deforms existing vortices in a manner that generates the longitudinal vortex.

In contrast to the three other models, the AEM was originally set up to describe scaling and statistics in a turbulent boundary layer flow. It doesn't include dynamics at all in its original formulation. Recent improvements are set up to include dynamic aspects (Kevin et al., 2019; Marusic and Monty, 2019). The AEM and the hairpin model have in common that they rely on deterministic, hierarchical vortex structures. In contrast, the explanations based on shear instabilities do not need any structural hierarchies and orders, which makes them more likely in a chaotic process. Another argument against the presence of closed vortex loops results from physics. If one considers the vortices as connected in a cane/ hairpin shape, the vortex loops would reach up to the outer edge of the boundary layer in maximum. Reuther and Kähler (2018) have shown that the pure turbulent fluctuation decreases in the outer boundary layer. Accordingly, the rotation must decrease significantly at the head of the hairpin, which is only true for a constant circulation if the vortex diameter increases. Such an increase of vortex diameters in the outer boundary layer has not been observed before in studies or literature.

All models have their individual advantages, disadvantages and potential. The AEM is a very simplified, straight forward concept focusing on statistics. The hairpin model describes the large-scale structures as a consequence of a hierarchical structure order and a regeneration process. The sweep-streak interaction and SSVM focus on the dynamics in the turbulent boundary layer flow. Both models have no need for a structural order, specific structure size and shape, and are therefore independent in their conception of the Reynolds number. In the AEM and hairpin model, the structures' sizes are dependant on wall distance and Reynolds number.

Finally, it must be stated that no model gives a total insight and generally agreed on conception. Models must be taken and understood as what they are: Simplified concepts which help to understand the complex turbulent flow and thereby improve our understanding for the physics. That's why they are necessary and valuable.

7

On the impact of an adverse pressure gradient on large-scale structures

Most technical and environmental flows are not canonical ZPG turbulent flows, but are subject to pressure gradients. In the classic aerodynamic example, the flow over a wing, the boundary layer on the suction side is exposed to both a favourable and an adverse pressure gradient. In particular the case of an adverse pressure gradient turbulent boundary-layer flow is of scientific interest as the APG fans the turbulence (Skåre and Krogstad, 1994). Hence, it is important to understand the behaviour of the large-scale structures under the impact of an APG, as large-scale structures are a dominant flow feature in a turbulent boundary-layer flow. Therefore, the topology of an attached turbulent boundary layer under an APG is discussed in section 7.1, focusing on large-scale structure scaling.

When the pressure gradient is further increased the boundary-layer flow separates. As large-scale structures are associated with a large amount of turbulent kinetic energy, it is of interest to examine how the separation itself is affected by the presence of large-scale structures in the flow and how the large-scale structures behave while interacting with the separated region. Therefore, a separated turbulent boundary-layer flow is analysed in section 7.2.

To simplify the comparison of the figures and analysis, the reference position x_0 is similar for all plots, namely the location of the central SPIV measurement over model 2, as given in table 3.3. Thereby, all measurements have the same coordinate system x^*, y^*, z^* in the APG of model 2. The results, discussions and conclusions in the following chapter are partly taken from the publications of Eich and Kähler (2017), Eich and Kähler (2019) and Eich and Kähler (2020) with permisson from Elsevier Ltd..

7.1. Structural pattern of an attached adverse pressure gradient turbulent boundary-layer flow

In this section the analysis is limited to the structural pattern within the turbulent boundary-layer flow. Characterisation of the attached adverse-pressure gradient turbulent boundary-layer flow in terms of mean flow parameters, boundary-layer thickness and modelling can be found in Reuther et al. (2015); Reuther and Kähler (2018) and Knopp et al. (2018).

The most direct and intuitive way to get a structure topology comparison between a ZPG and APG turbulent boundary-layer flow is the visual inspection of instantaneous flow fields in wall-parallel planes, comparable to the flow fields presented in section 4.1. In figure 7.1, the spatial distribution of instantaneous, normalised velocity fluctuations $u'/\overline{u}$ in streamwise direction are plotted for a ZPG and an attached APG turbulent boundary-layer flow in a

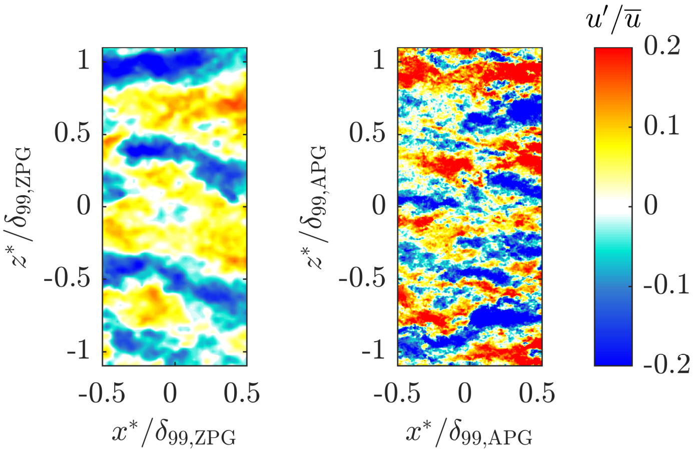

Figure 7.1: Velocity fluctuations $u'/\overline{u}$ in wall parallel planes at $y^*/\delta_{99} = 0.07$ under ZPG (left) and APG (right).

wall-parallel x^*z^*-plane at $y^*/\delta_{99} = 0.07$. Large elongated structures with positive (red) and negative (blue) momentum relative to the mean motion are found in both measurements. In the spanwise direction the structures align in a streaky topology side by side for both fields, which is in accordance with the previous findings discussed in chapter 4 and results from Harun et al. (2013). Due to the lower spatial resolution by a factor of $M = 2.6$ of the ZPG measurements, the ZPG flow fields appear smooth in comparison to the APG flow fields. Observing the same structural pattern under ZPG as well as APG flow conditions shows that large-scale structures are also dominant and a persistent flow feature under APG flow conditions. This raises multiple questions: Are the observed structures the same as observed in the ZPG boundary-layer flow? Are the structures newly generated in the APG boundary layer with a similar cyclic process as discussed in chapter 6, or are the structures convecting with the mean flow into the APG section of the boundary layer model? Theses questions will be addressed in the following, to the extent possible with planar PIV measurements.

Comparing the relative fluctuations in the two flow fields in figure 7.1, the fluctuations measured under an APG are higher on average, which confirms the increase in turbulent kinetic energy under an APG (Harun et al., 2013). It should be noted that observing a wall-parallel plane is not an observation at a constant relative wall distance y^*/δ_{99} in the APG case, as the increase in boundary-layer thickness is significantly large under APG impact. The given number is calculated in the centre of the image. For the ZPG case the increase of the boundary-layer thickness is $< 0.3\,\%$ of δ_{99} within the cropped field of view of $1 \times 2.1\,\delta_{99}$ in figure 7.1. Hence, the plane can be considered as wall parallel also in a relative sense. The decrease of relative wall distance for the APG flow field in combination with an overall decreasing mean velocity under an APG impact explains the marginal increase of relative fluctuations from upstream to downstream in the measured flow field. But even if the scaling and observation effects are taken into account, the turbulent intensity under the APG influence is increased, which again highlights that the turbulence under the APG is fanned (Skåre and Krogstad, 1994). For the structural analysis and discussion, this has two consequences: First, a convecting structure with a specific amount of streamwise momentum and turbulent kinetic energy results automatically in increased fluctuations when the structure is subjected to an overall mean flow deceleration. Second, the effect of the APG impact is not equally strong depending on the structure momentum.

To examine the corresponding structural scales, the flow fields under APG impact were analysed by spatial two-point correlations. In figure 7.2 the resulting spatial scales in the

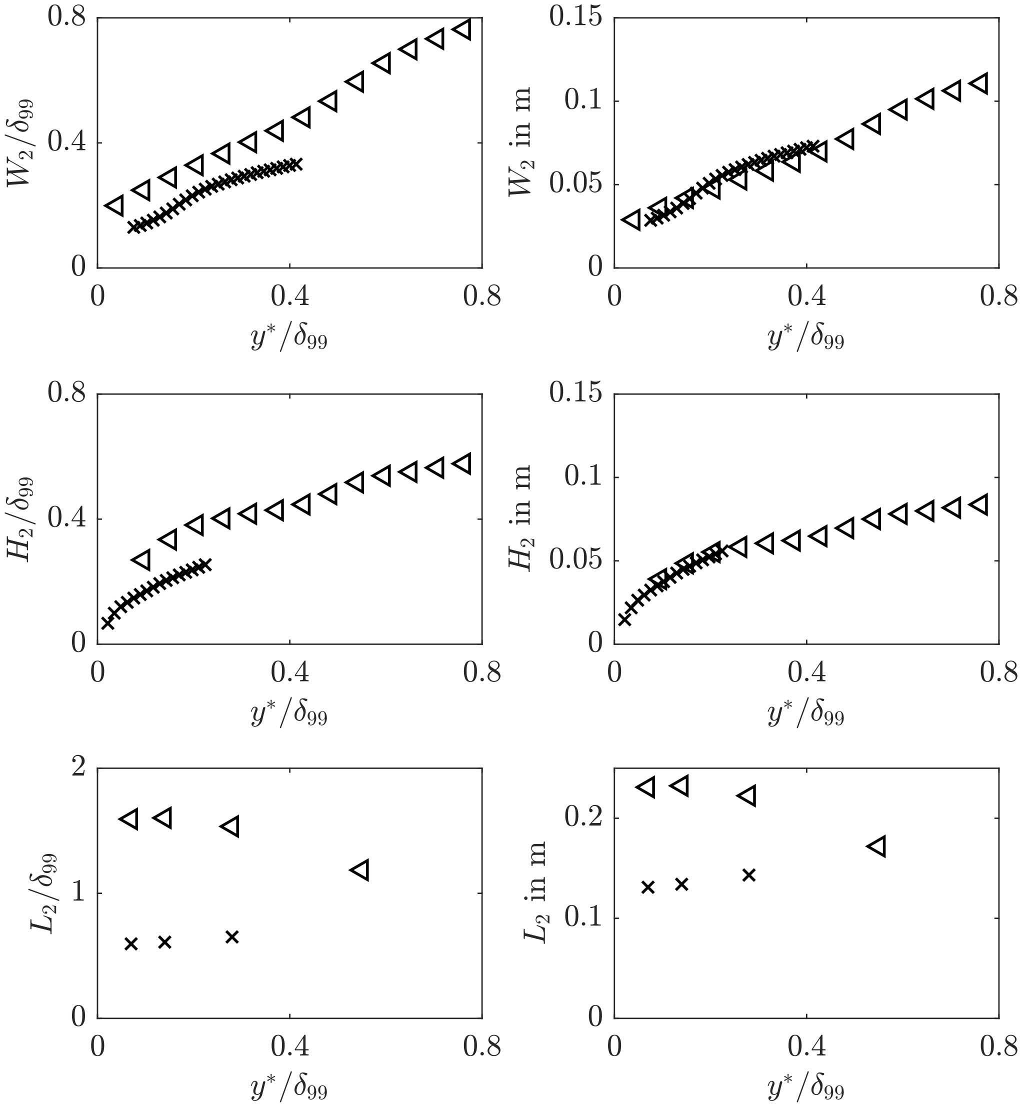

Figure 7.2: Comparison of structure width W_2, height H_2 and length L_2 under APG ($\times$) and ZPG ($\triangleleft$). Left column: Spatial scales normalised with the local boundary-layer thickness δ_{99}. Right column: Raw, unscaled results.

cut plane are plotted. The left column shows the spatial scales normalised with the local boundary-layer thickness. This is the commonly applied scaling for large-scale structures in a TBL flow (Hutchins and Marusic, 2007a; Maciel et al., 2018; Marusic et al., 2010). The increase in boundary-layer thickness due to the APG impact is about 50 % based on the ZPG boundary-layer thickness (Reuther et al., 2015). Therefore, all scales are expected to be shorter for the APG case when normalised with the local boundary-layer thickness. This is the case, as seen in the left column of figure 7.2. To distinguish between changes in the structure pattern and normalisation influence, the raw scales, in the following denoted as absolute scale, are plotted in the right column in figure 7.2. The absolute width is smaller below $y^*/\delta_{99,\mathrm{APG}} = 0.18$ and larger above. In contrast the height of the structures is identical for the ZPG and APG case. The length of a structure is significantly reduced under the APG impact.

Combining these scaling trends and observations from the instantaneous image it can be assumed that structures survive the APG impact and are modulated by the APG. The APG acts as a resistance to the flow, which is shortening the flow structures and forcing fluid motion in spanwise direction. This explains the increase in width in the outer boundary layer. The wall-normal direction is unaffected by the APG. Following this line of thought, the structures are convecting from the ZPG section, at least in the outer boundary layer. A different explanation can be given based on the turbulence theory and previous studies, which is discussed in the literature survey in section 2.2.3. The main production of turbulence is shifted away from the wall under APG impact (Skåre and Krogstad, 1994; Vinuesa et al., 2017). Also the main shear is not present at the wall but away from the wall the stronger the APG is. Hence, an APG turbulent boundary-layer flow has increasing similarity with free shear flows as the APG increases (Kitsios et al., 2017). This means that similar structures as under ZPG influence are generated under the APG impact but further away from the wall, if a shear driven process, as the mechanism proposed in chapter 6, is the structure generation mechanism. Supporting this theory is that a self-sustaining process based on shear instabilities needs strong shear in the flow, which is not present close to the wall in strong APG turbulent boundary-layer flows. Unfortunately, due to the limited optical access in the model 1 APG section, no SPIV data is captured beyond $y^*/\delta_{99,\mathrm{APG}} = 0.4$, therefore this conclusion is drawn on data limited to the inner region of a turbulent boundary-layer flow.

7.2. Analysis of a turbulent boundary-layer flow up to flow separation

While in the previous section 7.1 an attached APG turbulent boundary-layer flow was analysed, the following investigation focuses on a turbulent boundary-layer flow under APG impact up to flow separation. Therefore, the unsteady flow separation is quantified in a first step in section 7.2.1. Afterwards the effect of the unsteady flow separation on the mean flow parameters is described in section 7.2.2. As this thesis focuses on large-scale coherent structures in boundary layers, the structural pattern is discussed in section 7.2.3, to finally investigate the interaction between large-scale structures and the flow separation in subsection 7.2.4.

7.2.1. Characterisation of the unsteady flow separation

In order to characterise and quantify the effect of large-scale structures on the flow separation and vice versa, it is necessary to quantify the unsteadiness of the separation itself and the effect of the separation dynamics on characteristic boundary-layer parameters. In figure 7.3 a cumulative distribution function $\mathcal{P}$ of the separation location $x^*_{u<0}$ is shown. The separation location is defined as the most upstream position at the wall of the first area with negative flow velocity, which includes more than 150 vectors in the x^*y^*-plane. This enables a robust instantaneous detection, because the common approach for separation detection via the wall-normal velocity gradient is uncertain within the PIV fields due to the limited spatial resolution and measurement uncertainty near the wall, where particle image displacements are very small. The number of $N = 150$ connected vectors is chosen based on the observations in instantaneous flow fields, where small prior separations occur before the flow is completely separated (Bross et al., 2019). Sensitivity analysis of the chosen threshold number N showed no changes in the qualitative observations and conclusion, only the abso-

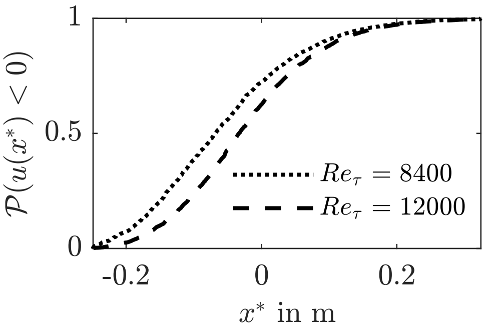

Figure 7.3: Cumulative distribution function $\mathcal{P}(u(x^*) < 0)$ of the instantaneous separation start position for two different Reynolds numbers.

lute separation location changes. The cumulative distribution function $\mathcal{P}$ in figure 7.3 can be therefore interpreted as the average fraction of time for which one specific position x^* is separated in the wall-normal x^*y^* plane. A detailed discussion and sensitivity analysis of the detection criteria is given in appendix A.6.

The results displayed in figure 7.3 show that the separation location is strongly unsteady over a streamwise length of approximately $2\,\delta_{99}$. Furthermore, clear influence of the Reynolds number is detectable. The higher the Reynolds number and thereby the free-stream velocity and mean streamwise momentum, the later the flow separates. The streamwise domain where the unsteadiness of the separation takes places shrinks with the Reynolds number. This is a direct consequence of the model 2 design. In contrast to an infinite flat plate turbulent boundary layer experiment, model 2 ends in a sharp corner at $x = 0$. Purpose of the sharp corner is to stabilise the separation bubble. The definite end of model 2 results in a streamwise shortened separation bubble with increasing Reynolds numbers as the extent in downstream direction is bound. In other cases it might be that the separated region is shifted downstream as a whole and not compressed as in the case were the geometry fixes the separation location. A second physical reason is the pressure recovery of the flow. The longer the flow can withstand the APG, the smaller is the pressure difference between the separation and the wind tunnel core flow behind the model, hence the separated region shrinks.

7.2.2. Conditional analysis of the boundary layer parameters

Depending on the location of the flow separation in the instantaneous flow field the data is conditioned into five quantiles. Thereby it is possible to analyse the effect of the separation location on the mean flow parameters. Quantile one represents the most upstream separation locations, continuing downstream. While no effect on the boundary-layer thickness δ_{99} is present, a clear influence on various boundary layer parameters such as the shape factor H, displacement thickness δ^* and the momentum thickness θ was detected, as shown in figure 7.4 for quintiles 1, 3, 5 and the complete data set. The mean flow parameters give insight in the state of the flow, e.g. laminar, turbulent or separated, and if acceleration, deceleration or some deviation from the canonical case occurs. For details see the discussion in section 2.1.1 and the text book of Schlichting and Gersten (2006).

The later the separation occurs, the smaller the momentum and displacement thicknesses become. The shape factor H is increasing from $H = 1.9$ at the upstream end of the field of view to $H \approx 4$ at the downstream end where the flow is separated, as is expected for an increased APG (Maciel et al., 2017). In comparison the shape factor is $H = 1.4$ for a ZPG TBL flow. The higher shape factor indicates that the mean profile is subject to increasing deceleration near the wall. A point of inflection in the mean profile is present, hence the

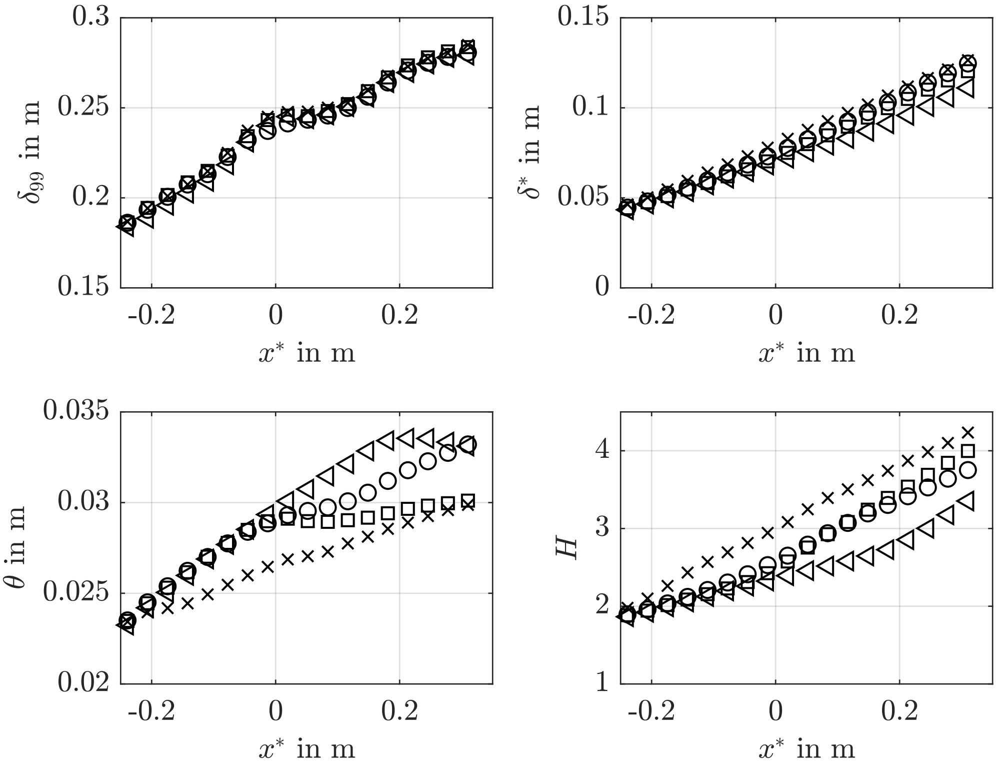

Figure 7.4: Conditional analysis of the mean boundary layer parameters δ_{99}; δ^*; θ and H at $Re_{\tau,\text{ZPG}} = 12000$ form the APG x^*y^* measurements over model 2. Symbols correspond to different start locations of the flow separation. ○ : unconditioned data; × : first quintile; □ : third quintile and ◁ : fifth quintile.

boundary-layer flow is unstable. Also a characteristic change of slope of the shape factor occurs near the average separation location of the analysed quintile, hence the shape factor can also be used as a detection criterion for the separation location.

The change in shape factor, while the mean boundary-layer thickness δ_{99} is unaffected, shows that the effect of the flow separation and the position of the separation line mainly affects the inner boundary layer. As discussed in chapter 4 and section 7.1 this is the region where high energetic turbulent structures exist. Therefore, in the following the structural pattern with the presence of flow separation will be investigated.

7.2.3. Analysis of the structural pattern

The structural pattern in the vicinity of the separation line is strongly dependant on the instantaneous separation line and the spatial extent of the separation bubble. In figure 7.5 the normalised velocity field u/u_∞ and fluctuation field u'/u_∞ in a streamwise wall-normal x^*y^*-plane is plotted. The velocity u_∞ corresponds to the free-stream velocity over the ZPG section of model 2, because defining one free-stream reference velocity in a decelerating flow is not possible. To highlight the separation bubble, the black line encloses the areas with flow velocity $u < 1\,\text{m/s}$. A small pre-separated area occurs right in front of the big separation bubble, where the flow completely separates. The separation extends in wall-normal direction up to $y/\delta_{99} = 0.3$. Multiple layers with uniform velocity inclined to the wall can be found in the velocity field. Investigating the fluctuation field, an overall similar pattern is present

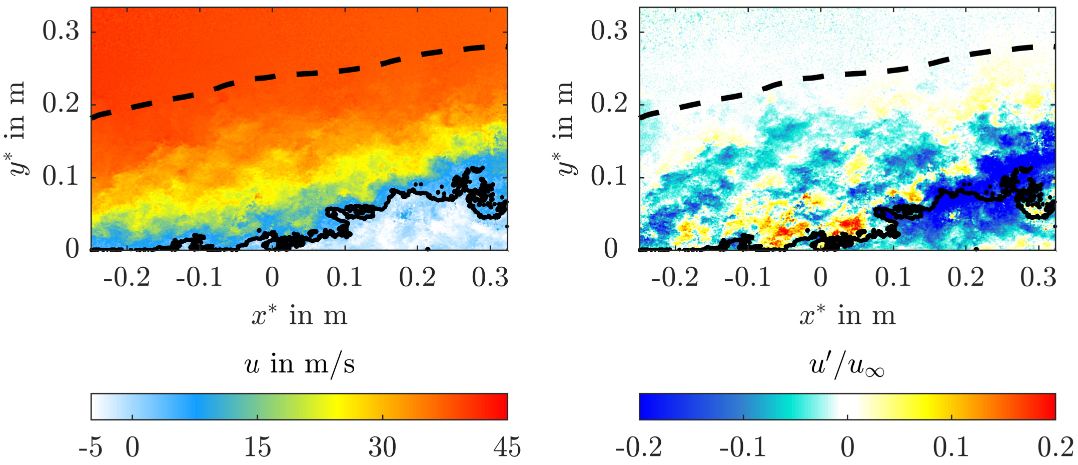

Figure 7.5: Normalised velocity field u/u_∞ (left) and fluctuation field u'/u_∞ (right) in a streamwise wall-normal x^*y^*-plane unter APG impact at Re_τ, ZPG $= 12000$. The dashed line corresponds to the average boundary-layer thickness δ_{99}.

with high and low-momentum fluid. At the far downstream position, a large low-momentum field with fluctuations around $u'/u_\infty \approx -0.2$ is visible, which might also be separated but still has a higher streamwise velocity than $u < 1\,\mathrm{m/s}$. This yields that the separation bubble is most likely underestimated when only considering reverse flow vectors or vectors below a certain low threshold velocity such as $u = 1\,\mathrm{m/s}$. On the other hand, it is impossible to define a threshold for the whole field which is enclosing the separation bubble correctly, because this threshold must be wall distance dependant. Furthermore, such a threshold must also be dependant on the streamwise position as the mean flow velocity decreases in downstream direction due to the APG.

To examine the underlying structural pattern, the flow fields in the APG close to the separation were analysed by means of two-point correlations. In figure 7.6 exemplary correlation functions are shown for the APG flow at $Re_{\tau,\mathrm{ZPG}} = 12000$ for three different wall-normal positions and two streamwise positions. The red correlation functions are close to the edge of the boundary layer, the blue correlation functions are within the large-scale structure dominated region and the black correlation functions are in the vicinity of the separated region. The shape of the positive correlated region outside the separated region is qualitatively similar to ZPG flow (Buchmann et al., 2016; Kitsios et al., 2017). Characteristic is the elongated shape in streamwise direction inclined to the wall. The shape of the correlation function is mainly dependent on the wall-normal location.

While the correlation functions close to the edge of the boundary layer reveal a round shape as a result of intermittency effects (Reuther and Kähler, 2019), the blue correlation functions are elongated in streamwise direction due to the presence of large-scale structures. The black correlation is dominated by the separation. Clearly visible is the change between the correlation at $x^* = -0.18\,\mathrm{m}$ upstream of the separated region and $x^* = 0.1\,\mathrm{m}$ within the separated region.

Based on the correlation functions, characteristic values can be calculated, such as the length L_2 in a cut plane of the correlation function and the angle α relative to the wall. The resulting scales are plotted in figure 7.7. The length scale L_2 is calculated using a threshold for the correlation of the streamwise fluctuation of $R_{u'u'} = 0.3$. The correlated length at a

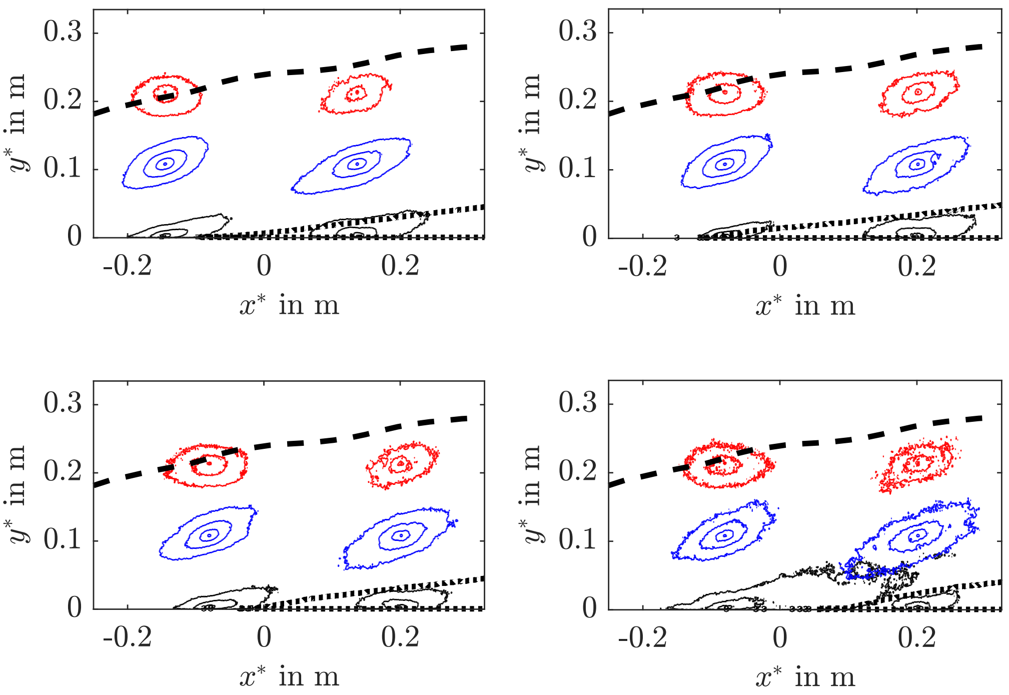

Figure 7.6: Two-point correlation function $R_{u'u'}$ at three different wall-normal locations and two streamwise positions. Contour lines are drawn at $R_{u'u'} = 0.3$, 0.5, 0.7 and 0.9. The dashed line (− −) corresponds to the average boundary-layer thickness δ_{99}, the dotted line (··) to the average separated region. Top left: All data. Top right: Quintile 2. Bottom left: Quintile 3. Bottom right: Quintile 4.

comparable ZPG position is $L_{2,\mathrm{ZPG}} = 1.9\,\delta_{99}$ at $y^*/\delta_{99} = 0.14$. The scales are normalised with the ZPG boundary-layer thickness $\delta_{99,\mathrm{ZPG}}$ to have a similar scaling of all positions within the field of view and flow cases. The high value of $R_{u'u'} = 0.3$ as selected threshold is necessary to ensure that the correlation function is within the field of view for the chosen value to calculate the length scales over the whole field of view. The correlated structure length in the outer APG boundary layer is $L_2 \approx 1.1\,\delta_{99,\mathrm{ZPG}}$, hence approximately 40 % shorter than in the ZPG case. This effect is a result of the impact of the APG, which shortens the structures due to the deceleration of the flow in this region, as discussed in section 7.1 and in PIV and hot-wire experiments in literature (Harun et al., 2013; Hain et al., 2016).

In the vicinity of the separated region the correlated length scales increase. Two different effects must be considered as causes: First, the separated region is highly unsteady due to the action of the large-scale structures, hence its spatial extent is in multiple fields larger than on average. As the fluctuation signal in the separated region is similar compared to the flow outside the separation, the separated region correlates positive, which biases the calculated spatial scales of the turbulent structures. This explains the dark red area in figure 7.7 (left) with length scales of $L_2 = 1.5\,\delta_{99,\mathrm{ZPG}}$. The second effect is the increase of length above the separated region, which can be interpreted as a stretching of large-scale structures when convecting directly over an obstacle like a separation due to the displacement of the non-separated flow region. Further, the pressure gradient in streamwise direction is decreasing in the vicinity of the separation bubble which leads to a smaller resistance for the structures.

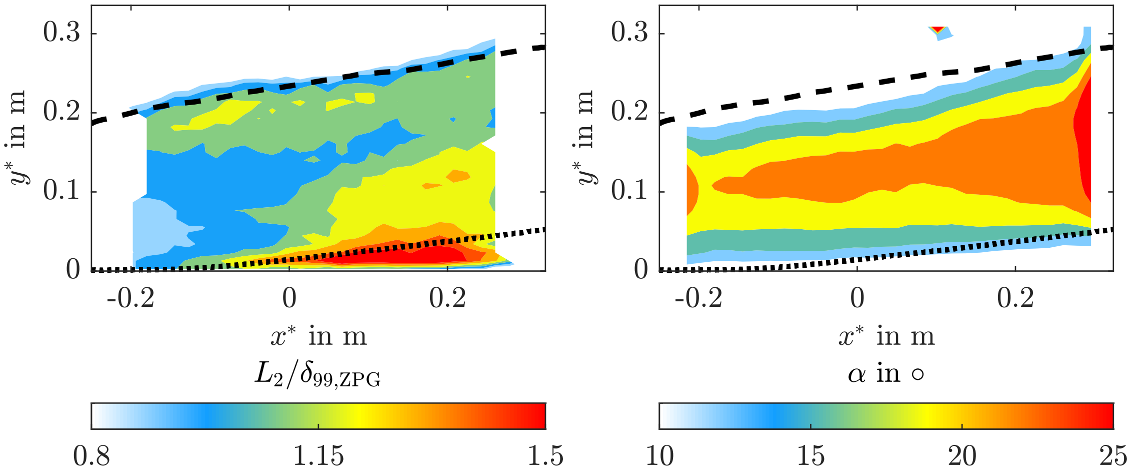

Figure 7.7: Evolution of the structure length L_2 (left) and structure angle α (right) under APG conditions calculated from two-point correlation functions at $Re_{\tau,\mathrm{ZPG}} = 8400$. Dashed line (− −) corresponds to the average boundary-layer thickness δ_{99}, the dotted line (··) to the average separated region.

Also significant is the change in the angle of the correlated structures relative to the wall, as shown in figure 7.7 (right). The angle was calculated based on the $R_{u'u'} = 0.3$ correlation line. For this purpose, an ellipse was fitted into the correlation of $R_{u'u'} = 0.3$ and the angle of the semi-major axis was calculated as the representative angle of the structures. While for ZPG flow characteristic angles of $\alpha \approx 7^\circ - 15^\circ$ are observed depending on the wall position y (Adrian et al., 2000; Buchmann et al., 2016), this angle is increased up to $\alpha > 20^\circ$ due to the APG and beginning flow separation. Kitsios et al. (2017) made comparable observations in a direct numerical simulation at smaller Reynolds numbers. They observed an increase from $\alpha = 7^\circ$ under ZPG to $\alpha = 27^\circ$ for strong APG conditions. When a flow separation occurs, further effects must be considered. The flow separation forces a displacement of the streamlines away from the wall and increases thereby the angle of the mean flow relative to the wall, which is on average transferred to the structures in the flow. As the angle of the structures is defined relative to the wall, the angle increases in the vicinity of the separation due to the displacement of the mean streamlines, which does not necessarily imply a change of structure angle relative to the flow.

Besides the scaling of the structures in streamwise direction, the spanwise pattern is analysed. As shown in figure 7.1 a characteristic intermittent pattern of high and low-momentum structures is present in ZPG as well as APG. To assess the structural pattern characteristics quantitatively, the spacing Λ_2 in a wall-parallel cut plane is calculated from two-point correlations in spanwise direction. Therefore, the instantaneous two-point correlation for one point of one statistical independent image is calculated and ensemble averaged for all images, which results in the characteristic two-point correlation function in spanwise direction (Hutchins and Marusic, 2007b). The structure spacing Λ_2 is defined as the distance between the two flanking minima. The calculation of the structure spacing is independent of chosen thresholds and yields therefore a robust criterion for coherent structure analysis. The resulting spacings are plotted in figure 7.8.

In contrast to the instantaneous flow fields in figure 7.1, all spacings in this figure are normalised with the same reference value, namely the boundary layer thickness $\delta_{99,\mathrm{ZPG}}$ at

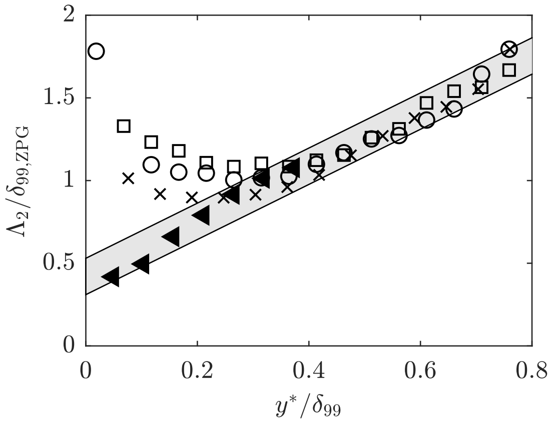

Figure 7.8: Spanwise spacing Λ_2 of large-scale structures under APG with flow separation. The filled symbols (◀) represent the reference case without flow separation at $Re_{\tau,\mathrm{ZPG}} = 9300$ over model 1. The other symbols correspond to different streamwise positions of the measurement at $Re_{\tau,\mathrm{ZPG}} = 12000$ at model 2. $\times$: $x^* = -0.18\,\mathrm{m}$; $\circ$: $x^* = 0\,\mathrm{m}$ and □ : $x_0 = 0.18\,\mathrm{m}$.

the corresponding ZPG position $x_{0,\mathrm{ZPG}}$. The wall distances are scaled with the local boundary layer thickness at the point of interest. Thereby, it is possible to quantify the modulation influence of the pressure gradient on the structure spacing at a specific relative wall distance, without the bias through scaling effects, e.g. the increase in boundary layer thickness δ_{99} from ZPG to APG. In the near wall region, $y/\delta_{99} < 0.3$, the structure spacings in the partly separated flow are significantly larger compared to the attached flow state case. This effect will be discussed in more detail in the following sections. Further away from the wall, the spanwise spacing scaling is identical for the attached APG and ZPG reference data. All data collapse in the shaded grey corridor. Those results are in line with the previous observations that the separated region mainly effects the flow in its close proximity, but large-scale structures, as energetic features, are persistent and keep their spanwise extension and structural pattern. The large-scale structures seem to convect over the separation bubble.

7.2.4. Interaction between large-scale structures and flow separation

Besides the average parameters of the TBL, the interaction between the flow separation, the velocity field and turbulent structures is evaluated. In figure 7.9 the difference between conditioned mean velocities of quintiles 1 (left) and 5 (right), $\langle u_i \rangle$, and the overall mean $\overline{u}$ is plotted. On average the flow velocity is lower for the further upstream separation location, while for the downstream separation location the opposite is the case. The dotted line marks the corresponding ensemble average of the separated region of the plotted quintile. These dynamics of the separated region can be explained with the impact of large-scale structures on the separation itself, as qualitatively shown in the sketch in figure 7.10. High-momentum large-scale structures push the separation line downstream, whereas low momentums large-scale structures favour flow separation. This is possible because the turbulent large-scale structures alter the flow dynamics down to the wall (Bross et al., 2019).

The dashed line in figure 7.9 shows the mean boundary layer thickness δ_{99} calculated for quintiles 1 and 5. The quintiles chosen for the plot refer to the separation position as explained in 7.2.2. As stated before, no differences are found for the five investigated separation locations. This observation is in accordance with the displayed differences of the

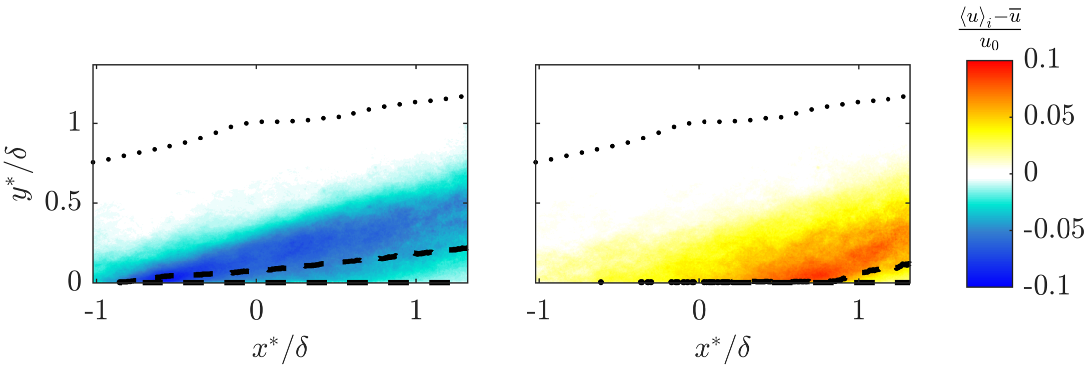

Figure 7.9: Conditioned streamwise mean velocity $\langle u_i\rangle$ in comparison to the average mean velocity field $\overline{u}$ at $Re_\tau = 12000$. Left: Upstream flow separation location (quintile 1). Right: Downstream flow separation location (quintile 5). Dotted line (··) corresponds to the average boundary-layer thickness δ_{99}, the dashed line (– –) to the average separated region.

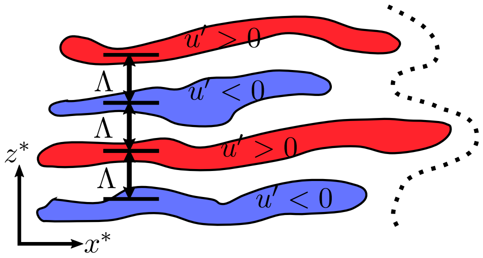

Figure 7.10: Sketch of the large-scale structure impact on the position of the separation line (–).

mean velocity. The faster and slower mean velocities only extend up to $y^*/\delta_{99} \approx 0.6$ in maximum, hence the outer boundary-layer flow is unaffected by the unsteady separation. This highlights that the interaction between flow and separation only takes place in the inner boundary layer where large-scale structures are present. Furthermore, this proves that the unsteadiness is not an effect of changes of the wind tunnel inflow velocity, because this would also effect the outer boundary layer, but an effect of turbulent large-scale structures.

7.2.5. Spectral analysis

If the large-scale motions modulate the separation line locally, the spanwise modulation of the line of separation must be as well largely governed by the spanwise spacing of the large-scale motions and their temporal dynamics. In figure 7.11 the spanwise pre-multiplied energy spectra of ϕ_{uu} is plotted. For the flow cases with separation and the ZPG reference case, an estimated peak occurs around $\lambda_z/\delta_{99} \approx 0.95$, which is the same value as the structure spacing Λ_2 calculated from two-point correlations and shown in figure 7.8. With increasing downstream position in the APG cases, the peak in the energy spectra raises in amplitude and broadens. Larger wavelengths, which correspond to the separated part are more likely present. Observing the maximum energy at a characteristic wavelength, which is equal to the structure spacing shown in figure 7.8, give further support for the assumption that the separation line dynamics are strongly modulated by the large-scale motions.

The strong increase of the peak value compared to attached ZPG and APG flows (Harun et al., 2013) is a direct consequence of the presence of the flow separation. The mean flow velocity value for a partly separated flow is in between the average attached and separated

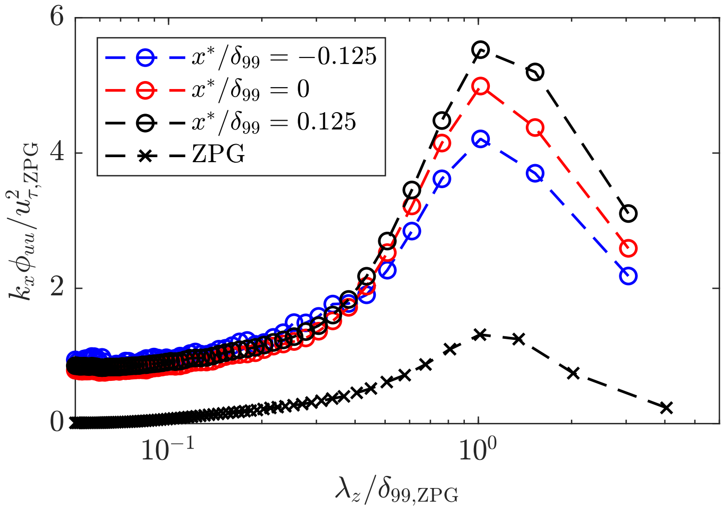

Figure 7.11: Spanwise pre-multiplied energy spectra $k_x\phi_{uu}/u^2_{\tau_{\mathrm{ZPG}}}$ at a wall distance $y/\delta_{99} = 0.3$. ○ symbols correspond to three streamwise position in the model 2 APG section at $Re_{\tau,\mathrm{ZPG}} = 8400$. × symbols correspond to a ZPG reference case at $Re_{\tau,\mathrm{ZPG}} = 9300$.

flow velocities. Accordingly, the attached flow results in strong positive fluctuations while the separation results in strong negative fluctuations when the Reynolds decomposition is applied. As the peak of the spectrum is the wavelength which covers the spanwise intermittent separated/non-separated pattern, the decomposition results in very high fluctuation amplitudes and thereby a growing peak value.

8

Volumetric data - an outlook to future possibilities

The results discussed in all previous chapters 4, 6 and 7 are based on planar, two-dimensional data of the flow fields. In contrast a turbulent boundary layer flow and the large-scale structures, which populate the boundary layer, are highly three-dimensional. To fully understand their dynamics and interaction, volumetric data is indispensable. Therefore, a time resolved, volumetric measurement was performed in cooperation with the DLR Göttingen at the AWM in Munich. Using 13 high speed cameras a flow field of $2.9 \times 0.6 \times 0.15\,\mathrm{m}^3$ was captured. In this chapter, preliminary results from this campaign are presented as an outlook to future possibilities in boundary layer research. Therefore, the unique set-up is described in section 8.1, tracked flow fields and first results will be presented in section 8.2.

One particular issue capturing volumetric data is the trade-off between particle density to be able to track the particles on the one hand and sufficient spatial resolution on the other hand, to allow a physical analysis of the data sets afterwards. The data acquired during this campaign were analysed with the "Shake the Box (STB)" particle tracking algorithm from the DLR, which is intentionally designed to measure densely seeded flow fields by utilising the time information as a predictor for the particle positions. Thereby, both conflicting restraints for the measurement could be fulfilled adequately.

8.1. Measurement set-up

The three-dimensional volumetric measurements were preformed over the VicToria boundary layer model in the Atmospheric Wind Tunnel Munich. Details on the model and wind tunnel are given in chapter 3. To capture a volume in a time resolved manner, multiple high speed cameras are necessary. As a large volume in streamwise direction is crucial for the investigation of large-scale structures, three tomographic systems, consisting of four or five high-speed cameras respectively, were set up side by side. To provide an impression on the set-up, two photographs and a sketch of the camera positions with respect to the boundary layer model are shown in figure 8.1.

To distinguish between the three camera systems, the systems are labelled A, B and C in streamwise direction and are colour coded. In table 8.1 details of the camera systems, field of view and resolution are given. Due to the stitching of the three systems and the necessary overlap region, the whole field of view is smaller than the sum of fields of view of the individual systems. System A has in addition to the four Veo4K 990 cameras an IX iSpeed726 camera installed at the beginning to support the initial detection of the particle tracks by providing redundant information. All cameras were placed in an in-line configuration instead of a classic trapezoid tomographic PIV set-up. One camera of each system was placed perpendicular to the boundary layer model and therefore the measurement volume, the other three cameras were placed at an angle. The advantage of the in line configuration is that bright glare points in the images due to different scattering behaviour can be reduced. Disadvantage is a higher uncertainty in the spanwise component due to similar camera angles in respect to the x direction (Raffel et al., 2018).

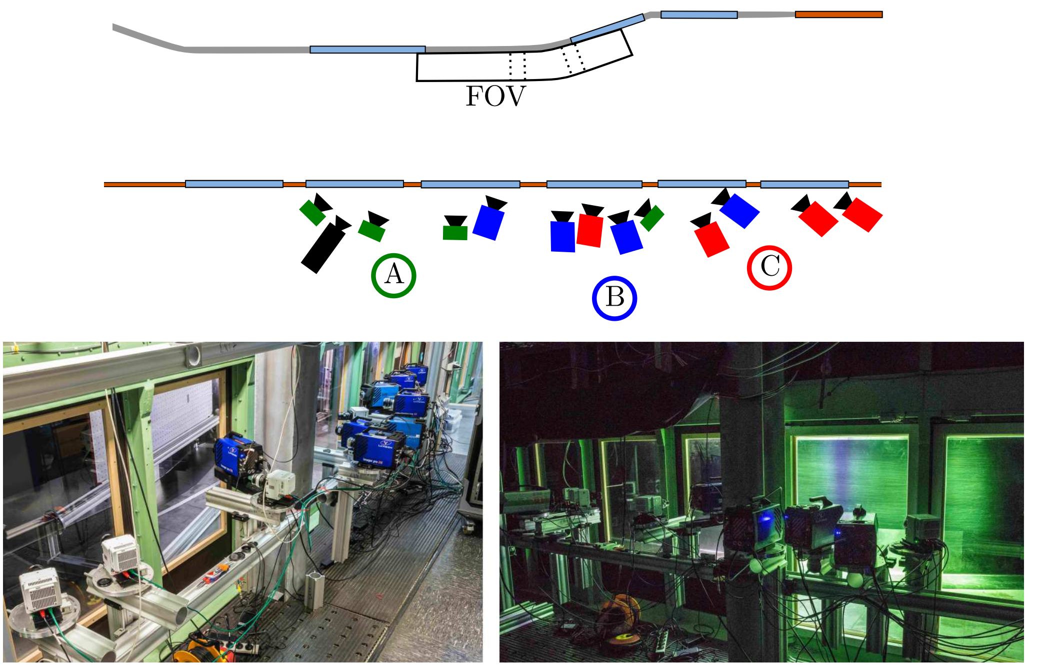

Figure 8.1: Camera set-up of the volumetric measurement. Top: Schema of the camera systems position at the wind tunnel with resulting field of view over the model. Green: System A, blue: System B, red: System C and the IX iSpeed 762 camera (black). Bottom left: Downstream view of the systems. In the tunnel the calibration plate is installed. Bottom right: Upstream view of systems A and B during a run. The green LED illumination and tracer particles are visible in the wind tunnel.

The camera system was calibrated with a printed 2D $2.5 \times 1.5\,\mathrm{m}^2$ target. Using no multi-plane target, it was necessary to shift the target within the wind tunnel to capture two planes with different wall distances with respect to the straight wall over the ZPG section of the model. The curvature of the model is not accounted for in the calibration process as a planar target was used, but the calibration function is extrapolated in the APG section and corrected via self-calibration. Details on the calibration procedure can be found in Schanz et al. (2019).

The volumetric illumination was provided by 9 high power LED arrays, each consisting of 75 single LEDs and 3 smaller arrays with 45 LEDs each. The arrays are specially designed for experimental fluid mechanic measurements and can be pulsed in a frequency range between $30\,\mathrm{Hz} - 100\,\mathrm{kHz}$ with a maximal radiometric flux of 450 W. For the measurements, a recording frequency of 1000 Hz was chosen for the cameras and the illumination was set on 2000 Hz, which is the double recording frequency. Therefore, all images are double illuminated. This improves the accuracy of the fitted particle tracks as more interpolation points can be used. The exposure time was set so $30\,\mu\mathrm{s}$ to avoid streaky particles.

As the volumetric illumination from the LEDs is less energetic per measurement volume than from pulsed Nd:YAG lasers utilised for PIV, larger particles with better light scattering characteristics must be used. In this set-up, Helium Filled Soap Bubbles (HFSB) were chosen as tracer particles. The HFSB are generated by individual nozzles run by two LaVision seeding generators, one placed in the inlet tower (200 nozzles) to provide a global seeding and one smaller generator (50 nozzles) placed in the local seeding box, which is described and tested for DEHS in section 3.5.1. Each nozzle can provide up to 40000 HSFB per second, resulting in a maximum of 10^6 tracer particles per second. Details on the generation and characteristics of HFSB are given in Bosbach et al. (2009). As HFSB implode in contact with solid structure, many HFSB didn't reach the measurement volume. For the Reynolds number $Re_\tau = 4200$, between $150000 - 170000$ particles were tracked per time step on average. This results in a particle density per pixel (ppp) of $ppp = 0.02$. The average size of the bubbles varies between $300 - 500\,\mu$m, depending on the chosen combination of Helium, air and soap flow. The maximum number of particles stated above is only possible with small particle sizes. For this measurements, a particle size of $400\,\mu$m was aimed, which is the optimal size to have nearly neutral buoyancy in air (Bosbach et al., 2009).

Table 8.1: Experimental parameters of the volumetric measurements

System	Cameras	Position	Sensor Size pixel^2	FOV m^3
A	4x Phantom Veo4K 990	ZPG	4096×2160	$1.53 \times 0.6 \times 0.18$
B	4x PCO Dimax S4	ZPG, FPG	2016×2016	$0.78 \times 0.7 \times 0.21$
C	4x PCO Dimax S4	APG	2016×2016	$0.81 \times 0.7 \times 0.25$

In time resolved measurements, the overall time of one run, which is limited by the memory of the used cameras, is an important measure to quantify the number of captured statistical independent flow events. For this measurement campaign 1382 images were taken per run, which equals 1.382 s at a recording rate of 1 kHz. Achieving a free stream velocity $u_\infty = 13.5\,\mathrm{m/s}$ over the ZPG section of the boundary layer model, 170 boundary layer turn over times $\tau_\delta = \frac{\delta_{99}}{u_\infty}$ were captured per run. As shown in section 4.3, large-scale structures with a streamwise length of $L_2 \approx 8\,\delta_{99}$ are present within the boundary layer flow. Hence, optimistically estimated a maximum of 21 independent large-scale structures could be measured per run. During the campaign a total number of 89 runs were captured at $Re_\tau = 4200$, which results at best in 1869 structure turn overs. Therefore, the results based on the data set can not be considered fully converged for a statistical structure analysis. But nonetheless, the data yields unique new insights in turbulent flows and especially the three-dimensionality of the structural pattern within the boundary layer.

8.2. Results of the volumetric measurement

The raw images were processed with the “Shake the Box (STB)” particle tracking algorithm (Schanz et al., 2016). The major difference between common tomographic codes and the STB algorithm is a particle position predictor step, which allows to predict a particle position $x(t_{n+1})$ based on the tracks calculated up to time step t_n. Due to the predictor step, much higher particle concentrations can be tracked. The latest STB code successfully handled particle densities of $0.2\,ppp$ in artificial noise free data and $0.1\,ppp$ in noisy images (Schanz et al., 2016). Further details on the STB algorithm can be found in Schanz et al. (2016); Gesemann et al. (2016); Novara et al. (2019).

In figure 8.2 a side view of the flow over the boundary layer model 2 at $Re_\tau = 4200$ is shown. The axes are normalised with the boundary layer thickness in the ZPG section at $x^* = 0$. Clearly visible is the ZPG area, followed by a favourable pressure gradient (FPG)

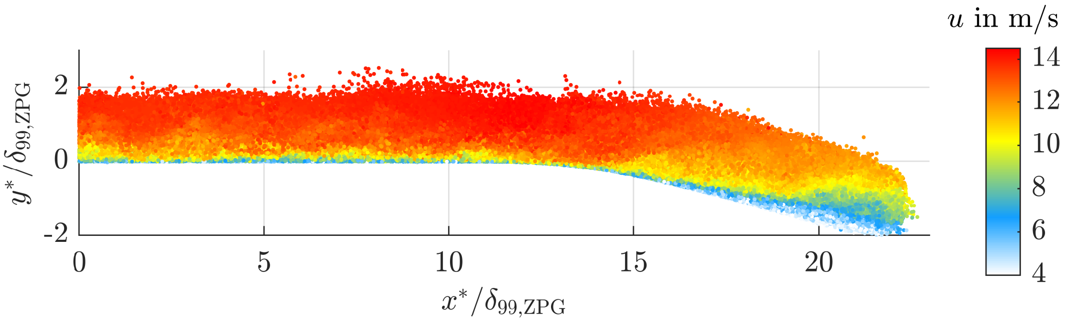

Figure 8.2: Instantaneous snapshot of the tracked HFSB at $Re_\tau = 4200$. Axis normalised with the ZPG boundary layer thickness $\delta_{99,\mathrm{ZPG}}$. Contours correspond to streamwise velocity u.

near the bent of the model and the large APG section. At $x^*/\delta_{99,\mathrm{ZPG}} > 20$ the flow separation is present. Multiple shear layers are present where the flow is under the APG impact.

In figure 8.3 two instantaneous flow fields of the volumetric data set are shown. The contour levels correspond to the relative fluctuations $u'/\overline{u}$. For better visualisation the contour limits are different in both figures. While the upper plot shows the data set up to $y^* < 1.2\,\delta_{99}$, in the lower plot only a wall-parallel cut sub-volume of the particle cloud with wall distance $y^* < 0.4\,\delta_{99}$ is shown, including the logarithmic layer. In both figures large-scale structures are clearly visible. While in the top figure the spot-wise intermittent pattern of laminar and turbulent flow is present, the elongated meandering large-scale structures are apparent in the lower figure. Also structures penetrating into the APG and the separation region can be found. Therefore, the conclusions drawn from the correlation and two-dimensional analysis in the previous chapters are confirmed based on a volumetric Lagrangian data set.

The shortcomings and problems of the three-dimensional STB data set are apparent as well. In the APG section and the vicinity of the separation bubble at $x^*/\delta_{99,\mathrm{ZPG}} > 20$ the particles are thinned out especially closer to the wall. The vortices in flow separation force the HFSB towards the wall and more particles implode. Also the overall seeding density is coarse. It is sufficient for the analysis of large-scale structures, as these are also detectable in the instantaneous image, but smaller flow features and vortices are difficult to detect with a robust criterion or are not resolved at all.

To assess the 3-dimensional structure shapes, volumetric two-point correlation functions are calculated and shown in figure 8.4 for three exemplary locations in a sub-volume of the data set with a spanwise extension of $3\,\delta_{99,\mathrm{ZPG}}$. For better comparison the curved boundary-layer model is plotted as a flat plate with a relative wall coordinate y^*_{rel} at the vertical axis. The correlation point P is chosen for all locations at a relative wall distance $y^*_{\mathrm{rel}}/\delta_{99} = 0.35$. This enables a direct visual comparison of the structure shapes. On top of the correlation functions the normalised boundary layer thickness $\delta_{99}/\delta_{99,\mathrm{ZPG}}$ is plotted as a shaded contour surface. At the upstream locations until approximately $x^*/\delta_{99,\mathrm{ZPG}} = 12$ within the ZPG section, the boundary-layer thickness is nearly constant. This region is followed by a decrease of the boundary-layer thickness for the FPG region and at the most downstream positions a strong increase in boundary-layer thickness for the APG region up to $1.8\,\delta_{99,\mathrm{ZPG}}$.

The two-point correlation functions consist of a positive correlated region in the centre (red) flanked by two clubs of negative correlations (blue) on each side in spanwise direction. This is in accordance with the observations from the 2-dimensional analysis in the previous chapters. While for the correlation functions in the ZPG regions no changes are visible, the

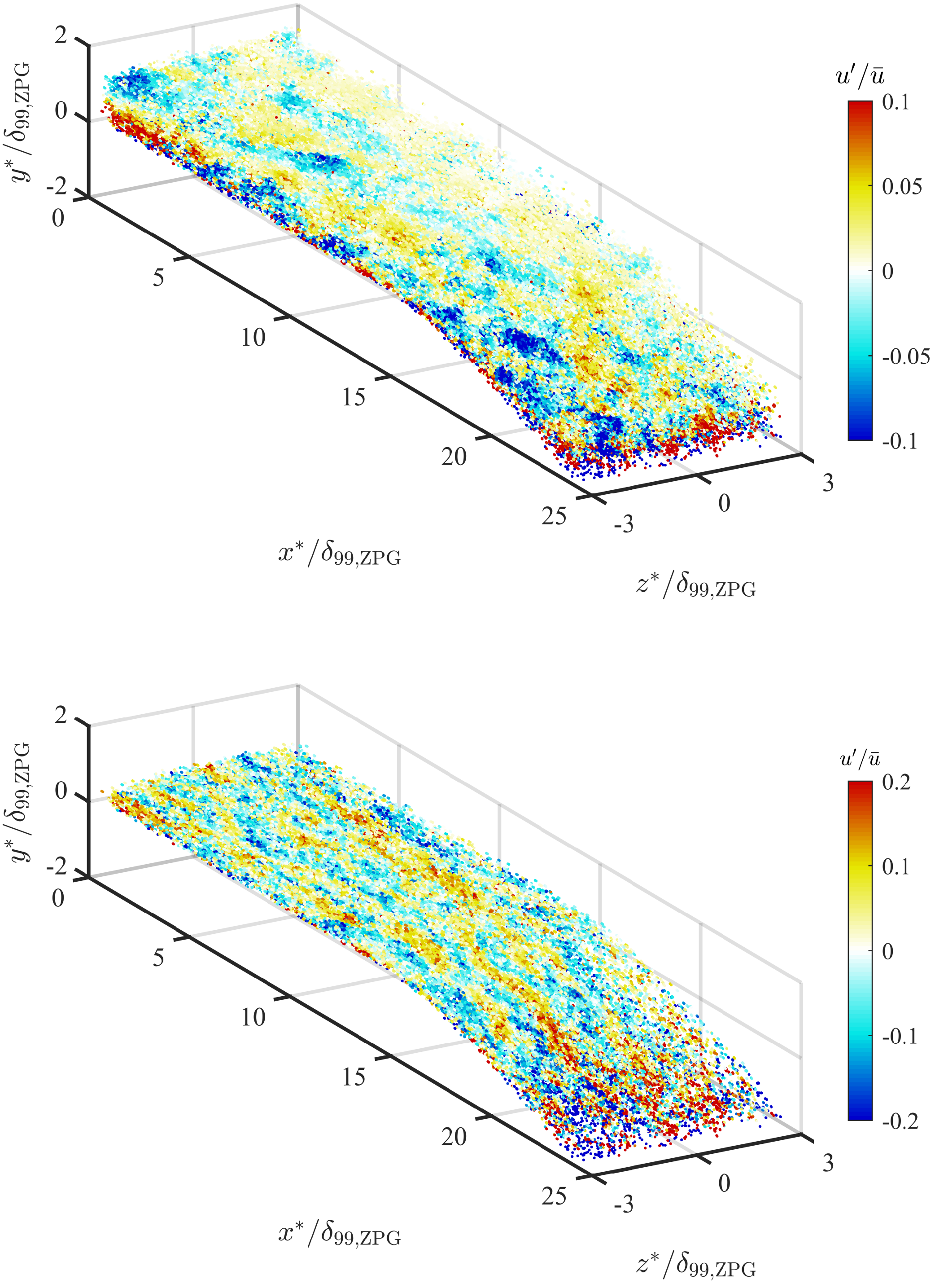

Figure 8.3: Exemplary instantaneous evaluation result at $Re_\tau = 4200$. Wall-parallel cut subvolume of the particle cloud with wall distances $y^* = 0 - 1.2\,\delta_{99}$ (top) and $y^* = 0 - 0.4\,\delta_{99}$ (bottom). Contours correspond to the normalised streamwise velocity fluctuations $u'/\overline{u}$.

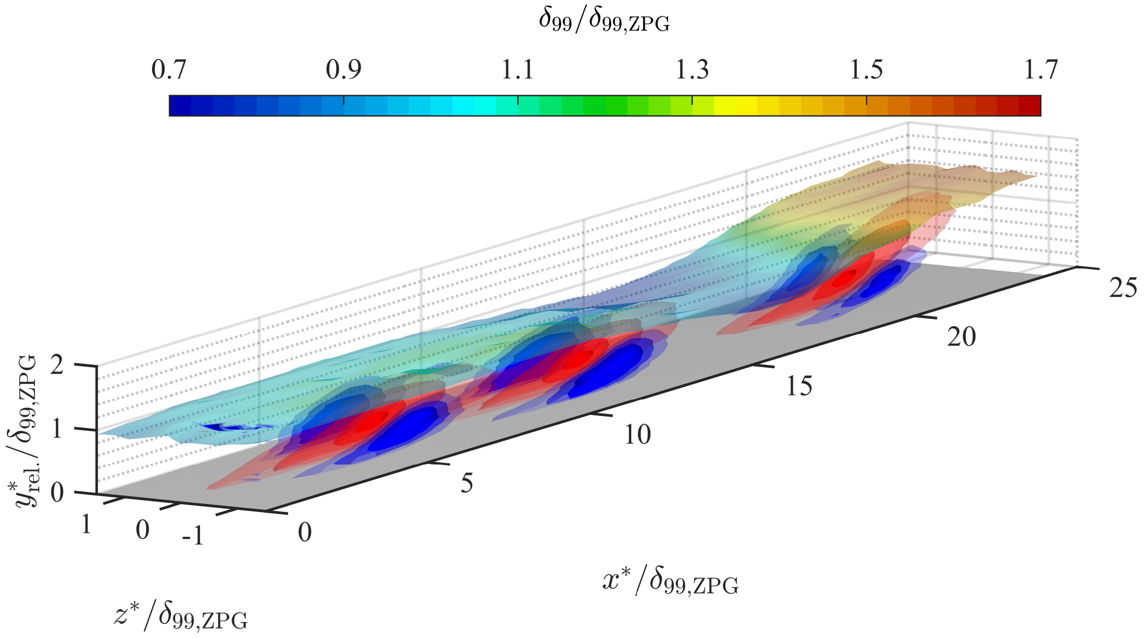

Figure 8.4: Volumetric two-point correlation functions. The contour levels are chosen at $R_{uu} = -0.15$; -0.12; -0.09; 0.15; 0.25; 0.45 and 0.65. The wall normal coordinate y^*_{rel} is defined as the normal distance to the model surface (grey). Superimposed is the relative boundary layer thickness $\delta_{99}/\delta_{99,\mathrm{ZPG}}$ as a shaded contour surface.

inclination of the correlation function increases in the APG. Furthermore, the inclination is not constant as for the ZPG correlation functions but is bent away from the wall with increasing wall distance. In all three cases a long tail of positive correlation in upstream direction is present.

9

Summary

Even after decades of intensive research, turbulent flows and especially turbulent boundary-layer flows are still not fully understood. In order to improve the understanding of the physical processes in a turbulent boundary-layer flow, knowledge of the principal features within the flow, such as large energy-carrying structures, is crucial to enhance the understanding of the turbulence physics itself. Within the scope of this dissertation, large-scale coherent structures in turbulent boundary-layer flows were investigated in detail. The aim of the research was to improve the understanding of large scale structure generation, interaction, dynamics and decay.

Therefore, large field of view PIV measurements were conducted to detect and analyse large-scale coherent structures in turbulent boundary layers with and without pressure gradients. The advantage of PIV as an optical method is that spatial structures can be identified and analysed directly and without a reconstruction hypothesis. Utilising multiple camera systems aligned side by side enabled the acquisition of the large-scale structures in their full spatial extent. The experiments were all performed in the Atmospheric Wind Tunnel Munich, which is an Eiffel type wind tunnel at the Bundeswehr Universität München, that allows research on turbulent boundary-layer flows at technically relevant Reynolds numbers up to $Re_\tau = 13400$. In order to achieve a pressure gradient distribution, the wind tunnel side wall was equipped with two different flow deflections that accelerate and decelerate the flow, resulting in a well-defined adverse pressure gradient flow up to flow separation.

The comparison of the instantaneous flow fields showed a characteristic streaky nature of the meandering large-scale turbulent flow structures. A multi-point statistical analysis of the instantaneous flow fields reveals that the length of the large-scale structures is relatively constant in the measurement plane, but the structure spacing of large-scale structures increases with the wall distance. This is explained by statistical analysis effects due to the natural height variation of large-scale structures and redistribution of streamwise momentum around ejection events. The structure height calculated from two-point correlations also increases with the wall distance, but three different slope regimes indicate the existence of different physical behaviours or states of the structures.

In order to further understand the scaling trends, the laminar flow regimes are masked out by a newly developed seeding concentration approach. Thereby, it is possible to separate a bias based on laminar flow regions in the statistical analysis from the true turbulent structure scaling, growth and dynamics. The results prove that intermittency biases the calculated length scales based on two-point correlation analysis. Overall, the spatial scales are overestimated without masking of the laminar flow regions. Above a wall distance of $y/\delta_{99} = 0.3-0.4$ the structure width and height stays nearly constant and no further structure growth occurs.

Intermittency itself starts at a wall distance around $y/\delta_{99} = 0.4$, but the effect on structures is detectable down to a wall distance of $y/\delta_{99} = 0.25$.

Of key interest is the effect of streamwise momentum of the structures on the analysis and the conclusions drawn. Therefore, the data were conditioned on high and low-momentum flow events. The analysis shows an increase in large-scale structure length up to $8\,\delta_{99}$ with increasing turbulent kinetic energy. Furthermore, the analysis indicates that low-momentum structures are the primary structures and observed high-momentum structures are fluid in gaps between the low-momentum structures.

To better understand the processes in a turbulent boundary layer, conceptual models are necessary. Therefore, a comparison between synthetic flow fields based on the attached-eddy model (AEM) and experimental data is presented to examine the predictive capabilities of spatial features in turbulent boundary layers from the model. To this end, the streamwise velocity and spanwise velocity components are analysed qualitatively and quantitatively on wall-parallel and cross-stream planes. The findings reveal that the resulting spatial coherence of the AEM synthetic flow fields is too strong and do not reproduce the meandering behaviour of flow features to the direction of flow.

Based on these observations, a modified AEM configuration is introduced to improve the spatial representation which incorporates the meandering of large-scale structures to the flow direction. The results confirm that the spatial representation of the instantaneous flow features is improved through this inclusion by reducing periodic effects and improving the estimation of spatial coherence. Although the modified AEM and the experimental data show improved similarity, the multipoint statistics are still observed to differ in the cross-plane for two main reasons. First, the AEM does not account for intermittency effects, which leads to increased correlation in the wake region. Second, the near-wall structures are different from logarithmic-layer structures in a turbulent boundary layer flow and the model does not account for flow structures that do not extend to the wall. Hence, the correlation is increased down to the wall. Further, the AEM is a statistically based model that does not directly account for the dynamic aspects of the flow motion, which include the generation, development and decay of the eddies, nor their formation into packets.

Analysing the flow field around large-scale structures, it is possible to better understand the turbulence dynamics associated with the structure. Longitudinal vortices are identified which flank large-scale structures and ejection events. Conditional averages are used to demonstrate that the vortices are a persistent feature in the flow and not a random effect. In addition, an increase in turbulence production between the eddies is observed, which emphasises the importance of the turbulent structures for the generation of the turbulence itself. The observed vortices in the conditional fields are larger in spatial extension than postulated hairpin vortices. To further quantify the vortices, bivariate distributions of vortex size, wall-distance and circulation are calculated from the instantaneous Stereo-PIV fields. The results show that the most likely vortices and the vortices with the highest circulation are in the upper logarithmic layer and slightly above. In the outer boundary layer, almost no large vortices are detected. Based on these observations and the scaling trends, a self-supporting flanking vortex model is proposed which explains the generation of large-scale structures based on shear instability and the redistribution of momentum by large vortices in the flow. The observations in the instantaneous flow fields and the calculated statistics strongly support the model. In contrast to other existing models, this explanation is not based on a hierarchical structure order within the boundary layer. Another major difference is the assumed primary structure. So far, large-scale structures elongated in the direction of flow have been explained as a secondary effect of the action of hairpin-shaped or lambda-shaped eddies, whereas this explanation assumes streamwise vortices as the primary feature of a turbulent boundary-layer flow.

The third major research area of this thesis was, besides the scaling and dynamics of large-scale structures, the influence of an adverse pressure gradient up to the flow separation on large-scale structures and the interaction of large-scale structures with the flow separation itself. Two-point correlations and observations in instantaneous flow fields show that the structural pattern does not change significantly with pressure gradients. This shows that large-scale structures retain their structural characteristics until they interact with the separated region. The streamwise length of the correlation decreases due to the flow deceleration. Furthermore, the slope relative to the wall increases up to $\alpha = 27^\circ$. In contrast to the length, the spanwise distance of the structures is unaffected by the adverse pressure gradient. Only in the immediate vicinity of the separated region the spanwise scales change.

The unsteadiness of the flow separation front was associated with the effect of turbulent large-scale structures. However, the mean boundary parameters are also partly determined by the topology and dynamics of the large-scale structures. While no influence on the boundary layer thickness δ_{99} could be found, the displacement and momentum thickness and consequently the shape factor change and can be used to quantify the state of the boundary-layer flow. Furthermore, conditioned flow analysis showed an interaction between the large-scale structures and the separated region, which takes place in the inner boundary layer up to $y^*/\delta_{99} < 0.6$. The point of separation and the dynamics of the separation depend on the stream-wise momentum of the large-scale structures. The outer flow is unchanged by the unsteady separated region. These observations make it possible to better understand the dynamics of pressure-induced flow separations.

As the turbulent boundary-layer flow is a three-dimensional flow problem, the conclusions and explanations drawn from the two-dimensional analysis are always limited and questionable to a certain extent. Therefore, a unique experiment was performed, in which a turbulent boundary-layer flow was measured time-resolved at a technically interesting Reynolds number of $Re_\tau = 4200$. The preliminary results show that the conclusions discussed above are consistent with the observations in the three-dimensional data set. Also the shortcomings of such measurements become obvious, namely the great effort and the coarse spatial resolution. Both could be overcome in the near future by improvements in camera technology and the number of cameras used as well as by improved seeding generation and seeding insertion.

Nonetheless, time-resolved volumetric measurement is the direction in which experimental research must proceed in order to obtain a better understanding of the coherent flow structures in the boundary-layer flow. On the other hand, the spatial resolution is significantly smaller in large field-of-view volumetric experiments and volumetric experiments are also insufficient. This is directly apparent in the discussions within this thesis, in which many observations from literature are confirmed and supported, but also interpreted differently. The consequent next step would therefore not be the attempt to further fit turbulent boundary layers and their structures into narrow models, but to combine the explanations from vortex dynamics and scaling trends given in this thesis by further experimental evidence.

Bibliography

Adrian, R. J., 2007. Hairpin vortex organization in wall turbulence. Physics of Fluids 19 (4), 041301.

Adrian, R. J., Meinhart, C. D., Tomkins, C. D., 2000. Vortex organization in the outer region of the turbulent boundary layer. Journal of Fluid Mechanics 422, 1–54.

Adrian, R. J., Westerweel, J., 2011. Particle image velocimetry. Cambridge University Press.

Balakumar, B. J., Adrian, R. J., 2007. Large-and very-large-scale motions in channel and boundary-layer flows. Philosophical Transactions of the Royal Society of London A: Mathematical, Physical and Engineering Sciences 365 (1852), 665–681.

Berkooz, G., Holmes, P.and Lumley, J. L., 1993. The proper orthogonal decomposition in the analysis of turbulent flows. Annual review of fluid mechanics 25 (1), 539–575.

Bosbach, J., Kühn, M., Wagner, C., 2009. Large scale particle image velocimetry with helium filled soap bubbles. Experiments in fluids 46 (3), 539–547.

Bradshaw, P., 1965. The effect of wind-tunnel screens on nominally two-dimensional boundary layers. Journal of Fluid Mechanics 22 (4), 679–687.

Bross, M., Fuchs, T., Kähler, C. J., 2019. Interaction of coherent flow structures in adverse pressure gradient turbulent boundary layers. J. Fluid Mech. 873, 287–321.

Bross, M., Kähler, C. J., 2016. Time-resolved 3D-PTV Analysis of near wall reverse flow events in apg turbulent boundary layers. In: 18th International Symposia on Applications of Laser Techniques to Fluid Mechanics, 04. - 07. July. 2016, Lisbon, Portugal. pp. 438–458.

Buchmann, N. A., Kücükosman, Y. C., Ehrenfried, K., Kähler, C. J., 2016. Wall pressure signature in compressible turbulent boundary layers. In: Progress in Wall Turbulence 2. Springer, pp. 93–102.

Chandran, D., Baidya, R., Monty, J. P., Marusic, I., 2017. Two-dimensional energy spectra in high-Reynolds-number turbulent boundary layers. Journal of Fluid Mechanics 826.

Chauhan, K., Nagib, H., Monkewitz, P., 2007. On the composite logarithmic profile in zero pressure gradient turbulent boundary layers. In: 45th AIAA Aerospace Sciences Meeting and Exhibit. p. 532.

Chauhan, K., Philip, J., de Silva, C. M., Hutchins, N., Marusic, I., 2014. The turbulent/non-turbulent interface and entrainment in a boundary layer. Journal of Fluid Mechanics 742, 119–151.

Cuvier, C., Srinath, S., Stanislas, M., Foucaut, J. M., Laval, J. P., Kähler, C. J., Hain, R., Scharnowski, S., Schröder, A., Geisler, R., et al., 2017. Extensive characterisation of a high reynolds number decelerating boundary layer using advanced optical metrology. Journal of Turbulence 18 (10), 929–972.

de Silva, C., Kevin, K., Baidya, R., Hutchins, N., Marusic, I., 2018. Large coherence of spanwise velocity in turbulent boundary layers. Journal of Fluid Mechanics 847, 161–185.

de Silva, C. M., Woodcock, J. D., Hutchins, N., Marusic, I., 2016. Influence of spatial exclusion on the statistical behavior of attached eddies. Physical Review Fluids 1 (2), 022401.

Dennis, D. J., Nickels, T., 2011. Experimental measurement of large-scale three-dimensional structures in a turbulent boundary layer. Part 2. Long structures. Journal of Fluid Mechanics 673, 218–244.

Dennis, D. J. C., Nickels, T. B., 2008. On the limitations of Taylor's hypothesis in constructing long structures in a turbulent boundary layer. Journal of Fluid Mechanics 614, 197–206.

Eich, F., de Silva, C. M., Marusic, I., Kähler, C. J., 2020. Towards an improved spatial representation of a boundary layer from the attached eddy model. Phys. Rev. Fluids 5, 034601.

Eich, F., Kähler, C. J., 2017. Towards capturing large scale coherent structures in boundary layers using particle image velocimetry. In: Proceedings of the 10th Turbulence and Shear Flow Phenomena Conference, 06. - 09. July. 2017, Chicago, USA.

Eich, F., Kähler, C. J., 2019. Large-scale structures in turbulent boundary layers under an adverse pressure gradient up to flow separation. In: Proceedings of the 11th Turbulence and Shear Flow Phenomena Conference, 30. July - 02. August. 2019, Southampton, UK.

Eich, F., Kähler, C. J., 2020. Large-scale coherent motions in turbulent boundary layers under an adverse pressure gradient up to flow separation. International Journal of Heat and Fluid Flow 85, 108645.

Eitel-Amor, G., Örlü, R., Schlatter, P., 2014. Simulation and validation of a spatially evolving turbulent boundary layer up to $Re_\theta = 8300$. International Journal of Heat and Fluid Flow 47, 57–69.

Elyasi, M., Ghaemi, S., 2019. Experimental investigation of coherent structures of a three-dimensional separated turbulent boundary layer. Journal of Fluid Mechanics 859, 1–32.

Fernholz, H. H., Finley, P. J., 1996. The incompressible zero-pressure-gradient turbulent boundary layer: An assessment of the data. Progress in Aerospace Sciences 32 (4), 245–311.

Fröhlich, J., von Terzi, D., 2008. Hybrid LES/RANS methods for the simulation of turbulent flows. Progress in Aerospace Sciences 44 (5), 349–377.

Ganapathisubramani, B., Hutchins, N., Hambleton, W. T., Longmire, E. K., Marusic, I., 2005. Investigation of large-scale coherence in a turbulent boundary layer using two-point correlations. Journal of Fluid Mechanics 524, 57–80.

Ganapathisubramani, B., Longmire, E. K., Marusic, I., 2003. Characteristics of vortex packets in turbulent boundary layers. Journal of Fluid Mechanics 478, 35–46.

Gesemann, S., Huhn, F., Schanz, D., Schröder, A., 2016. From noisy particle tracks to velocity, acceleration and pressure fields using B-splines and penalties. In: 18th International Symposia on Applications of Laser Techniques to Fluid Mechanics, 04. - 07. July. 2016, Lisbon, Portugal. pp. 371–384.

Graftieaux, L., Michard, M., Grosjean, N., 2001. Combining PIV, POD and vortex identification algorithms for the study of unsteady turbulent swirling flows. Measurement Science and technology 12 (9), 1422.

Grant, H. L., 1958. The large eddies of turbulent motion. Journal of Fluid Mechanics 4 (2), 149–190.

Hain, R., Scharnowski, S., Reuther, N.and Kähler, C. J., Schröder, A., Geisler, R., Agocs, J., Röse, A., Novara, M., Stanislas, M., et al., 2016. Coherent large scale structures in adverse pressure gradient turbulent boundary layers. In: 18th international symposium on the application of laser and imaging techniques to fluid mechanics Lisbon Portugal July 4, 7, 2016. pp. 474–496.

Harun, Z., Monty, J. P., Mathis, R., Marusic, I., 2013. Pressure gradient effects on the large-scale structure of turbulent boundary layers. Journal of Fluid Mechanics 715, 477–498.

Head, M., Bandyopadhyay, P., 1981. New aspects of turbulent boundary-layer structure. Journal of fluid mechanics 107, 297–338.

Hunt, J., Morrison, J. F., 2000. Eddy structure in turbulent boundary layers. European Journal of Mechanics-B/Fluids 19 (5), 673–694.

Hutchins, N., Chauhan, K., Marusic, I., Monty, J. P., Klewicki, J., 2012. Towards reconciling the large-scale structure of turbulent boundary layers in the atmosphere and laboratory. Boundary-layer meteorology 145 (2), 273–306.

Hutchins, N., Hambleton, W. T., Marusic, I., 2005. Inclined cross-stream stereo particle image velocimetry measurements in turbulent boundary layers. Journal of Fluid Mechanics 541, 21–54.

Hutchins, N., Marusic, I., 2007a. Large-scale influences in near-wall turbulence. Philosophical Transactions of the Royal Society of London A: Mathematical, Physical and Engineering Sciences 365 (1852), 647–664.

Hutchins, N., Marusic, I., 2007b. Evidence of very long meandering features in the logarithmic region of turbulent boundary layers. Journal of Fluid Mechanics 579, 1–28.

Hutchins, N., Nickels, T. B., Marusic, I., Chong, M. S., 2009. Hot-wire spatial resolution issues in wall-bounded turbulence. Journal of Fluid Mechanics 635, 103–136.

Hwang, J., Sung, H. J., 2018. Wall-attached structures of velocity fluctuations in a turbulent boundary layer. Journal of Fluid Mechanics 856, 958–983.

International Civil Aviation Organization, 2019. Envisioning a “zero climate impact” international aviation pathway towards 2050: How governments and the aviation industry can step-up amidst the climate emergency for a sustainable aviation future, Working Paper A40-WP/561.

Jiménez, J., 2018. Coherent structures in wall-bounded turbulence. Journal of Fluid Mechanics 842.

Jones, M. B., Marusic, I., Perry, A. E., 1995. The effect of aspect ratio and divergence on the turbulence structure of boundary layers. In: Proc. 12th Australasian Fluid Mech. Conf. pp. 436–439.

Kähler, C. J., 2004. Investigation of the spatio-temporal flow structure in the buffer region of a turbulent boundary layer by means of multiplane stereo PIV. Experiments in Fluids 36 (1), 114–130.

Kähler, C. J., Sammler, B., Kompenhans, J., 2002. Generation and control of tracer particles for optical flow investigations in air. Experiments in Fluids 33 (6), 736–742.

Kevin, K., Monty, J. P., Hutchins, N., 2019. The meandering behaviour of large-scale structures in turbulent boundary layers. Journal of Fluid Mechanics 865.

Kim, K. C., Adrian, R. J., 1999. Very large-scale motion in the outer layer. Physics of Fluids 11 (2), 417–422.

Kitsios, V., Sekimoto, A., Atkinson, C., Sillero, J. A., Borrell, G., Gungor, A. G., Jiménez, J., Soria, J., 2017. Direct numerical simulation of a self-similar adverse pressure gradient turbulent boundary layer at the verge of separation. Journal of Fluid Mechanics 829, 392–419.

Klebanoff, P. S., 1955. Characteristics of turbulence in boundary layer with zero pressure gradient. NACA Technical Report 1247.

Klewicki, J. C., 2010. Reynolds number dependence, scaling, and dynamics of turbulent boundary layers. Journal of fluids engineering 132 (9), 094001.

Kline, S. J., Reynolds, W. C., Schraub, F. A., Runstadler, P. W., 1967. The structure of turbulent boundary layers. Journal of Fluid Mechanics 30 (4), 741–773.

Kline, S. J., Robinson, S. K., 1990. Turbulent boundary layer structure: Progress, status, and challenges. In: Structure of Turbulence and Drag Reduction. Springer, pp. 3–22.

Knopp, T., Buchmann, N. A., Schanz, D., Eisfeld, B., Cierpka, C., Hain, R., Schröder, A., Kähler, C. J., 2015. Investigation of scaling laws in a turbulent boundary layer flow with adverse pressure gradient using PIV. Journal of Turbulence 16 (3), 250–272.

Knopp, T., Novara, M., Schanz, D., Schülein, E., Schröder, A., Reuther, N., Kähler, C. J., 2018. A new experiment of a turbulent boundary layer flow at adverse pressure gradient for validation and improvement of RANS turbulence models. In: New Results in Numerical and Experimental Fluid Mechanics XI. Springer, pp. 85–94.

Knopp, T., Schanz, D., Schröder, A., Dumitra, M., Cierpka, C., Hain, R., Kähler, C. J., 2014. Experimental investigation of the log-law for an adverse pressure gradient turbulent boundary layer flow at $Re_\theta = 10000$. Flow, turbulence and combustion 92 (1-2), 451–471.

Krogstad, P.-Å., Skåre, P. E., 1995. Influence of a strong adverse pressure gradient on the turbulent structure in a boundary layer. Physics of Fluids 7 (8), 2014–2024.

Lachmann, G. V., 2014. Boundary layer and flow control: its principles and application. Elsevier.

Lenaers, P., Li, Q., Brethouwer, G., Schlatter, P., Örlü, R., 2012. Rare backflow and extreme wall-normal velocity fluctuations in near-wall turbulence. Physics of fluids 24 (3), 035110.

Maciel, Y., Gungor, A. G., Simens, M., 2017. Structural differences between small and large momentum-defect turbulent boundary layers. International Journal of Heat and Fluid Flow 67, 95–110.

Maciel, Y., Wei, T., Gungor, A. G., Simens, M. P., 2018. Outer scales and parameters of adverse-pressure-gradient turbulent boundary layers. Journal of Fluid Mechanics 844, 5–35.

Marusic, I., 2001. On the role of large-scale structures in wall turbulence. Physics of Fluids 13 (3), 735–743.

Marusic, I., McKeon, B. J., Monkewitz, P. A., Nagib, H. M., Smits, A. J., Sreenivasan, K. R., 2010. Wall-bounded turbulent flows at high Reynolds numbers: Recent advances and key issues. Physics of Fluids 22 (6), 065103.

Marusic, I., Monty, J. P., 2019. Attached eddy model of wall turbulence. Annual Review of Fluid Mechanics 51, 49–74.

Marusic, I., Monty, J. P., Hultmark, M., Smits, A. J., 2013. On the logarithmic region in wall turbulence. Journal of Fluid Mechanics 716.

Marusic, I., Perry, A. E., 1995. A wall-wake model for the turbulence structure of boundary layers. Part 2. Further experimental support. Journal of Fluid Mechanics 298, 389–407.

Mathis, R., Hutchins, N., Marusic, I., 2009. Large-scale amplitude modulation of the small-scale structures in turbulent boundary layers. Journal of Fluid Mechanics 628, 311–337.

Monty, J. P., Harun, Z., Marusic, I., 2011. A parametric study of adverse pressure gradient turbulent boundary layers. International Journal of Heat and Fluid Flow 32 (3), 575–585.

Monty, J. P., Hutchins, N., Ng, H. C. H., Marusic, I., Chong, M. S., 2009. A comparison of turbulent pipe, channel and boundary layer flows. Journal of Fluid Mechanics 632, 431–442.

Nagib, H. M., Chauhan, K. A., 2008. Variations of von Kármán coefficient in canonical flows. Physics of Fluids 20 (10), 101518.

Nickels, T. B., 2004. Inner scaling for wall-bounded flows subject to large pressure gradients. Journal of Fluid Mechanics 521, 217–239.

Nickels, T. B., Marusic, I., Hafez, S., Hutchins, N., Chong, M. S., 2007. Some predictions of the attached eddy model for a high Reynolds number boundary layer. Philosophical Transactions of the Royal Society of London A: Mathematical, Physical and Engineering Sciences 365 (1852), 807–822.

Nieuwstadt, F. T. M., Westerweel, J., Boersma, B. J., 2016. Turbulence: Introduction to theory and applications of turbulent flows. Springer.

Novara, M., Schanz, D., Geisler, R., Gesemann, S., Voss, C., Schröder, A., 2019. Multi-exposed recordings for 3D Lagrangian particle tracking with Multi-Pulse Shake-The-Box. Experiments in Fluids 60 (3), 44.

Oertel, H., Böhle, M., Ehrhard, P., Etling, D., Müller, U., Riedel, U., Sreenivasan, K. R., 2013. Prandtl-Führer durch die Strömungslehre: Grundlagen und Phänomene. Springer-Verlag.

Österlund, J. M., Johansson, A. V., Nagib, H. M., Hites, M. H., 2000. A note on the overlap region in turbulent boundary layers. Physics of Fluids 12 (1), 1–4.

Pamiès, M., Weiss, P., Garnier, E., Deck, S., Sagaut, P., 2009. Generation of synthetic turbulent inflow data for large eddy simulation of spatially evolving wall-bounded flows. Physics of Fluids 21 (4), 045103.

Perry, A. E., Henbest, S., Chong, M., 1986. A theoretical and experimental study of wall turbulence. Journal of Fluid Mechanics 165, 163–199.

Pope, S. B., 2011. Turbulent flows. Cambridge Univ. Press.

Raffel, M., Willert, C. E., Scarano, F., Kähler, C. J., Wereley, S. T., Kompenhans, J., 2018. Particle image velocimetry: A practical guide. Springer.

Reuther, N., Kähler, C., 2018. Evaluation of large-scale turbulent/non-turbulent interface detection methods for wall-bounded flows. Experiments in Fluids 59 (7), 121.

Reuther, N., Kähler, C. J., 2019. Effect of the intermittency on the outer scales in turbulent boundary layers. In: Proceedings of the 11th Turbulence and Shear Flow Phenomena Conference, 30. July - 02. August. 2019, Southampton, UK.

Reuther, N., Kähler, C. J., 2020. Effect of the intermittency dynamics on single and multi-point statistics of turbulent boundary layers. Journal of Fluid Mechanics 897.

Reuther, N., Schanz, D., Scharnowski, S., Hain, R., Schröder, A., Kähler, C. J., 2015. Experimental investigation of adverse pressure gradient turbulent boundary layers by means of large-scale PIV. In: 11th International Symposium on Particle Image Velocimetry - PIV15 -, 14. - 16. Sept. 2015, Santa Barbara, CA, USA.

Robinson, S. K., 1991. Coherent motions in the turbulent boundary layer. Annual Review of Fluid Mechanics 23 (1), 601–639.

Samie, M., Marusic, I., Hutchins, N., Fu, M. K., Fan, Y., Hultmark, M., Smits, A. J., 2018. Fully resolved measurements of turbulent boundary layer flows up to $Re_\tau = 20000$. Journal of Fluid Mechanics 851, 391–415.

Schanz, D., Gesemann, S., Schröder, A., 2016. Shake-The-Box: Lagrangian particle tracking at high particle image densities. Experiments in fluids 57 (5), 70.

Schanz, D., Novara, M., Geisler, R., Agocs, J., Eich, F., Bross, M., Kähler, C. J., Schröder, A., 2019. Large-scale volumetric characterization of turbulent boundary layer flow. In: 13th International Symposium on Particle Image Velocimetry –ISPIV 2019, 22.-24. July, Munich.

Schlatter, P., Örlü, R., Li, Q., Brethouwer, G., Fransson, J. H. M., Johansson, A. V., Alfredsson, P. H., Henningson, D. S., 2009. Turbulent boundary layers up to $Re_\theta = 2500$ studied through simulation and experiment. Physics of fluids 21 (5), 051702.

Schlichting, H., Gersten, K., 2006. Grenzschicht-Theorie. Springer-Verlag.

Schulze, S., 2012. Experimentelle Untersuchungen zur Wirbeldynamik am überziehenden Triebwerkseinlauf. Ph.D. thesis, München, Univ. der Bundeswehr, 2012.

Sharma, A., Moarref, R., McKeon, B., 2017. Scaling and interaction of self-similar modes in models of high reynolds number wall turbulence. Philosophical Transactions of the Royal Society A: Mathematical, Physical and Engineering Sciences 375 (2089), 20160089.

Sillero, J., 2014. High reynolds number turbulent boundary layers. Ph.D. thesis, Universidad Politénica de Madrid.

Sillero, J., Jiménez, J., Moser, R. D., Malaya, N. P., 2011. Direct simulation of a zero-pressure-gradient turbulent boundary layer up to Re_θ=6650. In: Journal of Physics: Conference Series. Vol. 318. IOP Publishing, p. 022023.

Simmons, D., Thomas, F. O., Corke, T. C., 2019. Smooth body flow separation experiments and their surface flow topology characterization. In: AIAA Aviation 2019 Forum. p. 3085.

Simpson, R. L., 1989. Turbulent boundary-layer separation. Annual Review of Fluid Mechanics 21 (1), 205–232.

Skåre, P. E., Krogstad, P.-Å., 1994. A turbulent equilibrium boundary layer near separation. Journal of Fluid Mechanics 272, 319–348.

Smith, C., 1984. A synthesized model of the near-wall behavior in turbulent boundary layers. Tech. rep., Lehigh University Bethlehem Pa, Department of Mechanical Engineering and Mechanics.

Smith, C. R., Metzler, S. P., 1983. The characteristics of low-speed streaks in the near-wall region of a turbulent boundary layer. Journal of Fluid Mechanics 129, 27–54.

Smits, A. J., McKeon, B. J., Marusic, I., 2011. High-Reynolds number wall turbulence. Annual Review of Fluid Mechanics 43.

Spencer, A., Hollis, D., 2005. Correcting for sub-grid filtering effects in particle image velocimetry data. Measurement Science and Technology 16 (11), 2323.

Theodorsen, T., 1952. Mechanism of turbulence. In: Proc. Midwest. Conf. Fluid Mech. pp. 1–18.

Tomkins, C. D., Adrian, R. J., 2003. Spanwise structure and scale growth in turbulent boundary layers. Journal of Fluid Mechanics 490, 37–74.

Townsend, A. A., 1956. The structure of turbulent shear flow. Cambridge University Press.

Vinuesa, R., Hosseini, S., Hanifi, A., Henningson, D. S., Schlatter, P., 2017. Pressure-gradient turbulent boundary layers developing around a wing section. Flow, Turbulence and Combustion 99 (3-4), 613–641.

Waleffe, F., 1997. On a self-sustaining process in shear flows. Physics of Fluids 9 (4), 883–900.

Waleffe, F., 1998. Three-dimensional coherent states in plane shear flows. Physical Review Letters 81 (19), 4140.

Wallace, J. M., 2012. Highlights from 50 years of turbulent boundary layer research. Journal of Turbulence 13, N53.

Wallace, J. M., 2016. Quadrant analysis in turbulence research: History and evolution. Annual Review of Fluid Mechanics 48, 131–158.

Wallace, J. M., Eckelmann, H., Brodkey, R. S., 1972. The wall region in turbulent shear flow. Journal of Fluid Mechanics 54 (1), 39–48.

Westerweel, J., Fukushima, C., Pedersen, J. M., Hunt, J., 2009. Momentum and scalar transport at the turbulent/non-turbulent interface of a jet. Journal of Fluid Mechanics 631, 199–230.

Willert, C. E., Cuvier, C., Foucaut, J. M., Klinner, J., Stanislas, M., Laval, J. P., Srinath, S., Soria, J., Amili, O., Atkinson, C., et al., 2018. Experimental evidence of near-wall reverse flow events in a zero pressure gradient turbulent boundary layer. Experimental Thermal and Fluid Science 91, 320–328.

Woodcock, J., Marusic, I., 2015. The statistical behaviour of attached eddies. Physics of Fluids 27 (1), 015104.

Zhang, Q., Schröder, W., Meinke, M., 2010. A zonal RANS-LES method to determine the flow over a high-lift configuration. Computers & Fluids 39 (7), 1241–1253.

Appendix

A.1. Turbulent energy equation - APG

The conservation equation for the kinetic energy k, also called k-equation,

$$K = \frac{1}{2}\sqrt{\overline{u'^2} + \overline{v'^2} + \overline{w'^2}} \tag{A.1}$$

is central for the modelling and understanding of turbulence. The full equation for steady flows is giving in Schlichting and Gersten (2006). The k-equation balances the contributions convection, viscous+turbulent diffusion, production and dissipation. The production term k_P is defined as

$$\begin{aligned} k_\mathrm{p} = -\rho \left(\overline{u'^2}\frac{\partial \overline{u}}{\partial x} + \overline{u'v'}\frac{\partial \overline{v}}{\partial x} + \overline{u'w'}\frac{\partial \overline{w}}{\partial x} \right) \\ - \rho \left(\overline{u'v'}\frac{\partial \overline{u}}{\partial y} + \overline{v'^2}\frac{\partial \overline{v}}{\partial y} + \overline{v'w'}\frac{\partial \overline{w}}{\partial y} \right) \\ - \rho \left(\overline{u'w'}\frac{\partial \overline{u}}{\partial z} + \overline{v'w'}\frac{\partial \overline{v}}{\partial z} + \overline{w'^2}\frac{\partial \overline{w}}{\partial z} \right). \end{aligned} \tag{A.2}$$

As the focus of this thesis are turbulent boundary layers, multiple simplifications can be applied. The average velocities in spanwise $\overline{w}$ and wall-normal direction $\overline{v}$ are 0 for ZPG boundary layers. Furthermore, the gradients of the mean fields are 0. Using those assumption, the turbulence production simplifies to equation 2.6.

More complicated is the flow under an APG. Due to the positive pressure gradient in streamwise direction $\frac{\mathrm{d}p}{\mathrm{d}x} > 0$, the gradient $\frac{\mathrm{d}\overline{u}}{\mathrm{d}x} < 0$. Furthermore, the mean field $\overline{v} \neq 0$ due to the bend of the boundary layer model, as described in section 3.3. The resulting production equation for the APG is given by

$$k_\mathrm{p} = -\rho \left(\overline{u'^2}\frac{\partial \overline{u}}{\partial x} + \overline{u'v'}\frac{\partial \overline{v}}{\partial x} + \overline{u'v'}\frac{\partial \overline{u}}{\partial y} + \overline{v'^2}\frac{\partial \overline{v}}{\partial y} \right). \tag{A.3}$$

A.2. Wall-parallel flow fields masked

In figure A.1 the flow field from the bottom plot in figure 4.1 is masked based on different thresholds, depending on distribution of the streamwise velocity component u.

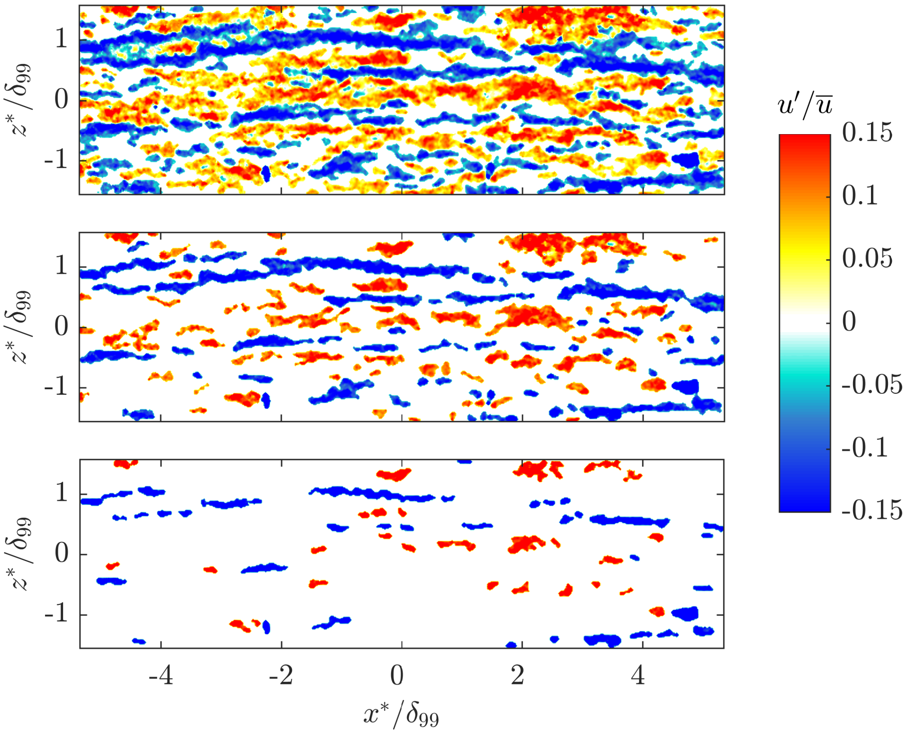

Figure A.1: Masked flow fields at $Re_\tau = 9300$ and a wall distance $y^*/\delta_{99} = 0.07$. Top:. Structures with $|u'| < 0.5\,\sigma_u$ are masked out. Centre: Structures with $|u'| < 1\,\sigma_u$ are masked out. Bottom: Structures with $|u'| < 1.5\,\sigma_u$ are masked out.

A.3. Structures spacing calculation - binarisation algorithm test

In section 4.1 the large-scale structure spacing is calculated based on binarised images. Binarisation assigns discrete values of 0 and 1 to a flow field and is therefore dependent on the method chosen for the binarisation. In this case, the binarisation is based on a diagnosis variable χ, which is defined as

$$\chi = \frac{u - \overline{u}}{\sigma_u} \tag{A.4}$$

with the standard deviation σ_u of the streamwise velocity u. To reduce small scale fluctuations, those fields were filtered with a spatial filter calculating the median of 5×5 values of χ. In figure A.2 an exemplary field of the diagnosis factor χ is plotted. Clearly identifiable are the high (red) and low (blue) momentum structures. Due to the median filtering the structures are clearly separated and not biased by small scale fluctuations.

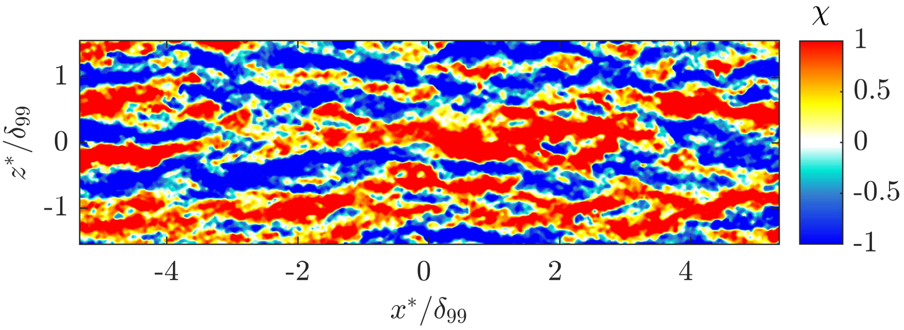

Figure A.2: Diagnosis factor χ in a wall-parallel x^*z^*-plane at $Re_\tau = 9300$.

The images are binarised in a way that the binarisation factor

$$I = 1 \, \forall \, \chi < k \cdot \sigma_u \tag{A.5}$$

with the threshold $k \cdot \sigma_u$ that defines the strength of the low-momentum structure. Within the binarised images, all streamwise locations are analysed and the distance between the centres of two regions with $I = 1$ is calculated. That distance is equal to the spacing Λ_2 of two low-momentum structures in a wall-parallel cut plane. In figure A.3 (left) the resulting probability density functions (PDF) of the spacings Λ_2 for different thresholds $k \cdot \sigma_u$ are plotted.

There is negligible impact for $k < 0.5$, at higher k values the structure spacings tend to increase because the events become more seldom and are therefore not representative for the structures as a whole any more. This effect is also visible in the masked flow fields in figure A.1. In addition, strong events are averaged by spatial median filtering. In the right plot in figure A.3 different window sizes for the spatial median filter are compared. A clear trend towards larger spacings with increasing window sizes is visible. A coherent structure in the wall-parallel measurements has an average spanwise extension of approximately 40 vectors. Hence, the spatial filter must be chosen significantly smaller. The analysis shows that smaller filtering results in smaller numbers for the structures spacing, which is a physical consequence of the calculation process. Based on those observations and assumptions, a filter width of 7×7 is a plausible choice. As the final calculated spacing values of Λ_2 are dependent on a chosen variable, the tool is only reliable to analyse scaling trends but not to quantify definite spacings.

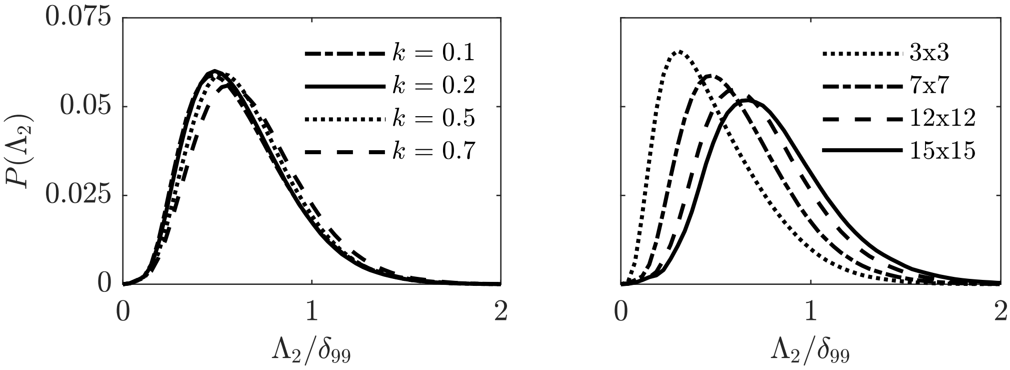

Figure A.3: Comparison of the binarisation variables influence on the Λ_2 spacing distribution at $Re_\tau = 9300$ calculated in a wall parallel plane at $y^*/\delta_{99} = 0.14$. The left plot shows the influence of different thresholds for the binarisation, the right plot the impact of varying windows sizes for the spatial median filtering.

For the analysis in chapter 4 the parameter k was chosen to $k = 0.1$ in order to capture all low-momentum structures. The filtering was applied with a filter width of 7×7.

A.4. Error estimation of the vortex parameter calculation

In chapter 6 a detailed investigation of the flow around large-scale structures is performed, also analysing the vortical pattern in the vicinity of a large-scale structure. Therefore, the vortices are detected and quantified. The detection criterion is based on the method proposed by Graftieaux et al. (2001), who developed a robust detection criterion for vortices in PIV fields. To estimate the area A and circulation Γ of a detected vortex, the presence of a generic vortex, e.g. a Rankine vortex or a Lamb–Oseen vortex, is assumed. As core area A_0, the area within the maximum of the circumferential velocity in the vicinity of the vortex is taken, as exemplarily shown in figure A.4 (left) where the area A_0 up to a radius of r_0 is considered as the vortex core. For non-circular/ non-ideal vortices a convex hull of an individual shape is created with the same technique. To calculate the circulation, the area A_0 is discretised in finite elements dA. This procedure is exemplary sketched in figure A.4 (right).

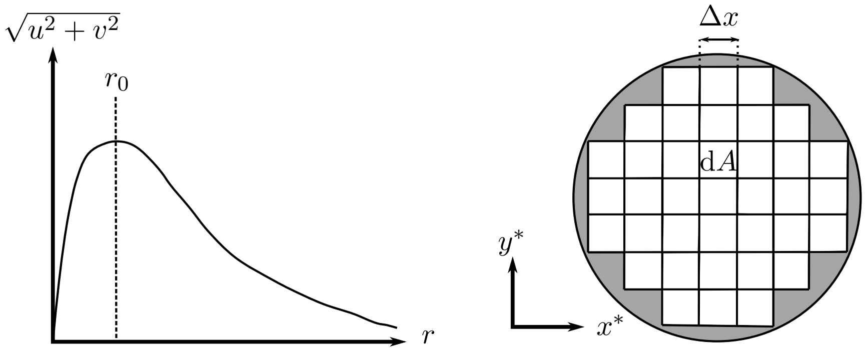

Figure A.4: Left: Sketch of the velocity distribution $\sqrt{u^2+v^2}$ of a Lamb–Oseen vortex with its centre at $r = 0$. Right: Discretised vortex with finite elements dA and vector spacing Δx.

The total circulation Γ of the vortex can be estimated by approximation

$$\Gamma = \sum_i \omega_i \cdot \mathrm{d}A \tag{A.6}$$

with the individual vorticity ω_i of a finite element i. As directly visible in figure A.4 and equation A.6, the accuracy of the procedure is dependant on the size of the finite element dA and the size of the vortex itself. For example, the grey shaded region in figure A.4 right is not accounted for in the discretisation, as no complete cells fit into the region.

To test the accuracy of the circulation and area estimation, the used detection script is tested on a Rankine vortex with a known vorticity $\omega_{\mathrm{rankine}}$ in a fixed Cartesian grid. By reducing the vortex size while keeping the vorticity constant, the relative error as a function of the number of vectors inside the vortex core diameter can be calculated. As the vorticity of the Rankine vortex $\omega_{\mathrm{rankine}}$ is known, the relative error is given as

$$\epsilon_{\mathrm{rel}} = \frac{\frac{\Gamma}{A_0} - \omega_{\mathrm{rankine}}}{\omega_{\mathrm{rankine}}}. \tag{A.7}$$

As the circulation and area estimation are coupled in this method, no individual errors can be estimated. The resulting relative error ϵ_{rel} is plotted in figure A.5. For a vortex diameter $d_{\mathrm{vortex}} > 13$ individual vectors, the relative error drops below 5 %. Hence, as a rule of thumb, one order of magnitude between the vector spacing Δx and the vortex diameter d_{vortex} should be obtained to achieve reliable results.

It should be noted that the error estimation is based on an idealised, perfectly circular vortex. The resulting error for the calculation of the area and circulation form instantaneous

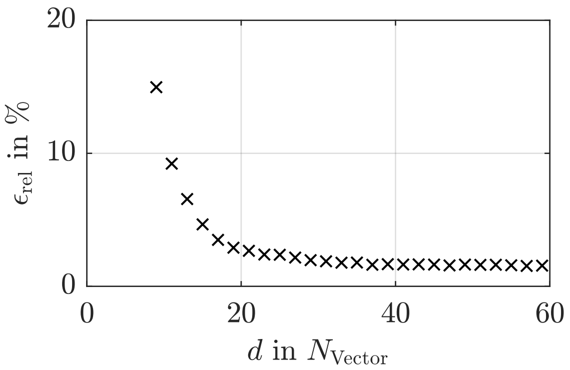

Figure A.5: Relative error ϵ_{rel} of the circulation and area estimation.

flow fields is therefore dependant on the shape of the calculated convex vortex hull and thereby discretisation of a non-circular area. The representative radius r_0 or diameter d_0 can accordingly be considered comparable to a hydraulic diameter. On the other hand, these shortcomings make the here proposed methodology very robust, because it can cope with real, measured flow fields, which are subject to noise and small scale turbulence.

A.5. Vortex path based on the potential theory

In the following, the path of a vortex pair in a turbulent boundary layer shall be estimated based on the potential theory assuming the presence of a pair of potential vortices with the circulation Γ. Due to the flow in the vicinity of the wall, the mirror principle has to be utilised to fully describe the path. In figure A.6 the potential vortices and their mirrored vortices are sketched. The distance of a vortex centre from the wall is denoted as h, the distance between the vortex centres as b at time $t = 0$.

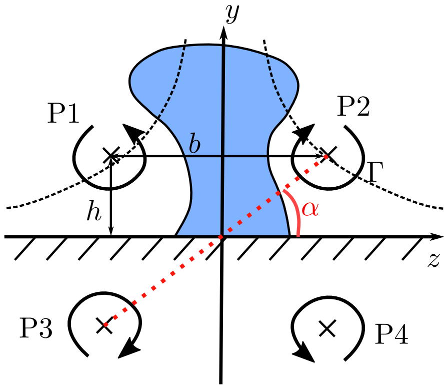

Figure A.6: Sketch of potential vortex pair (P1 and P2) with the circulation Γ and their mirrored vortices (P3 and P4) in the turbulent boundary layer.

To estimate the path of the potential vortex P2, the induced velocities from P1, P3 and P4 on P2 must be calculated.

$$u_{\mathrm{i,P1}} = \begin{pmatrix} 0 \\ \frac{\Gamma}{2\pi b} \end{pmatrix} \tag{A.8}$$

$$u_{\mathrm{i,P3}} = \begin{pmatrix} \sin(\alpha) \\ -\cos(\alpha) \end{pmatrix} \cdot \frac{\Gamma}{2\pi r} \text{ with } r = \sqrt{(2h)^2 + b^2} \tag{A.9}$$

$$u_{\mathrm{i,P4}} = \begin{pmatrix} -\frac{\Gamma}{2\pi 2d} \\ 0 \end{pmatrix} \tag{A.10}$$

$$\tag{A.11}$$

Therefore, the overall velocity u on the potential vortex P2 is

$$u_{\mathrm{i}} = u_{\mathrm{P1}} + u_{\mathrm{P1}} + u_{\mathrm{P1}} \tag{A.12}$$

$$u_{\mathrm{i}} = \begin{pmatrix} \frac{-b^2}{2h)^3+b^2\cdot 2h} \\ \frac{(2h)^2}{(2h)^2 b+b^3} \end{pmatrix} \cdot \frac{\Gamma}{2\pi}. \tag{A.13}$$

With the instantaneous position of the vortex centre of P2 $(y_{\mathrm{P2}}, z_{\mathrm{P2}})$, the distance b and h can be expressed as $b = 2z_{\mathrm{P2}}$, $h = y_{\mathrm{P2}}$. The instantaneous wall-normal velocity of the vortex P2 v_{P2} and spanwise velocity w_{P2} are accordingly defined as

$$v_{\mathrm{P2}} = \frac{\mathrm{d}y_{\mathrm{P2}}}{\mathrm{d}t} \tag{A.14}$$

$$w_{\mathrm{P2}} = \frac{\mathrm{d}z_{\mathrm{P2}}}{\mathrm{d}t}. \tag{A.15}$$

Combining equations A.15 and A.13, the derivative of the vortex path is given by

$$\frac{\mathrm{d}y_{\mathrm{P2}}}{\mathrm{d}z_{\mathrm{P2}}} = \frac{v_{\mathrm{P2}}}{w_{\mathrm{P2}}} = -\frac{y_{\mathrm{P2}}^3}{z_{\mathrm{P2}}^3}. \tag{A.16}$$

Integration of equation A.16 yields the final vortex path

$$\frac{1}{y_{\mathrm{P2}}^2} + \frac{1}{z_{\mathrm{P2}}^2} = C, \tag{A.17}$$

with the integration constant C. Using the initial position at the time instance $t = 0$ of $y_{\mathrm{P2}} = h$ and $z_{\mathrm{P2}} = \frac{b}{2}$, the constant C results to $C = \frac{4}{b^2} + \frac{1}{d^2}$.

For all time instances $t > 0$, the induced velocity is always positive in y-direction and negative in z-direction, according to equation A.13. If this is transferred for a limit value consideration to the path line given in equation A.17, this means that for

$$\lim_{t\to\infty} y_{\mathrm{P2}} = \infty \tag{A.18}$$

$$\lim_{t\to\infty} z_{\mathrm{P2}} = \frac{1}{\sqrt{C}}, \tag{A.19}$$

which is highlighted by the dashed path lines in figure A.6 for the potential vortices P1 and P2.

A.6. Detection of the separation location

The detection of the flow separation in an instantaneous flow field is challenging. In principle, multiple criteria are possible which are based on

- the velocity gradient at the wall $\frac{\mathrm{d}u}{\mathrm{d}x}$,
- the wall shear stress τ_w,
- POD analysis or
- the number of reverse flow vectors $N_{u<0}$.

The calculation of the instantaneous wall shear stress is impossible in large-field of view PIV snapshots, also the velocity gradient near the wall is not suitable for the detection of the separation location as the near wall flow vectors are subject to high noise. Hence, the first two theoretical criteria are inapplicable. As the flow separation is a spatially large feature of the APG flow, it can be detected via POD. Using only a small number of the higher energetic, spatially large modes, it is possible to extract the separated regions in the measured flow field without small scale turbulence influence due to the spatial filtering of the POD reconstruction. Details on snapshot POD application can be found in Berkooz and Holmes (1993). Examining the flow field in figure A.7 (left) closely, two unconnected flow separations are visible, a small separation upstream after that the flow reattaches and a large separation on the downstream end. As the reconstructed flow features with POD are dependent on the chosen modes for calculation and reconstruction, the detection criterion and resulting location is dependent on multiple variables and is not robust. Therefore, the fourth criterion based on the reverse flow vectors was chosen.

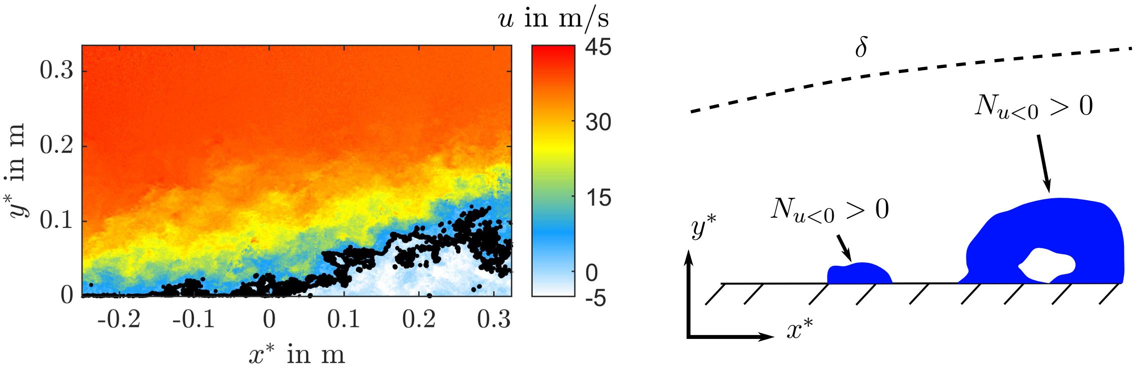

Figure A.7: Principal sketch of the flow separation under APG influence. Blue regions symbolise reverse flow vectors.

In figure A.8, the the cumulative density distributions of the separation location calculated with the reverse flow vectors approach are plotted. To investigate the sensitivity of the position detection on the chosen criterion, the number of chosen reverse flow vectors $N_{u<0}$ is varied in the left plot. The overall trend and shape of the distribution is similar for all investigated $N_{u<0}$ numbers. Only for the case with $N_{u<0} = 1500$, a jump occurs at the most downstream position, which highlights that the threshold number $N_{u<0}$ is chosen at a too high value, because some fields are defined by the method without any separation at all. This is physically wrong, as is seen by the other curves, where reverse flow occurs, which is connected with flow separation. The plot in A.8 (right), the trend for different two Reynolds numbers is tested. The higher the Reynolds number, the later the average flow separation occurs, as discussed in chapter 7. For the detection criterion, no influence of the Reynolds number on the algorithm, results and conclusions can be detected.

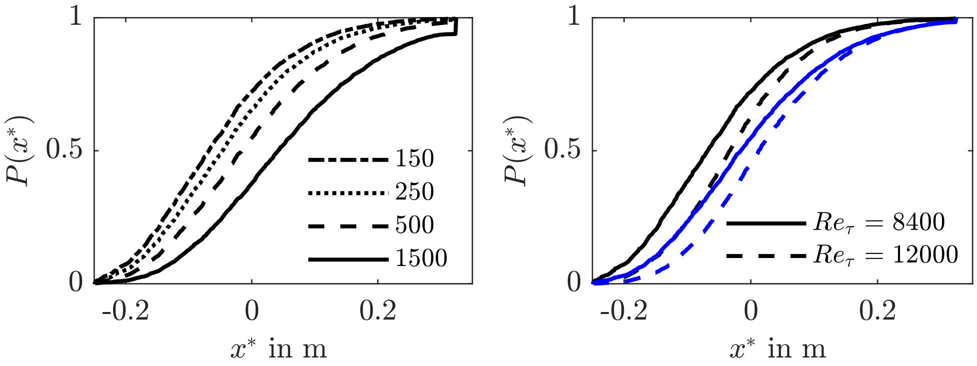

Figure A.8: Cumulative distribution function of the separation location in the APG. Left: Comparison of the influence of different reverse flow vectors numbers N at $Re_{\tau,\mathrm{ZPG}} = 8400$. Right: Comparison of the Reynolds number impact for two reverse flow vector numbers $N_{u<0} = 150$ (black) and $N_{u<0} = 500$ (blue).